

ABSTRACT

Title of Document: EFFECTS OF WALL PLANE TOPOLOGY
ON VORTEX-WALL INTERACTIONS IN
A FORCED IMPINGING JET

Jayson Spencer Geiser
Master of Science, 2011

Directed By: Associate Professor, Kenneth Kiger,
Mechanical Engineering

The phenomenon of a three-dimensionally unstable vortex-ground interaction is studied, motivated by the problem of sediment suspension by vortex-wall interactions from landing rotorcraft. In the current work, the downwash of a rotorcraft is simplified using a prototype flow consisting of an acoustically forced impinging jet. The goal of the current investigation is to quantify the effects of disturbances to the ground-plane boundary layer on the three-dimensional development of the vortex ring as it interacts with the ground plane. A small radial fence is employed to perturb the natural evolution of the secondary vortex, which typically exhibits azimuthal instabilities as it is wrapped around the primary vortex. The fence is observed to localize and intensify the azimuthal development, dramatically altering the mean flow in this region and generating corresponding azimuthal variations in the turbulent near-wall stresses. Multi-plane ensemble-averaged stereo PIV is employed to obtain volumetric, phase-averaged data that are subjected to a triple decomposition to quantify the unsteady behavior resulting from the coherent and stochastic fluctuations of the impinging structures. The effects of the radial fence are examined at both a high and low Reynolds number flows ($Re = 50,000$ and $10,000$, respectively (Γ/ν)), and the data is analyzed in the context of structures leading to significant sediment mobilization

EFFECTS OF WALL PLANE TOPOLOGY ON VORTEX-WALL INTERACTIONS IN
A FORCED IMPINGING JET

By

Jayson Spencer Geiser

Thesis submitted to the Faculty of the Graduate School of the
University of Maryland, College Park, in partial fulfillment
of the requirements for the degree of
Master of Science
2011

Advisory Committee:

Associate Professor Kenneth Kiger, Chair

Professor J. Gordon Leishman

Professor James H. Duncan

© Copyright by
Jayson Spencer Geiser
2011

Table of Contents

Table of Contents	ii
List of Tables	iv
List of Figures.....	v
Chapter 1: Introduction	1
Chapter 2: Literature Review	4
Rotorcraft Brownout	4
Vortex Ring Formation	8
Vortex-Wall Interactions.....	11
Triple Decomposition	16
Surface Roughness Effects.....	18
Additions from this Research.....	20
Chapter 3: Experimental Set-up.....	23
Introduction.....	23
Experimental Set-up.....	24
Inlet Blower	24
Forcing Loudspeaker	26
Conditioning Tunnel	32
Outlet Nozzle	33
Scaling Analysis	34
Data Acquisition	34
Data Processing.....	37
Uncertainty Analysis.....	39
Chapter 4: Results and Analysis.....	41
Collected Data Summary	41
Scoping Results.....	45
High-Resolution Two-Component Data	58
High-Speed Data.....	59
Velocity and Vorticity	59
Periodic Fluctuations	63
Stochastic Fluctuations	67

Low-Speed Data	69
Velocity and Vorticity	69
Periodic Fluctuations	73
Stochastic Fluctuations	75
Profile Decomposition	77
Effect of the Fence	85
3-D Visualization	86
Cut-Plane Analysis	94
Z-Vorticity	94
θ -Vorticity	101
R-Vorticity	103
Instantaneous Images	105
Quantitative Effect of the Fence	108
Chapter 5: Conclusion	116
Appendix A: Pressure Calculations	120
Appendix B: Uncertainty Propagation	125
References	127

List of Tables

Table 3.1: The circulations of each waveform tested at three different peak widths

Table 4.1: A summary of the collected data sets accompanied by abbreviations that will be used for the rest of this document

Table A.1: The area and associated velocities with each section of the jet given an exit velocity of 18m/s.

Table A.2: The loss characteristics of each section of the jet.

Table A.3: The physical characteristics of each section of the jet.

Table A.4: loss values of each section of the jet.

List of Figures

Figure 2.1: A brownout cloud being formed by a helicopter approaching for a landing procedure.

Figure 2.2: A diagram of rotorcraft brownout flow (Leishman 2008)

Figure 2.3.: The initial onset of a rotorcraft brownout cloud

Figure 2.4: Radial striations are formed during the formation of a rotorcraft brownout cloud.

Figure 2.5: Helical vortical structures convecting towards a ground plane (Brown 2000)

Figure 2.6: A visualization of the wavy instabilities in the secondary vortex obtained by Walker et al (1987)

Figure 2.7: The wrapping of the secondary vortex around the primary vortex tube as simulated by Luton and Ragab in 1997. The secondary vortex both wraps above and bends to form legs underneath the primary vortex.

Figure 3.1: The experimental set-up inside the dust chamber (left) and a labeled schematic (right).

Figure 3.2: DHSF A vortex ring formed with a peak width of a).01s and b) .0066s. The return to mean flow for a c)1.5 Period Sine Wave and d) Negative Sine Period

Figure 3.3: A sketch of the experimental set-up.

Figure 3.4: A sketch of the stereo PIV camera placement with attached Scheimpflug mounts

Figure 4.1: The area illuminated by the laser for the different test cases.

Figure 4.2: DHSF Contours of normalized vorticity for a vortex ring created by a single period of a 150 Hz negative sine wave overset on streamlines of velocity. a)-e) show the formation of the ring and f) captures the trailing vortex

Figure 4.3: FHSW contours of normalized vorticity accompanied by streamlines of velocity are shown for a vortex ring formed by a single period of a negative sine wave

Figure 4.4: FHSW vorticity contours of the evolving primary and secondary vortex ring accompanied by streamlines and background color of the normalized time averaged mean flow. The circulation values of the primary and secondary vortex as a function of the normalized radial position.

Figure 4.5: HSIS ensemble averaged values of normalized vorticity during vortex ground interaction accompanied by streamlines of velocity. Figures a ($t/T=0.06$), b ($t/T=0.12$), and c ($t/T=0.18$) detail the formation and interaction with the secondary ring. Figure d ($t/T=0.60$), shows the loss in coherence of the ring after interaction.

Figure 4.6: HSIS ensemble averaged normalized speed of the flow during vortex interaction illustrating the sizeable fluid jet created between the two vortex rings.

Figure 4.7: HSIS ensemble average normalized vorticity for the vortex ring after interaction (top). HSIS instantaneous images of the vorticity at the same phase (bottom)

Figure 4.8: a) The normalized vorticity of the original image after the interaction of the primary and secondary vortex ring. b) The identification of areas above the Q -criterion cutoff (positive vorticity red, negative blue). c) The sorting of the positive vorticity identified by size. d) The final image is used to calculate circulation

Figure 4.9: The circulation values of the vortex breakdown calculated as the circulation of the ensemble average (red) and the average of the instantaneous circulations (blue)

Figure 4.10: A scatter plot of the vortex weighted centroids of the primary (red) and the secondary (blue) ring. The ensemble averaged centroid path for each the primary (solid) and the secondary (dashed) ring are also shown. The primary vortex core size is approximated with the red circle.

Figure 4.11: The vortex core location for a single phase from an actual rotor experiment (Johnson, 2008)

Figure 4.12: Ensemble averaged normalized a) Reynolds stress and b) turbulent kinetic energy for the primary coherent vortex. The same quantities are plotted in c) and d), but the vortex centers have been aligned for each snapshot in an attempt to remove the effect of the “jitter” in spatial positioning of the vortex.

Figure 4.13: Ensemble average velocity of HSHR (\tilde{V}_r top and \tilde{V}_z bottom) at time $t/T=.025$. The primary vortex ring is seen at $r/R \approx 2$ while starting to form the secondary vortex ring.

Figure 4.14: Time average normalized velocity from HSHR (\bar{V}_r top and \bar{V}_z bottom).

Figure 4.15: HSHR vorticity (θ -direction) is plotted at $t/T=.625, .825$, and $.25$ respectively. In each image, three separate vortex events are visible.

Figure 4.16: HSHR vorticity (θ -direction) is plotted at $t/T=.225, .27, .35$, and $.425$ respectively on a larger scale. The boundary layer is visible as the area of negative vorticity near the ground plane.

Figure 4.17: HRHS radial normal periodic stresses ($\tilde{V}_r \tilde{V}_r$) are plotted as a time average and ensemble averages at $t/T=.575, .925$, and $.125$ respectively.

Figure 4.18: HSHR wall normal periodic stresses ($\tilde{V}_z \tilde{V}_z$) are plotted as a time average and ensemble averages at $t/T=.575, .925$, and $.125$ respectively.

Figure 4.19: HSHR Reynolds shear periodic stresses ($\tilde{V}_r \tilde{V}_z$) are plotted as a time average and ensemble averages at $t/T=.575, .925$, and $.125$ respectively.

Figure 4.20: HSHR stochastic stresses are shown. From top to bottom, the images show time averaged radial stresses ($\overline{V_r' V_r'}$), ensemble averaged radial stresses ($\overline{V_r' V_r'}$) at $t/T=.3$, time averaged shear stresses ($\overline{V_r' V_z'}$), ensemble averaged shear stresses ($\overline{V_r' V_z'}$) at $t/T=.3$, time

averaged wall normal stresses ($\overline{V_z'V_z'}$), and ensemble averaged wall normal stresses ($\widetilde{V_r'V_z'}$) at $t/T=.15$.

Figure 4.21: Velocities from LSHR. From top to bottom, the images show time averaged radial velocity ($\overline{V_r}$), ensemble averaged radial velocity ($\widetilde{V_r}$) at $t/T=.025$, time averaged wall normal velocity ($\overline{V_z}$), and ensemble averaged wall normal velocity ($\widetilde{V_z}$) at $t/T=.025$

Figure 4.22: LSHR vorticity (θ -direction) is plotted at $t/T = .45, .85$, and $.075$ respectively. In each image, three separate vortex events are visible.

Figure 4.23: LSHR normalized vorticity (θ -direction) is plotted at $t/T=.225, .27, .35$, and $.425$ respectively on a larger scale. The boundary layer is visible as the area of negative vorticity near the ground plane.

Figure 4.24: A comparison of the trajectory of the high speed (red) and low speed (blue) vorticity

Figure 4.25: LSHR periodic radial normal stresses ($\widetilde{V_r}\widetilde{V_r}$) are plotted as a time average and at $t/T=.325$ and $.7$ respectively

Figure 4.26: LSHR periodic Reynolds stresses ($\widetilde{V_r}\widetilde{V_z}$) are plotted as a time average and at $t/T=.325$ and $.7$ respectively

Figure 4.27: LSHR periodic wall normal stresses ($\widetilde{V_z}\widetilde{V_z}$) are plotted as a time average and at $t/T=.325$ and $.7$ respectively

Figure 4.28: LSHR stochastic stresses are shown. From top to bottom, the images show time averaged radial stresses ($\overline{V_r'V_r'}$), ensemble averaged radial stresses ($\widetilde{V_r'V_r'}$) at $t/T=.3$, time averaged shear stresses ($\overline{V_r'V_z'}$), ensemble averaged shear stresses ($\widetilde{V_r'V_z'}$) at $t/T=.3$, time averaged wall normal stresses ($\overline{V_z'V_z'}$), and ensemble averaged wall normal stresses ($\widetilde{V_r'V_z'}$) at $t/T=.15$.

Figure 4.29: The centroid of the vortex ring for the high speed data (red) and the low speed data (blue) as time progresses accompanied by streamlines of time averaged high speed velocity

Figure 4.30: Profiles of low speed Reynolds radial normal stresses ($V^2/\overline{V^2}$) at $r/R=$ a)2.5,b)3.5c),4.5d),5.5 and high speed Reynolds wall normal stresses at $r/R=e)2,f)3,g)4$. The phase angles ascend based on color as follows: red, green, blue, cyan, magenta

Figure 4.31: Profiles of low speed Reynolds shear stresses ($V^2/\overline{V^2}$) at $r/R=$ a)2.5,b)3.5c),4.5d),5.5 and high speed Reynolds wall normal stresses at $r/R=e)2,f)3,g)4$. The phase angles ascend based on color as follows: red, green, blue, cyan, magenta

Figure 4.32: Profiles of low speed Reynolds wall normal stresses ($V^2/\overline{V^2}$) at $r/R=$ a)2.5,b)3.5c),4.5d),5.5 and high speed Reynolds wall normal stresses at $r/R=e)2,f)3,g)4$. The phase angles ascend based on color as follows: red, green, blue, cyan, magenta

Figure 4.33: Waterfall profiles of radial normal (left) and wall normal (right) velocity from the experiments of Didden and Ho, 1987 (top) and this study (bottom)

Figure 4.34: Detailed profiles of radial normal velocity from at the point of vortex-ground contact (left) and separation (right) in the experiments of Didden and Ho, 1987 (top) and this study (bottom). In the later radially outward profiles, the point where the vertical gradient of the radial velocity is zero is known as the unsteady separation point

Figure 4.35: The θ -component of the normalized vorticity at a phase of $t/T = .45$ and contours of $5 \omega_\theta R / \bar{V}$. The retardation of the primary vortex is shown by the yellow arrow. The exaggerated kink in the secondary vortex caused by the radial fence is shown (green arrow).

Figure 4.36: The θ -component of the normalized vorticity at a phase of $t/T = .55$ and contours of $5 \omega_\theta R / \bar{V}$. The kink caused by the radial fence is shown by the arrow (yellow)

Figure 4.37: The θ -component of the normalized vorticity at a phase of $t/T = .70$ and contours of $5 \omega_\theta R / \bar{V}$. The legs under the primary vortex are shown by the arrow (yellow).

Figure 4.38: The z -component of the normalized vorticity at a phase of $t/T = .35$ and contours of $1 \omega_z R / \bar{V}$. The first kink in the secondary vortex is formed (yellow arrow).

Figure 4.39: The z -component of the normalized vorticity at a phase of $t/T = .60$ and contours of $1 \omega_z R / \bar{V}$. The additional kinks forced upwards by the first vortex kink are visible (yellow arrow).

Figure 4.40: The z -component of the normalized vorticity at a phase of $t/T = .70$ and contours of $1 \omega_z R / \bar{V}$. The secondary kinks wrap beneath the loop of the primary kink (yellow arrow). The secondary vortex forms legs under the primary ring (green arrow).

Figure 4.41: The z -component of the normalized vorticity at a phase of $t/T = .90$ and contours of $1 \omega_z R / \bar{V}$. The secondary vortex is bent and curved above the primary vortex (yellow arrows).

Figure 4.42: The normalized enstrophy at a phase of $t/T = .35$ and contours of $2.5 \omega R / \bar{V}$. The initial kink in the secondary vortex is seen (yellow arrow).

Figure 4.43: The normalized enstrophy at a phase of $t/T = .60$ and contours of $2.5 \omega R / \bar{V}$. The secondary vortex completely wraps around the primary vortex forming a loop (yellow arrow).

Figure 4.44: The normalized enstrophy at a phase of $t/T = .75$ and contours of $2.5 \omega R / \bar{V}$. The loop above the primary vortex is bent and stretched outward (yellow arrow).

Figure 4.45: The z -component of the normalized vorticity near the ground plane. The vorticity is dominated by reflections as this height

Figure 4.46: The z -component of the normalized vorticity at different phases and heights. A, B, and C show $t/T = .3$, $.65$, and $.75$ respectively at a height of $z/R = .16$. These phases depict the formation and spreading of the kink in the secondary and tertiary rings. D and E show $t/T = .65$ and $.05$ respectively at $z/R = .5$. These phases demonstrate the secondary vortex completely wrapping around the primary ring.

Figure 4.47: A cartoon of the secondary vortex beginning to wrap around the primary ring. The cartoon is not to scale, but serves as a visual guide to the wrapping patterns.

Figure 4.48: The r -component of the normalized vorticity at $r/R=2.15, 2.42$, and 2.61 respectively at $t/T=.6$. The figures show different instances of vorticity around the legs beneath and loops over the primary vortex ring.

Figure 4.49: The z -component of the normalized vorticity at $r/R=2.15, 2.42$, and 2.61 respectively at $t/T=.6$. The figures show different instances of vorticity around the legs beneath and loops over the primary vortex ring.

Figure 4.50: The θ -component of the normalized vorticity at $\theta/R=-1.41, -1.30, -1.05$, and $-.50$ respectively at $t/T=.65$. The figures show the wrapping pattern of the secondary vortex around the primary.

Figure 4.51: The θ -component of the normalized vorticity at $y/R=-.9$ and $t/T=.4, .55, .60, .75, .9$, and $.05$ respectively. The figures show comparable vortices to those seen in the 2-Dimensional data; i.e. a secondary vortex formation and vortex rebound.

Figure 4.52: Instantaneous plots of vorticity for heights and phases; a) $z/R=.14$ $t/T=.55$ b) $z/R=.2$ $t/T=.70$ c) $z/R=.32$ $t/T=.60$ d) $z/R=.58$ $t/T=.65$ e) $z/R=.58$ $t/T=.80$ f) $z/R=.5$ $t/T=.65$

Figure 4.53: Time-averaged radial velocity, \bar{v}_r for a plane $z/R = 0.02$. The case with no radial fence is shown on the left, and the case with a radial fence is shown on the right (location indicated by grey stripe). The region used to calculate the azimuthal averages is shown by the black sector, and to sectional lines, AA and BB are indicated.

Figure 4.54: Ensemble-averages of the wall-normal velocity and periodic and stochastic Reynolds stresses in a plane parallel to the wall at $z/R = 0.02$. Note that the color scale for the stress components is stretched quadratically to capture the large variation. The location of the primary (solid line) and secondary (dashed line) vortex core is indicated by the corresponding black line. Contours of the wall-normal vorticity component (ω_z) are shown at several positive (red) and negative (blue) thresholds (1000 to 4000 1/s in 1000 1/s increments).

Figure 4.55: Azimuthal- and time-averaged radial profiles. Mean velocity profiles (left), radial normal stresses (center) and wall-normal Reynolds stresses (right). Grey lines indicate the sectional profiles in the low-speed (AA) wake, and the high-speed (BB) streak noted in the mean radial velocity shown in Figure 4.53

Figure A.1: Performance Characteristics for multiple fans.

Chapter 1: Introduction

Rotorcraft brownout is a complex problem that often results in extensive and costly damage to helicopters during take-off and landing procedures in dusty environments. The problem of rotorcraft brownout is created when the intense downwash wake comes in proximity to a mobile sediment boundary with sufficient energy to suspend large amounts of sand and silt, drastically impairing pilot visibility (Leishman, 2008). These flows are characterized by intense vortices shed from the tips of the rotor blades, which are entrained in the downwash and subsequently interact with the ground-plane in a turbulent stagnation point flow. The sediment suspension process is thought to be dominated by the local dynamics of these large-scale features, which poses a significant problem for accurate prediction of the flow as most sediment suspension models are based upon assumptions of a quasi-equilibrium development. In addition, the rapid erosion of sediment and formation of topographic structures on comparatively short time-scales can potentially significantly alter the boundary conditions from a nominally planar surface, leading to a strong coupling between the evolution of the air and sediment phases.

The focus of this research is on understanding the significant interactions of the nominally coherent tip vortices prevalent in rotorcraft flows with a non-uniform ground plane, placing an emphasis on interpretation of this flow in terms of its expected influence on sediment uplift and bombardment. Although sediment transport is a primary motivation for the study, the current work will limit itself to examining only the single-phase flow, providing a baseline understanding as a comparison for companion studies of the two-phase problem using a mobile sediment bed. An exploration of the causes of topographic structures that alter the formation of the brownout cloud is also included in

the scope of this study. It is hoped that the experimental data generated in this work will serve as a validation for future simulation codes used for modeling these class of flows.

Other goals of this study involve increasing the knowledge of vortex-wall interactions through the examination of volumetric flow fields of the complete vortex trajectory. A qualitative analysis of the vortex-ground interaction with and without the introduction of a radial fence on the ground plane will be presented along with a quantitative study of the velocities and stresses surrounding these two scenarios.

To study the vortex-wall interactions, a repeatable vortex structure similar to a rotor driven flow must be generated. Though adapting a small-scale rotor is the most obvious and realistic solution for vortex generation, rotor driven vortex filaments are complex and instable. To obtain large, converged data set surrounding a coherent vortex event embedded in a wall shear flow, it is necessary to simplify the rotor vortices to increase their stability. This can be achieved in a using the much simpler and more repeatable flow generated by an impinging jet that is forced by modulating the exiting flow to produce a highly coherent vortex ring. While this flow does retain the essential features of a coherent vortex embedded within an axisymmetric downwash, one significant difference is the rings themselves are nominally axisymmetric, and not helical as would be the case in a rotorcraft wake.

Measurements of the flow-field were conducted with both single and stereo-camera PIV. This measurement technique allows for the generation of 2 and 3-component vector planes that can be utilized to generate volumetric data sets of the forced vortices. From the flow fields, vorticity and enstrophy can be calculated and used to visualize the forced vortex. The velocity fields will be examined in terms of their

fluctuations, as these quantities are likely to cause sediment uplift in flows near the threshold value of particle dispersion. The fluctuations are divided into periodic and stochastic components in order to isolate the contributions from the coherent vortex, jitter, and turbulence in the flow. The full results and analysis of the collected are described later in this thesis.

Chapter 2: Literature Review

Rotorcraft Brownout

Rotorcraft brownout is the process of dust entrainment into the rotor flow during an approach to a landing procedure. The uplifted dust disrupts the pilot's view of the landing zone and causes various visual anomalies by creating spurious visual clues, often inducing vertigo. In addition to the immediate threat due to reduced visibility, the uplifted sediment also causes significant abrasion and wear of the rotorcraft blades and engine components (Leishman, 2008). The current mitigation techniques rely on supplemental information from external sensors or use of advanced landing techniques. Though adapting sensors to a rotorcraft to assist in brownout condition flight can be an effective method of accident avoidance, they can be costly, complicated, and heavy. Another currently employed brownout mitigation technique is the use of a modified landing pattern that attempts to out-run the forming brownout cloud. This method increases the risk of damage to the rotorcraft structure involved with landing, because of its increased skill requirements and higher touchdown velocities. Even with the aforementioned mitigation techniques, brownout related damages are serious enough to require a search for a fundamental solution to the problem (Leishman, 2008). The physical effects of brownout can be seen in Figure 2.1, which depicts a rotorcraft forming brownout cloud during a landing procedure.



Figure 2.1: A brownout cloud being formed by a helicopter approaching for a landing procedure.

Rotorcraft brownout flow is a complex two-phase problem involving interactions between the air and dust particles. Uplifting and maintaining suspension of the sediment particles from the ground plane requires a net aerodynamic load sufficient to overcome three main forces: 1) gravity, 2) aerodynamic forces and 3) interparticle cohesive force. The gravitational force will act downwards on the particles with a magnitude proportional to their volume and density. Aerodynamic forces from the rotorcraft flow field are exerted onto the particles. These forces are split into two categories, lift and drag. Finally, particle interaction forces exist between a single sediment object and the rest of the sediment bed. The interaction between particles induces cohesive forces that depend on the electrostatic environment, humidity, particle size, and van der Waals forces. Once the threshold force required to move a particle is overcome, the mass of the particles and

the direction of the forces acting upon them determine whether that particles are subjected to uplift, creep, bombardment, or saltation (Greeley and Iversen, 1987).

The driving flow structure behind uplifting particulates is the blade-tip vortices. As the rotor blades rotate to induce a pressure gradient and lift the rotorcraft, they shed vorticity in the form of a coherent vortex filament. With multiple rotor blades spinning at high velocities, these vortex filaments approximate a series of vortex rings convecting towards the sediment bed. These filaments have a swirl component and are highly unstable. The combination of the shed vortices and the rotor downwash frequently provides a net force sufficient to exceed the threshold value required to uplift the sediment bed. A schematic of the flow is shown in Figure 2.2.

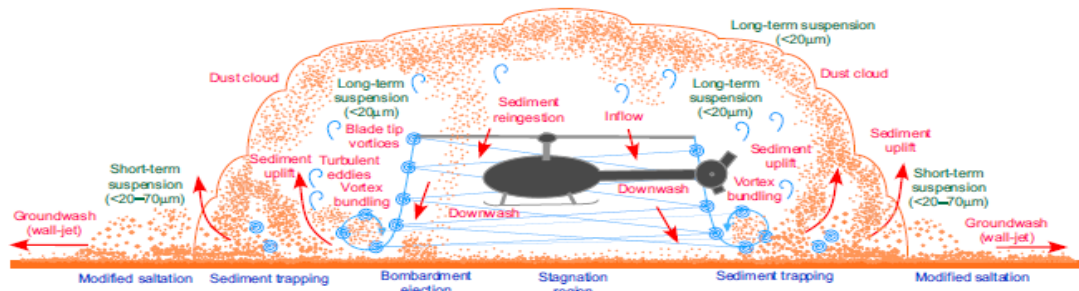


Figure 2.2: A diagram of rotorcraft brownout flow (Leishman 2008)

The effect of the vortex interactions with the ground plane (Figure 2.3 and 2.4) is qualitatively understood, but not to an extent that uplift can be quantitatively predicted given the size and strength of the vortices produced by the rotating rotor blades. To obtain a full understanding of rotorcraft brownout, as well predict the efficiency of mitigation techniques, the vortex-wall interactions in both one and two-phase flows must be thoroughly studied. Evidence of the complications surrounding rotorcraft flow is seen in Figures 2.3 and 2.4. In the downwash flow of a rotorcraft there exists complicated



Figure 2.3.: The initial onset of a rotorcraft brownout cloud



Figure 2.4: Radial striations are formed during the formation of a rotorcraft brownout cloud.

flow structures that lead to patterns in sediment uplift.

The vortical structures of downwash flow are complex in nature, forming helical spirals as they are convected towards the ground plane (Figure 2.5). This shed vorticity is influenced by a swirl component, causing instabilities to form and making large, converged data sets difficult to obtain. However, at high rotational velocities and with multiple rotor-blades generating these vortices, downwash flow can be accurately represented by vortex rings generated in a mean flow

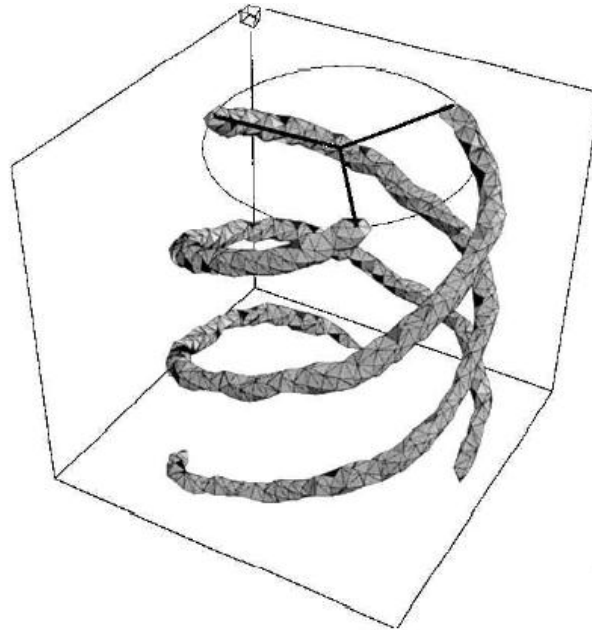


Figure 2.5: Helical vortical structures convecting towards a ground plane (Brown 2000)

Vortex Ring Formation

To create a prototype flow for the vortex driven downwash, an impinging jet can be employed. Free axial jets produce trailing vortex rings downstream of the outlet of their nozzle. These rings, however, are of small scale and accompanied by large amounts of jitter in shape, size, formation, orientation, and convection velocity (Zaman and

Hussain 1980). This jitter makes the statistical observation of these small scale vortical structures difficult. A controllable axial jet must be utilized to provide a repeatable flow similar in structure to rotorcraft downwash flow.

The classical experiment of Crow and Champagne (1971) documented the creation of “vertical puffs” at the exit of a forced jet. By forcing the base flow of an axial jet, instability growth rates inside the jet are amplified, enhancing the boundary layer transition to turbulence. The forcing of the jet leads to the creation of large scale vortex rings at the outlet of the jet (Didden and Ho 1985). These large scale vortical structures are more stable than their unforced counterparts, and are amenable to characterization during formation via phase averaging techniques.

A vortex ring can be repeatedly formed at the end of a shock tube, as demonstrated by Gawthrop, Shepherd and Perrott in 1931. There are two commonly used modern methods of axial jet forcing. The first forcing mechanism utilizes a loudspeaker to acoustically force an axial jet at a given frequency with pure tones (as seen in Widnall and Sullivan 1973). A loudspeaker can be excited at varying frequencies and amplitudes to create a wide variety of forcing conditions. For lower Reynolds number studies (conducted in a liquid medium), a piston mounted over a jet is applied (as seen in Didden and Ho 1985). Both methods of vortex ring generation use a pressure pulse generated by a forcing device to roll-up the free-shear layer at the outlet of a jet. Typically the frequency response of mechanical plunger systems usually limits such forcing to lower frequencies, and as such to lower range of Reynolds numbers.

To compare studies of the two methods of vortex ring formation in an axial jet, acoustic forcing parameters must be mapped to the classical slug model associated with piston generated vortex rings. The slug model takes into account the piston diameter, length, velocity, and discharge time used to form a vortex ring (Lim and Nickels 1995). Evaluating the piston velocity of an acoustically forced speaker theoretically can prove to be an arduous task that depends greatly on the speaker repeatability and quality. Instead, the piston velocity can be estimated experimentally using PIV data at the outlet of an acoustically forced jet. When defining the forcing time as half of the speaker forcing period, the piston velocity can be determined as the time average of the nozzle outlet velocity over the forcing time. These characteristics can be simplified by introducing the amplitude ratio of the forcing; a ratio of the maximum forcing velocity to the base jet velocity. In this case, $\overline{U_p} = \overline{U}(1 + 2A/\pi)$. The piston diameter is equitable to the outlet diameter of the jet, while the piston length relates to the forcing frequency as $L \equiv \overline{U_p}/2f$ (Aydemir *et al*, 2011).

The formation of large scale vortex rings from an acoustically forced jet depends on the forcing conditions of the speaker. Both the amplitude and frequency used to drive the loudspeaker in an acoustically forced jet affect the structures formed downstream of the nozzle outlet. For a fixed frequency, an increase in forcing amplitude will cause the vortex ring to form closer to the outlet of the jet (Aydemir *et al*, 2010). When the forcing frequency is lowered, trailing jets are encountered at the outlet of the nozzle. These trailing jets contain large amounts of vorticity that, at low forcing frequencies, are able to roll up into coherent rings before eventually being entrained into the primary forced ring.

The roll-up of trailing jets limits the total vortex ring strength and stability. Ideal forcing conditions must be ascertained to ensure the formation of a primary vortex ring with a high circulation that is stable and repeatable. Crow and Champagne (1971) reported the ideal forcing frequency as $f = 0.3 * U_e/D$, corresponding to a Strouhal Number of $St = 0.3$; however their employed jet was dominated by resonance structures unrelated to vortex ring formation (i.e. naturally forming vortical structures). More recent studies by Gharib *et al* (1998) and Aydemir *et al* (2010) suggest that the ideal forcing conditions for a sinusoidally excited jet corresponds to an $L/D \approx 4$; in terms of acoustic forcing, this is represented as $\frac{L}{D} = \frac{\overline{U_p}}{2fD}$. The ideal forcing conditions noted in previous literature serves as a starting point when determining the forcing parameters of the axial jet. With relation to this study, a stable, strong, and singular vortex ring must be formed by the forced jet to allow for repeatable uplift conditions on the ground plane.

Vortex-Wall Interactions

The interaction between the vortices created by a forced axial jet and the ground plane is a major contributor of sediment uplift. The vortex-wall interaction can be examined in two ways. The first method involves treating the flow as an axisymmetric event and observing the ring in two-dimensions (i.e., the radial and ground normal directions). However, this reference frame neglects three dimensional instabilities that develop during the ground interaction. In highly turbulent flows, such as that of rotorcraft downwash flow, these instabilities can play a significant role in sediment uplift. Therefore, vortex rings must also be studied in three dimensions as they evolve towards and interact with the ground plane. Adding a third dimension to simulations and

experiments introduces significant complexity and numerical costs to obtaining flow solutions.

Much of the literature surrounding vortex-wall interactions focuses on the generation of a vortex ring that is not embedded in a mean flow. Though this flow is similar to the vortex generation with a co-flow, it is void of the naturally occurring vorticity upstream and downstream of the forced vortex ring. Also, the co-flow tends to force the vortex ring radially outwards upon completion of the vortex-wall interaction.

Potential flow theory suggests that a vortex ring would convect toward a ground plane with a hyperbolic trajectory (Milne-Thompson 1962). As the ring is convected towards the ground by a mean co-flow, it is stretched outward by the ground plane (which can be represented by an image ring). The inviscid stream function, as defined by Helmholtz (1987), is:

$$\Psi(r, y, t) = \frac{(Rr)^{\frac{1}{2}}}{2\pi k} \{(2 - k^2)K(k) - 2E(k)\} - \frac{(Rr)^{\frac{1}{2}}}{2\pi \bar{k}} \{(2 - \bar{k}^2)K(\bar{k}) - 2E(\bar{k})\}$$

where

$$k^2 = \frac{4Rr}{(y-Y)^2 + (r+R)^2} \quad \bar{k}^2 = \frac{4Rr}{(y-Y)^2 + (r+R)^2}$$

and k and E are complete elliptic integrals of the first and second kind defined by:

$$K(k) = \int_0^{\frac{1}{2}\pi} (1 - k^2 \sin^2 x)^{-\frac{1}{2}} dx \quad E(k) = \int_0^{\frac{1}{2}\pi} (1 - k^2 \sin^2 x)^{\frac{1}{2}} dx$$

At low Reynolds numbers ($Re_v = \Gamma/(\nu)$), the viscous response to the vortex ring is sufficiently small to accept the potential solution (Walker *et al* 1987). As Reynolds

number increases, the initial vortex trajectory becomes more similar to the hyperbolic path predicted by potential theory. However, at high Reynolds numbers, vortex-ground interactions lead to a sharp deviation from the aforementioned trajectory.

The viscous response to a vortex ring convecting towards a ground plane produces increasingly complex flow structures. A vortex ring approaching the ground plane will increase the local velocity and vorticity of the wall boundary layer. A “spike” in the shear layer is formed radially outward of the impinging vortex (Elliot *et al* 1983). The adverse pressure gradient located under the vortex ring causes separation to occur in the region below and just downstream of the vortex as it nears its closest approach to the wall (Magarvey and McLatchy 1964). Once separation has occurred, the spike forms a coherent vortex with a circulation that is of opposite sign to the primary ring, referred to as the secondary vortex. The primary and newly formed secondary vortex act together as a dipole lifting off of the ground as a “vortex rebound.” The rebound creates structures of wall normal velocity crucial in uplifting and bombarding sediment particles. The secondary ring, much weaker than its primary counterpart, is rotated around the primary vortex during the rebound and eventually dissipated into the surrounding flow-field. Following the dissipation of the secondary vortex, the primary vortex is weakened and distorted. As the Reynolds number is increased, the radial stretching of the primary vortex begins to be retarded by the strengthening of the secondary vortex. At very high Reynolds numbers, the primary vortex ring has been shown to temporarily reverse its radial motion and move in a looping pattern (Walker *et al* 1987). At even higher Reynolds numbers the primary vortex may form a tertiary vortex after the completion of

a rebound event. These tertiary vortices are less influential than their secondary counterparts in terms of affecting the path of the primary vortex.

To fully understand the interaction of the primary and secondary vortex ring, the vortex-wall interaction must be studied in three dimensions. The significant understanding gained from a volumetric visualization of vortex ground interaction comes from the wrapping of the secondary vortex around the primary. Perturbations in the flow allow for the growth of instabilities in the vortex wrapping process that significantly alter the shape of the secondary ring. The instabilities brought on by the perturbations are grown substantially by the presence of the primary vortex ring. As the instabilities grow, the secondary vortex is bent, stretched, and wrapped around the stronger primary vortex. Thus the vorticity of the secondary vortex (which was originally in the azimuthal direction) now lies mostly in the wall-normal-radial plane. The configuration resembles a continuous series of hairpin vortices. As shown by Walker *et al* (1987), the secondary vortex demonstrates a wavy wrapping behavior when interacting with the primary ring; their visualization of this effect is seen in Figure 2.6. This wavy behavior grows from random azimuthal perturbations, and is hence typically not repeating from event to event, rendering phase averaging techniques difficult.

Simulations of this primary-secondary ring interaction were conducted by Luton and Ragab (1997). These simulations focused on supporting the theories of the short wavelength instability on the secondary vortex. A counter-rotating vortex pair moving toward a wall boundary was simulated using an incompressible Navier-Stokes solver. The secondary vortex was shown to be unstable to the short wave-length Crow-Widnall instability (Widnall, Bliss and Tsai 1974 and Crow 1970) with a preferred wavelength of

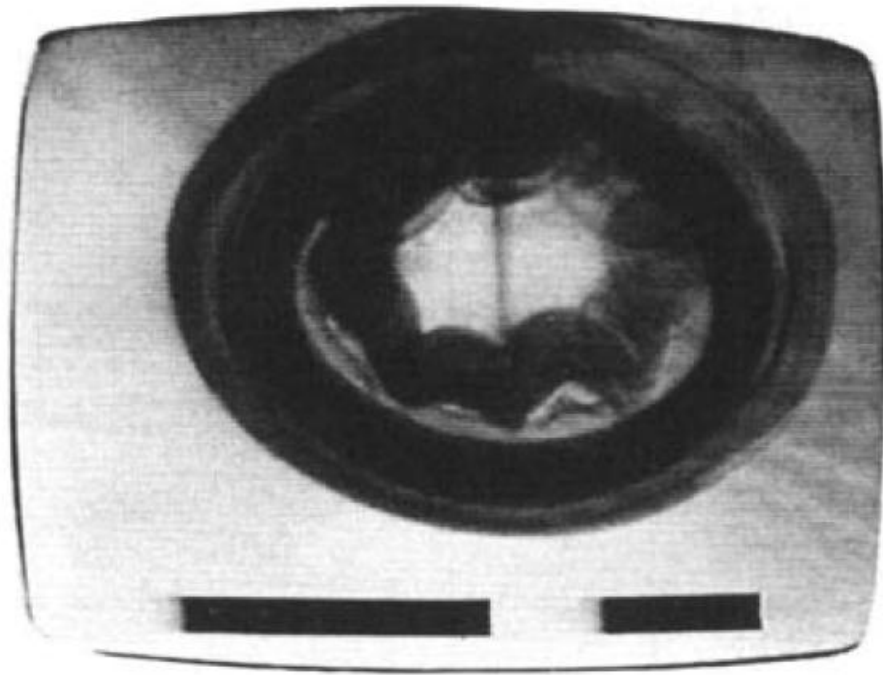


Figure 2.6: A visualization of the wavy instabilities in the secondary vortex obtained by Walker et al (1987)

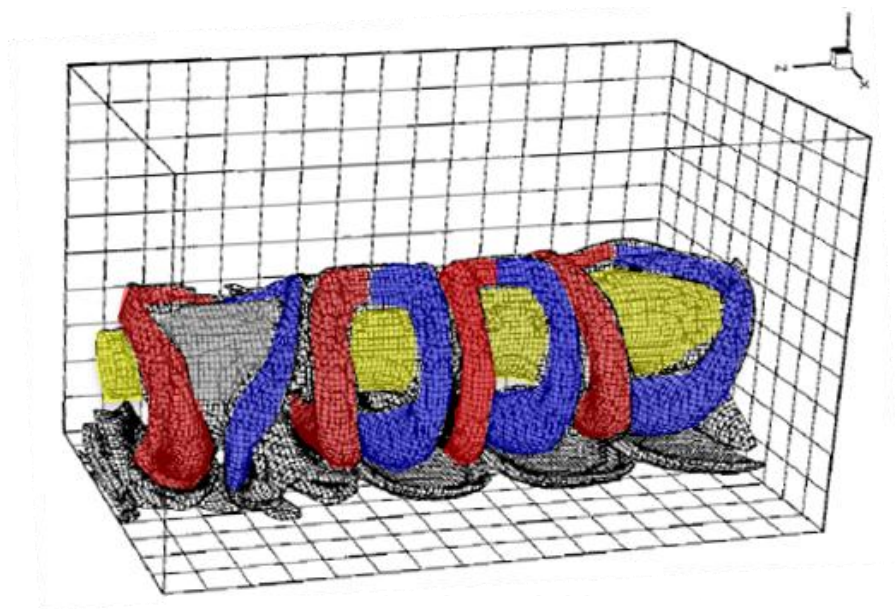


Figure 2.7: The wrapping of the secondary vortex around the primary vortex tube as simulated by Luton and Ragab in 1997. The secondary vortex both wraps above and bends to form legs underneath the primary vortex.

approximately 3.2 vortex core diameters. In the relevant simulations, the secondary vortex is bent, stretched, and wrapped around the stronger primary in “leg-like” structures (Figure 2.7). The leg structures that are adjacent vertically along the primary vortex are far apart underneath of the ring. The legs, primarily in the cross plane, form a series of counter-rotating vortices in the wall normal direction. As the secondary vortex approaches the wall, each leg creates its own vorticity layer on the wall which can roll up to form even smaller tertiary vortices. The Crow-Widnall instability can grow in the tertiary vortices as they revolve around the legs of the secondary vortex and approach the wall. Because the cores are smaller than those of the secondary vortex, the resulting wavelength of their instability is smaller. Thus, energy is transferred to continually finer scales by the creation of smaller and smaller vortices. The complexities of the three-dimensional instabilities complicate the prediction of sediment uplift. Their contribution to wall normal velocity structures may potentially represent significant features relevant to sediment uplift in rotorcraft brownout.

Triple Decomposition

The vortex ring created by a forced axial jet can be viewed using a triple decomposition into coherent and stochastic fluctuations. When dealing with phase averaging in turbulence, the velocities can be broken down into three components. A flow field can be decomposed as follows:

$$u_i = \bar{u}_i + \tilde{u}_i + u'_i$$

where u_i is the velocity, \bar{u}_i is the time-averaged mean flow, \tilde{u}_i is the periodic component, and u'_i is the turbulent fluctuations (Reynolds and Hussain 1971). The phase average,

the average over a large ensemble having the same phase as the reference oscillator, is represented as follows:

$$\langle u_i \rangle = \tilde{u}_i + u_i'$$

with $\langle u_i \rangle$ referring to the ensemble average velocity at a given phase angle. In flows closely associated with a phase locked event, this decomposition can prove a useful analysis tool. Decomposing phase locked data leads to enhancing the understanding of fluctuations about both the time and phase means of a data set. Several basic definitions and properties can be immediately gathered from this decomposition as follows:

$$\begin{aligned} \langle u_i' \rangle &= 0 & \tilde{u}_i &= 0 & \overline{u_i'} &= 0 \\ \overline{\tilde{u}_i \tilde{u}_j} &= \tilde{u}_i \tilde{u}_j & \langle \tilde{u}_i u_j \rangle &= \tilde{u}_i \langle u_j \rangle & \langle \tilde{u}_i u_j \rangle &= \tilde{u}_i \langle u_j \rangle \\ \langle \overline{u_i} \rangle &= \overline{u_i} & \langle \overline{u_i} \rangle &= \overline{u_i} & \overline{\tilde{u}_i u_j'} &= \langle \overline{\tilde{u}_i u_j'} \rangle = 0 \end{aligned}$$

Triple decomposition can be combined with these properties and applied to the Navier Stokes equation by substituting the fluctuating decomposition for the velocity and pressure. This form of the Navier Stokes equation can then be either phase or time averaged resulting in the following:

Phase-averaged:

$$\begin{aligned} \frac{\delta \tilde{u}_i}{\delta t} + \tilde{u}_j \frac{\delta \tilde{u}_i}{\delta x_j} + \tilde{u}_j \frac{\delta \tilde{u}_i}{\delta x_j} + \tilde{u}_i \frac{\delta \tilde{u}_i}{\delta x_j} + \frac{\delta}{\delta x_j} \langle u_i' u_j' \rangle + \frac{\delta}{\delta x_j} (\tilde{u}_i \tilde{u}_j) \\ = - \left(\frac{\delta \bar{p}}{\delta x_i} + \frac{\delta \tilde{p}}{\delta x_i} \right) + \frac{1}{Re} \left(\frac{\delta^2 \tilde{u}_i}{\delta x_j \delta x_i} + \frac{\delta^2 \tilde{u}_i}{\delta x_j \delta x_i} \right) \end{aligned}$$

Time-averaged:

$$\bar{u}_j \frac{\delta \bar{u}_i}{\delta x_j} = -\frac{\delta \bar{p}}{\delta x_i} + \frac{1}{Re} \frac{\delta^2 \bar{u}_i}{\delta x_j \delta x_i} - \frac{\delta}{\delta x_j} (\overline{u_i' u_j'}) - \frac{\delta}{\delta x_j} (\overline{\tilde{u}_i \tilde{u}_j})$$

These forms of the Navier-Stokes equations introduce a new form of the Reynolds stress:

$$\tilde{r}_{ij} = \langle u_i' u_j' \rangle + \overline{u_i' u_j'}$$

A triple decomposition lends itself to understanding the major contributors to sediment uplift in rotorcraft brownout flow. For the mobilization and suspension of sediment into a turbulent boundary layer, the fluctuating stress components are typically the dominant contributors in comparison to pressure gradients and mean viscous shear stress. The velocity fluctuations responsible for uplift are both coherent and stochastic in nature. The triple decomposition of the axial jet flow-field will illuminate the most influential method of sediment uplift.

Surface Roughness Effects

The effects of wall-topology on vortex-wall interactions have been previously studied in terms of surface roughness and its effects on turbulent boundary layers. Two dimensionless parameters can be defined to govern the effects of surface roughness on a turbulent flow. The first of these quantities is the roughness Reynolds number, k_s . This term quantifies the effect of the surface roughness on the buffer region of the flow. The second important parameter is the blockage ratio (δ/k), which defines the ratio of the boundary layer thickness to the surface roughness height. This term controls the effect of the roughness on the logarithmic region of the boundary layer (Jimenez 2004).

The most important effect of surface roughness on a turbulent flow is the change to the mean velocity profile near the wall surface and the consequent change of the friction coefficient (Jimenez 2004). For example, the introduction of riblets (organized structures of large surface roughness) aligned with the mean flow on a wall surface can decrease the surface drag by 10% depending on the relative size of the riblets (Walsh 1990). In turbulent boundary layers over a smooth wall, the majority of the turbulent energy within the layer is found just above the region of the boundary layer dominated by viscosity. In this region of the flow (the “buffer” region), a non-linear self-sustaining cycle is present, and accounts for the majority of turbulent energy introduction into the flow (Jimenez and Moin 1991). This cycle consists of longitudinal streaks of high and low streamwise velocity accompanied by shorter, quasi-streamwise vortices (Robinson 1991).

Studies presented by Yuan and Piomelli (2010) discuss the effects on surface roughness in a turbulent flow undergoing re-laminarization forced by a favorable pressure gradient. The favorable pressure gradient in this study is similar to the pressure gradient seen under a vortex ring as it impinges on a ground plane. A pressure gradient stronger than a critical threshold amount is shown to force a flow to re-laminarize by reorganizing the wall layer and increasing the boundary layer stability. Once the pressure gradient is removed, the flow returns to its turbulent state after experiencing a transition period. The re-laminarization and the transition period can be visualized in terms of the skin-friction coefficient (C_f). During re-laminarization, there is a sharp decrease in C_f , which ultimately returns to its turbulent equilibrium position after the transition period is completed and the flow is once again turbulent. In smooth flows with strong favorable

pressure gradients, the aforementioned change in the skin-friction coefficient is clearly visible. In flows with low amount of surface roughness in comparison to the magnitude of the pressure gradient, a dip in C_f is also seen, though its magnitude is slightly weakened by the roughness. For flows that are dominated by larger areas of surface roughness, C_f never reduces below the value in the equilibrium region, suggesting that re-laminarization never occurs. The study also notes that small scale coherent structures are generated in the wake of the surface roughness structures. These eddies increase the mixing in the buffer layer, and break up the organized streamwise velocity streaks. The break-up of these stabilized streaks is the primary cause of surface roughness leading to a decrease in re-laminarization in a wall layer forced by a pressure gradient.

Additions from this research

This research serves to advance our general fluid mechanics knowledge of vortex-wall interactions, with a particular emphasis in interpreting the relevance of the flow structures potential contribution to sediment transport. The data obtained during this research can be utilized for the validation of complementary vortex ring simulations and as a starting point for interpreting flow structures and mechanisms observed in vortex-wall interaction dominated sediment transport flow conditions. The dominant structures contributing to the uplift and sediment suspension will be explored. An attempt will be made to offer an explanation of the radial striations seen in the sediment bed below a landing rotorcraft. The results of this work, in conjunction with the results of a simultaneous project involving two-phase measurement of the vortex-ground interaction flow will allow for the quantitative measurement of the efficiency of rotorcraft brownout

mitigation techniques by serving as a liaison between formed vortex strength and sediment uplift.

The outcome of this research will include a data set volumetrically detailing the interaction between a vortex ring and a stationary ground plane for high Reynolds number flows (10,000 and 50,000). Previously, experimental data has not been volumetrically collected to the extent of this project for vortex ground interactions at higher Reynolds numbers. A converged data set can provide boundary conditions for simulations of turbulent boundary layers with and without a forced vortex ring. The unstable wrapping of the secondary vortex ring seen in the lower Reynolds number studies of Walker *et al* and the simulations of Luton and Ragab will be viewed experimentally at higher Reynolds numbers, serving as a source of validation. This research will add to the knowledge of the fluid mechanics of vortex-wall interaction by documenting the effects of a single surface roughness event on the interaction between a forced vortex ring and the ground plane. A converged, volumetric, 3-component data set will lead to the documentation of the effects that a single, large scale ground plane disturbance will have on the interaction between the vortex ring and the ground plane. This work will focus on the effect of a single dominant ground-plane disturbance, which allows for repeatable, ensemble averaged measurements and realizations of the flow by increasing the stability of the vortex-wall interaction. The effect of a single element of wall surface roughness has implications in both rotorcraft downwash flow as well as general accelerated turbulent flows. Previously, simulations and experiments have been conducted using multiple instances of randomly generated disturbances on the ground plane. The changes in the secondary vortex wrapping patterns as well as the changes in

forces important to sediment uplift will be examined. By observing a single roughness event, the mechanisms surrounding a turbulent boundary layer interacting with a rough ground plane will be visible on a larger, repeatable scale.

Chapter 3: Experimental Set-up, Data Acquisition, and Data Analysis

Introduction

The purpose of the study is to quantify the flow-field of an analog to rotorcraft downwash evolving and interacting with a ground plane. Rotorcraft downwash is based around a steady mean flow produced downwards from the rotor blades. As the flow reaches the ground plane, the downwards mean flow begins to follow a hyperbolic path toward the ground. Shed from each rotor blade is a vortex filament that is entrenched into the mean flow. The interactions between these tip vortices and the ground plane plays the main role in uplifting sediment into a brownout cloud.

Rotorcraft flow is extremely complex; including a swirl component of the vorticity and instabilities in the generation of vortex filaments. To utilize a phase-averaging method of study, the instabilities in the downwash flow must be lessened substantially. To add repeatability to the downwash flow, a prototype flow is developed that closely approximates the key structures manifested under a rotorcraft. With multiple rotorcraft blades operating at high rotational velocities, tip vortices can be approximated as vortex rings convecting towards the ground. Vortex rings centered about a stagnation point are similar to the tip vortex filaments void of the majority of the complex instabilities of an actual rotorcraft flow.

Two methods of vortex ring generation are historically employed in experiments. The first of these methods is the classic piston generation technique. The piston method, however, is usually employed for lower Reynolds numbers flow, as the vortex ring medium is a liquid in these experiments. The second technique of vortex ring generation

is an acoustically forced axial jet. By forcing an axial jet with a loudspeaker placed upstream of the jet inlet, high Reynolds number vortex rings are generated at the outlet of the jet nozzle. The loudspeaker forcing conditions can be altered to produce vortex rings with characteristics similar to rotorcraft flow. The latter of the two vortex generation methods is employed in this study. The experimental rig is designed for both single and two-phase flow studies using 2 and 3 component PIV.

This experiment conducts both high and low Reynolds number tests, to simulate the structures seen in rotorcraft flow as well as provide large data sets to compare with numerical simulations. The data sets from this experiment will serve as validation for the vortex filament simulations of rotorcraft flow interactions as well as DNS simulations of turbulent boundary layers.

Experimental Set-up

The axial jet is composed of an inlet source, flow conditioning tunnel, a forcing loudspeaker, and a nozzle outlet (Figure 3.1). Each segment of the jet was carefully designed based on previous work to ensure ideal exit conditions and provide the least amount of interference with the generated vortex.

Inlet blower:

The design parameters for the inlet source of the jet flow were determined through a pressure drop analysis. Each component of the jet downstream of the inlet was analyzed to determine the total pressure drop in the jet. The drop was calculated for the inlet tubing, conditioning tunnel walls, conditioning screens, and outlet nozzle. These calculations can be seen in full in Appendix A. For the conditioning screens and

honeycomb, an open area was estimated to determine the pressure drop factor. The largest pressure drop was seen in the inlet tubing, determining that this section of jet was the most vital to obtaining a symmetric flow. To ensure an equal pressure drop from each section of inlet tubing, every section attaching the blower to the jet inlet was cut at the same length. The maximum required exit velocity (18 ms^{-1}) was used to determine the required performance of the inlet source.

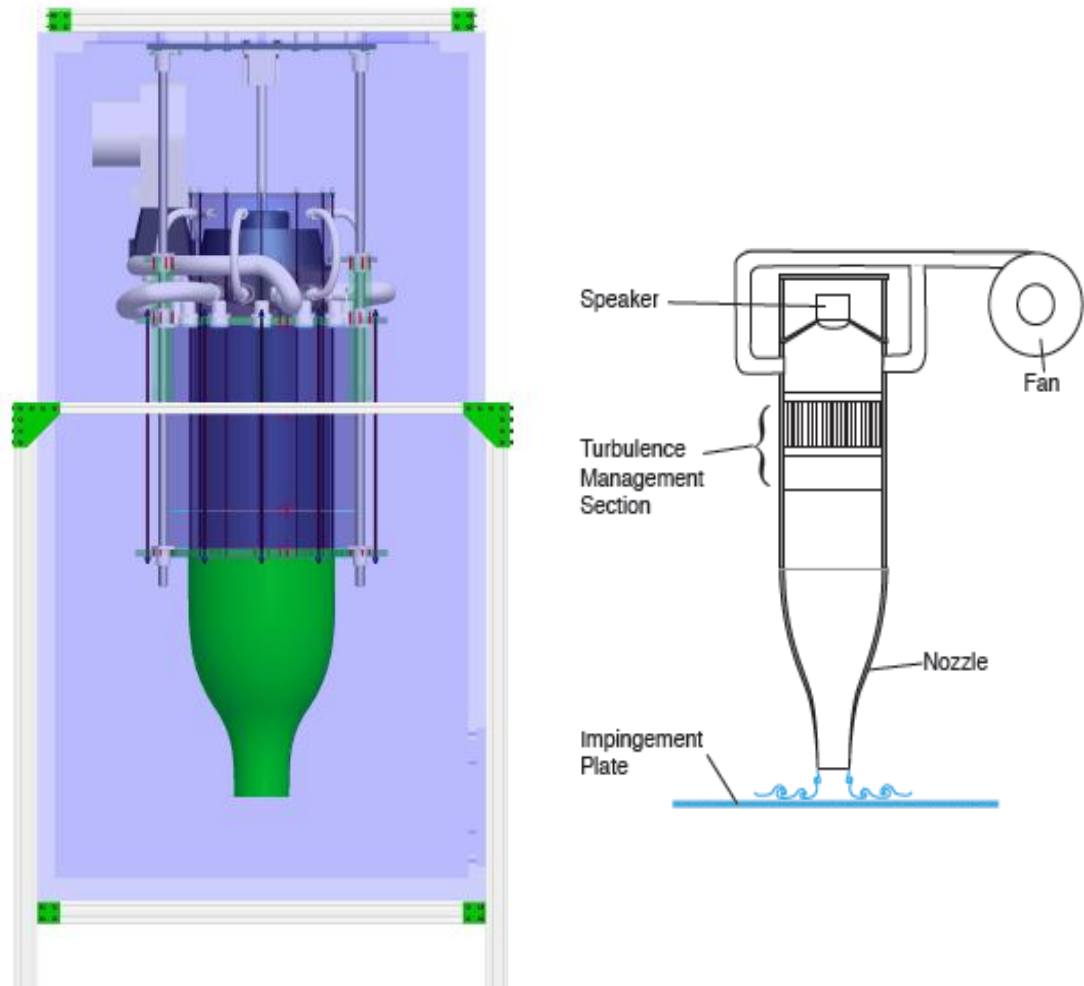


Figure 3.1: The experimental set-up inside the dust chamber (left) and a labeled schematic (right).

From the pressure calculations, a Nautilair 8.9" variable speed brushless blower was selected as the inlet source for the jet. This blower uses a variable voltage input

(between 1.5-10V) to produce differing inlet pressures. The signal voltage to control the fan velocity was provided with a DC signal produced by Labview. The blower outlets into a diffuser designed to divide the air evenly between six equally sized sections of tubing. The inlet tubing is attached to the jet downstream of the forcing speaker in axisymmetric locations around the conditioning tunnel. For low Reynolds number tests (beyond the lower limits of the fan performance), three inlet tubes are removed from the coaxial jet and recirculated into the blower inlet. The three remaining hoses are restricted to $\frac{1}{2}$ of their original diameter to decrease inlet flow to the jet without compromising the blower performance or flow symmetry.

For real-time flow rate estimations of the jet, two pressure transducers (Omega PX653-10D5V Differential Pressure Transmitter) were tapped into the jet. The transducers measured the pressure drop between the inlet diffuser and the outlet nozzle. The reported pressure drop was calibrated to an outlet velocity utilizing the PIV data at different fan control voltages. The pressure transducers were also used to monitor the stability of the jet over time. To ensure constant fan performance over longer testing scenarios, the outputted voltage from the transducers was monitored over several experimental runs. The pressure transducers remained at a constant output voltage (with a tolerance of 0.01 volts) throughout the entire testing procedure. Also, the ambient room temperature was seen to remain constant during the testing intervals. From these tests, it can be concluded that the inlet blower produces a constant mean flow throughout each testing condition.

Forcing loudspeaker:

The forcing loudspeaker chosen for the forced axial jet is a Ciare 12" 2000W subwoofer. This loudspeaker was chosen based on the maximum power requirements and frequency response. The high wattage capability of the Ciare subwoofer ensures that the amplitude ratio of the maximum forced outlet velocity compared to the mean flow is large enough to produce a singular coherent vortex event. At low Reynolds number, the forcing frequency of the jet must be significantly low to attempt to conserve a constant Strouhal number based on the forcing conditions. Most loudspeakers are designed for higher frequencies and have unpredictable performance at the necessary range for this experiment (12.5 Hz). A reliable, repeatable tone is required for phase averaging on forced vortex rings, and the Ciare subwoofer showed the highest quality performance at low frequencies.

The loudspeaker was forced both continuously (with a pure tone), and with single pulsing events. Pure tones were generated with a function generator using a sine wave with a prescribed amplitude and frequency. The signal was phase locked by outputting a square wave as a trigger to the PIV system. Single events were created using LabviewTM and sent at a frequency that prevents interaction between adjacent forced rings (2 Hz). A digital trigger signal was also produced from LabviewTM for phase locking. Different signals were tested for the individual pulsing waveforms to determine the strongest, most stable forcing waveform. The waveforms tested consisted of a half, full, and 1.5 period sine wave (both positive and negative), as well as a ramp signal with a prolonged return to zero voltage. These signals are seen in Table 3.1. Each signal was tested at three frequencies; 50, 100, and 150 Hz. The frequency was measured using the pulse width of half of a sine period. In the case of the ramp wave, the pulse width was determined by

doubling the width of the positive half of the ramp. Samples of the forced vortex created by each waveform at constant amplitudes were taken at constant positions in the flow. From these flow-fields, the circulations of the generated vortex rings were calculated. The circulation was used to determine the strongest waveform and ideal forcing frequency. These values for each waveform are shown in Table 3.1. From the table, it is clear that the 1.5 period wave and the negative single period wave produce the highest circulation strengths. Also, there is an inverse relationship between the frequency and the circulation strength for each wavelength. From the circulation values, the conclusion can be drawn that the ideal forcing waveform is a 1.5 period wave at 50 Hz. However, the stability of each waveform must also be considered before making a final selection.

Waveform stability was determined by imaging the flow-field at the outlet of the jet. High temporal and spatial resolution was employed to capture the formation of the coherent vortex ring at the nozzle outlet. Along with the ring formation, the flow's return to the mean conditions was also imaged. The vortex formation for the 1.5 period and negative single period waves are shown in Figure 3.2c+d. As seen in the figure, when returning to mean conditions, the 1.5 period wave creates a distinct vortex dipole. This dipole is caused by the suction in the jet generated by the trailing negative pulse of the 1.5 period waveform. The dipole is convected towards the ground similarly to the desired forced vortex ring and interferes with the vortex-ground interactions. The single period wave, however, returns to the mean conditions by re-establishing the naturally occurring outlet vortices that are insubstantial in terms of vortex interference. The increased values of circulation strength associated with the 1.5 period wave are unable to overcome the loss of stability generated by the trailing dipole.

The effect of waveform frequency on stability and similarity to rotorcraft flow was studied for the selected waveform shape (negative single period sine). As noted in previous literature surrounding vortex ring generation (Aydemir et al 2010), lower frequency forcing can lead to formation of a tail of coherent vortices following the forced primary vortex. This finding, confounded by the lessened reliability of loudspeakers at low frequency ranges, was observed for the 50 Hz forcing condition. As seen in Figure 3.2a, vortices centered about individual stagnation points circle the primary vortex ring on its approach to the ground. These vortices are eventually engulfed by the primary vortex ring, but not until after the ground interaction occurs. The presence of the vortex tail leads in inaccuracies and interference in the ground interaction, altering the rebound process and increasing instabilities in the instantaneous vortex core location. At higher frequencies (150 Hz), the vortex tail contains vorticity, but as an incoherent trail (Figure 3.2b). For this reason, the 150 Hz negative single period sine pulse was selected as the forcing condition for high speed testing.

Signal amplification is an important step in controlling vortex ring stability. Originally, a high-quality acoustic amplifier was employed to amplify the signals sent to the loudspeaker (Europower Behringer EP3000 Stereo Power Amplifier). However, upon further scoping of the signal from the amplifier, a large amount of interference was observed. With the sharp voltage increase and decrease associated with the single event forcing, the amplifier was unable to reproduce the signal without significant overshoot at the completion of waveform. The trailing overshoot would produce artificial vortex events unrelated to the forced primary ring, leading to instabilities in the flow-field. To

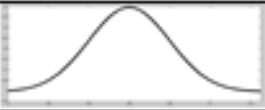

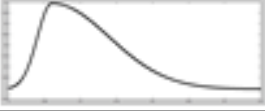

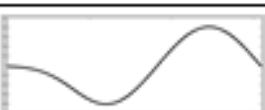

Forcing	Wave Shape	Peak circulation (m^2/s)		
		.02 s	.01 s	.0066 s
Positive Gaussian pulse		0.334	0.343	0.308
Negative Gaussian pulse		0.574	0.430	0.275
Asymmetric Ramp		0.344	0.357	0.350
Full wave "positive"		0.337	0.274	0.226
Full wave "negative"		0.671	0.622	0.582
1.5 wave		0.508	0.713	0.560

Table 3.1: The circulations of each waveform tested at three different peak widths

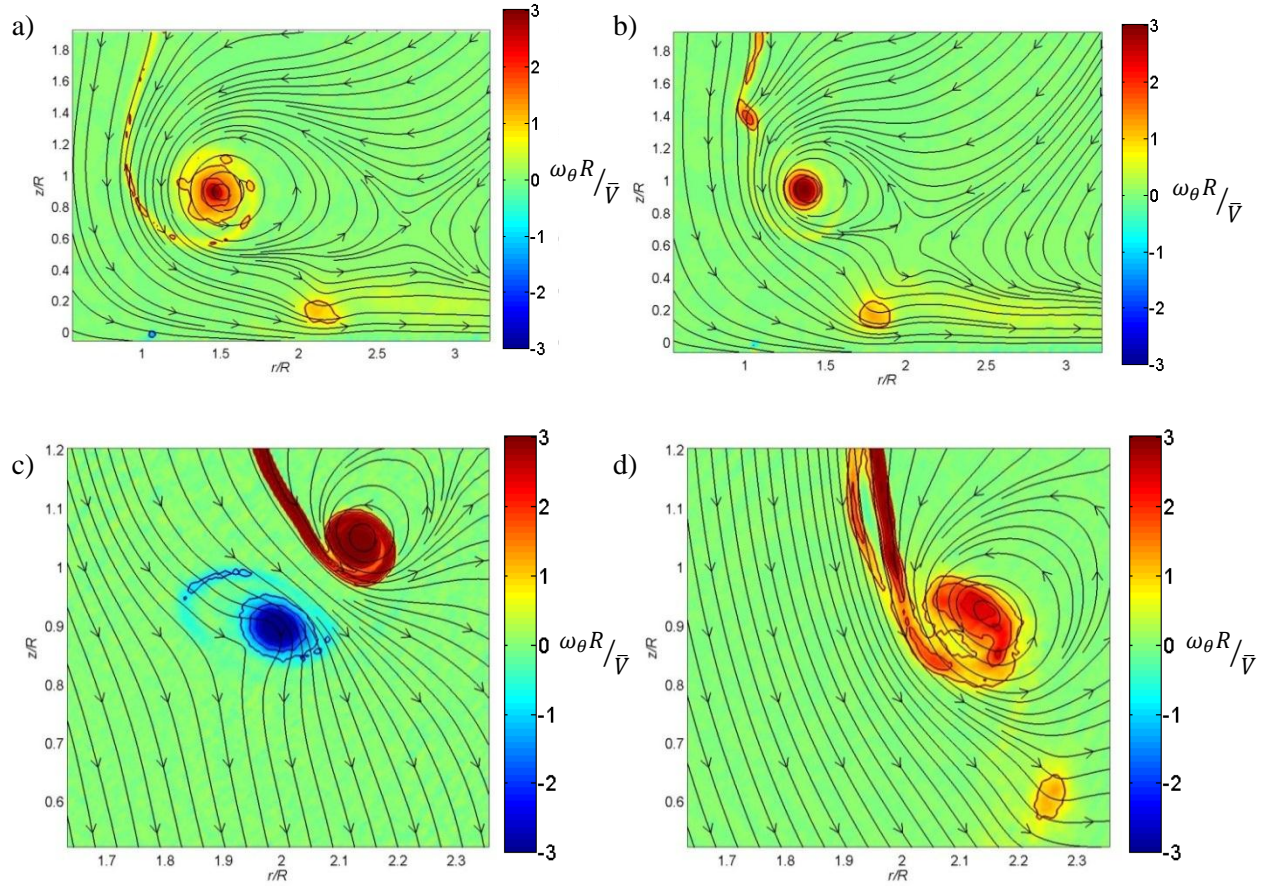


Figure 3.2: DHSF A vortex ring formed with a peak width of a).01s and b).0066s. The return to mean flow for a c)1.5 Period Sine Wave and d) Negative Sine Period

rectify this problem, a high-frequency experimental amplifier (AE Techron DV.1 Experimental Amplifier), replaced the acoustic amplifier, as it is more capable of handling the single pulse excitement. Though the increased ability of the new amplifier to handle the desired signal reduced the errors, a small trailing overshoot still existed in the amplifier output. By combining the sine wave with a Gaussian wave to smooth the beginning and end of the waveform ramping, the trailing overshoot from the amplifier can be effectively eliminated without compromising the strength and shape of the generated vortex ring.

Along with single pulse testing, continuous forcing testing was also conducted. Continuous testing utilizes a sinusoidal pure tone emitted by the loudspeaker to force vortex roll-up. Continuous forcing generates a constant stream of vortices at slightly smaller circulations than produced by single waveform pulsing. The peak width of the pure tone signal was matched to that of the single waveform pulsing for the high speed tests. At lower speeds, the negative pulsing of the pure tone wave can cause suction from the loudspeaker. Suction caused by the loudspeaker forces the roll up of a trailing vortex of the opposite sign of the primary forced vortex. This trailing vortex forms a dipole with the free shear layer and is trajected toward the ground similar to the outlet conditions of the single forced 1.5 period waveform. This dipole follows the primary vortex and interferes with a steady ground interaction process. Scoping studies were conducted to determine the ideal maximum forcing amplitude the does not induce suction from the outlet. At low speeds, the same maximum forcing amplitude ratio as the high speed tests is not achievable, but effort was made to force the jet as close to this value as possible.

Conditioning Tunnel

Airflow is directed from the blowers into the axial jet through a series of six cuts of flexible tubing into the flow conditioning tunnel. The flow conditioning tunnel of the axial jet is constructed from several segments of 12” diameter PVC piping. Inside the piping are several flow conditioners designed to straighten the flow that is turbulently introduced from the blowers. The flow conditioners were selected and placed based on previous studies utilizing an acoustically forced axial jet. Initially, the flow is passed through a coarse screen with an open area of 0.75. Following the coarse screen, a honeycomb structure constructed from plastic straws tightly packed inside the PVC

piping is employed as a flow straightener. The honeycomb is 5 inches long and terminates into the fine screen section. The two fine screens, separated by 6 inches, have an open area of 0.35. The latter of the two screens is at the inlet of the nozzle.

Outlet Nozzle

The outlet nozzle of the jet was designed based of the parameters specified by T. Morel, 1975. The nozzle is employed for three specific reasons; to reduce non-uniformities in the mean flow guaranteeing an even flow at the outlet of the tunnel, reducing the relative turbulence level at the outlet, and to reduce the dynamic loads and pressure losses seen across the screens and honeycomb. A failure to design the nozzle based on pre-specified parameters can lead to up to 10% non-uniformities in the outlet mean flow of the jet. To maintain similarity to rotorcraft flow, the mean flow exiting the jet must be as steady as possible throughout the entire exit area. Failure to achieve this condition can lead to asymmetry in the forced vortex rings. Another concern when designing the nozzle is the possibility of separation in the adverse pressure gradients naturally forming in the nozzle. Small scale separation will cause an increase in the size of the boundary layer and large scale separation will introduce higher levels of turbulence into the outlet flow. Both of these scenarios surrounding separation are unacceptable for this experiment.

The nozzle design consists of two cubic curves combined a point of inflection. Other parameters that determine the nozzle design are the length to diameter (L/D) ratio and the inlet-outlet area contraction ratio. The contraction ratio, selected for optimal flow acceleration, was determined to be 3:1 in order to provide high velocity flow for larger

Reynolds number tests. The other parameters are chosen based on charts given by Morel that document ideal design parameters to avoid separation in the nozzle. From these charts, and L/D ratio of 2.15 about a point of inflection of $0.6L$ is selected.

Once designed, the nozzle was fabricated using a CNC mill out of a single bar of aluminum. To lessen the effects of a stagnant flow at the outlet walls of the nozzle, outlet walls were manufactured as thin as possible on the mill. A separate ring was fabricated to thin the nozzle outlet to a sharp point and attached at the end of the nozzle using a smooth adhesive binding.

Scaling analysis:

Rotorcraft flow is significantly more complicated than the developed prototype flow. The swirl component of the helical vortices is ignored as well as other instabilities in rotor-tip vortex generation. In order to apply the conclusions of this research to the problem of rotorcraft brownout, a scaling comparison must be conducted between the two flow scenarios. For this purpose, the data was non-dimensionalized in terms relating to rotorcraft flow. The velocities and fluctuations presented in this thesis are normalized by the mean jet outlet velocity (\bar{V}), comparable to the downwash velocity of a rotor. The vorticity is normalized by the nozzle outlet radius ($R=50\text{mm}$), which is equivalent to the rotor radius, and the jet outlet velocity. All positions are normalized by the nozzle outlet radius.

Data Acquisition:

Experimental data was obtained using single and two-camera PIV. PIV requires short bursts of a two-dimensional laser sheet to be imaged by a single camera. The laser

illumination was provided by a Litron nanoPIV Nd:YAG laser which produced approximately a 2 mm thick laser sheet. The light sheet was formed by 500 mm focal length cylindrical lens located 1.524 m from imaging planes. The laser was reflected off two mirrors to allow for easier laser sheet manipulation, adding 10 mm to the working distance of the flow. For data sets requiring a larger viewing field, a 60 mm focal length lens was added to the optics configuration as a distance of 1.504 m from the field of view. The light sheet could be rotated to produce vertical or horizontal light sheets as required. Figure 3.3 displays an approximate view of the set-up for a vertical light sheet at the outlet of the nozzle.

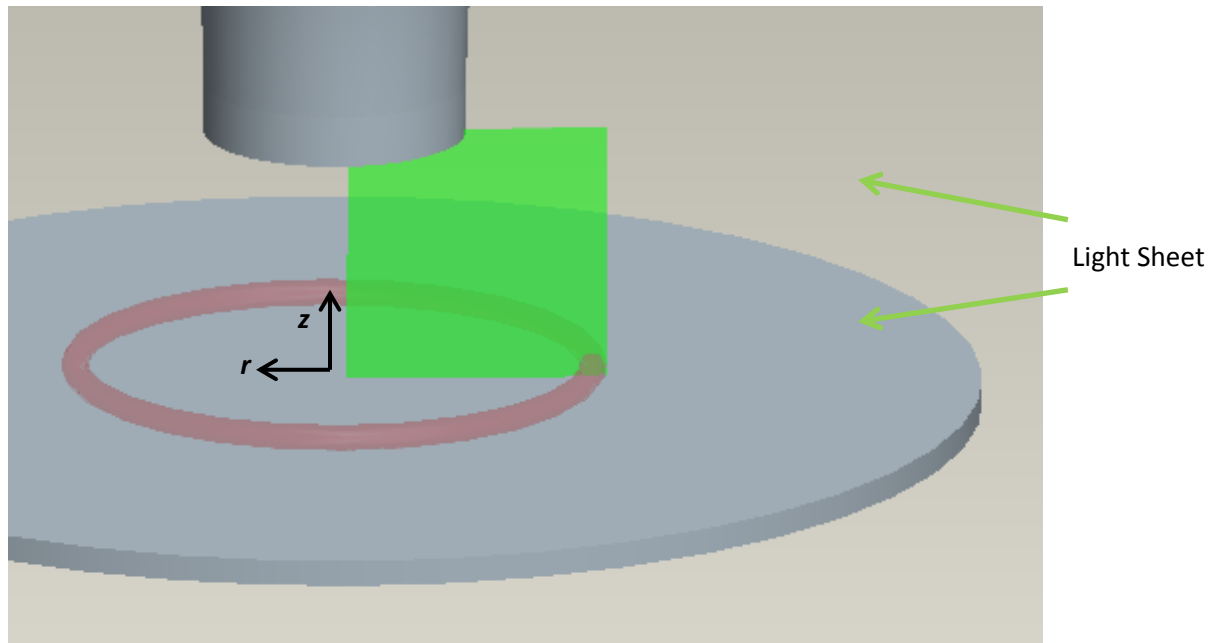


Figure 3.3: A sketch of the experimental set-up.

The images were taken with either an Imager Intense 2Mp camera, a single Imager Pro X 4Mp camera, or two Imager Pro X cameras (for stereo PIV). For the single camera measurement, a vertical light sheet was employed to illuminate a field that

velocity vectors in the radial and wall normal directions can be calculated from. With the single camera set-up, the camera is aligned perpendicular to the light sheet, at a working distance between 0.5-1m (depending on the attached lens and required field of view). With two camera stereo PIV, the laser sheet is turned horizontally, i.e. parallel to the ground plane displayed in Figure 3.3. The cameras were placed on opposite sides of the experiment tank, ensuring that the light scattering angle for both cameras was 90° , therefore giving equal observed particle brightness for each camera. As the two cameras could no longer be equally placed perpendicularly to the light sheet, Scheimpflug mounts had to be attached to each camera to guarantee an even focal plane at the imaging plane. The viewing angle (θ) of the two cameras affects the ratio of the in and out-of-plane errors reported in the PIV images. The amplitudes of these errors have been shown to be equal at $\theta=90^\circ$ (Lawson & Wu, 1997), however viewing angles of $\theta=60$ to 90° are widely accepted as appropriate. For this study, the viewing angle for each camera was determined to be 60° . The stereo camera set-up is seen in Figure 3.4.

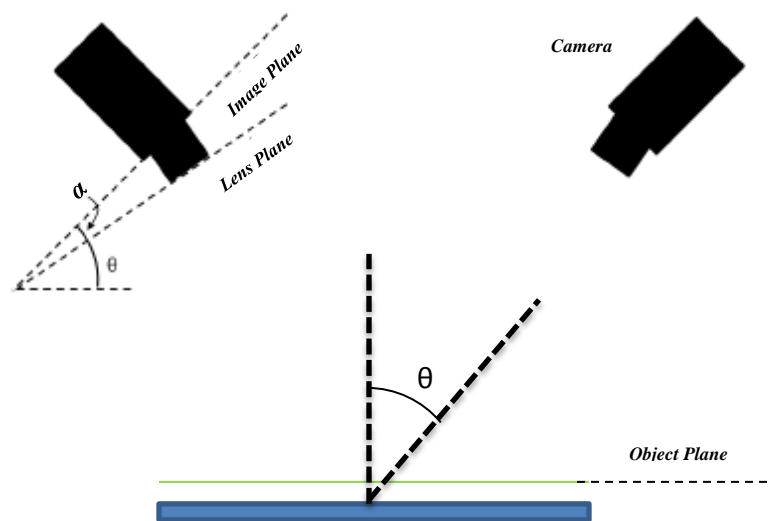


Figure 3.4: A sketch of the stereo PIV camera placement with attached Scheimpflug mounts

To obtain a volumetric data set with planar stereo PIV, several horizontal planes must be obtained at different heights off of the ground plane. Several challenges occur and must be addressed when using this technique to create volumetric data sets of a flow. First, the collected data will only be useful when viewed as ensemble averages, as instantaneous images will not observe the same vortex event. Inconstancies in the position of the vortex at downstream locations in the flow prevents instantaneous images of different vortex events from being combined into a sign volumetric representation of a vortex, as will be detailed in later sections of this thesis. Secondly, moving the laser sheet and cameras to each required viewing plane (25 in total) is extremely difficult, requiring re-calibration of the cameras for each move potential leading to laser alignment problems. To circumvent these difficulties, a design feature was added to the experimental set-up to allow for easy vertical translation of the jet apparatus and ground plane. This translation keeps the same standoff distance between the nozzle tip and the ground plane while allowing the laser to illuminate a different plane of the forced vortices. The vertical increment of movement was obtained using 1 mm metal shims to ensure the spacing in the vertical direction was constant and the vector resolution was similar to the in-plane values. Once data from every plane was obtained, each plane was fit into the proper location in a volumetric data matrix for form a full 3-dimensional data set.

Data Processing

The collected data was processed using standard options in DaVis PIV software. The images were first pre-processed using a sliding minimum subtraction. The sliding minimum subtraction removed the minimum intensity of each pixel in five images from the entire data set. This pre-processing tool was used to remove background noise and excess laser reflections from the unprocessed images. The images returned from the minimum subtraction were then used for a cross-correlation. The cross-correlation was calculated using a multipass algorithm, which first consisted of a single pass of a large interrogation window (64x64 pixels) with 50% overlap. The vectors from this pass are used to obtain more accurate results in the following two passes of smaller (32x32 pixel) interrogation windows with 50% overlap. Between each pass in the multipass cross-correlation, a median filter was employed to remove erroneous vectors that would lead to larger errors. Post-processing of the vector fields consisted of a final pass of a 3x median filter that rejected vectors greater than 2x the median of the surrounding 8 vectors. These vectors were then replaced using an interpolation of the surrounding vectors. After the post-processing steps, the vectors were loaded into Matlab using `readimx` and `Pivmat` (two MatlabTM tools made available by DaVis). Once in MatlabTM, the vector files could be manipulated to make the necessary calculations.

Two optional processing techniques were employed as necessary. The first of these techniques was the introduction of a mask. Because the reflective surface of the ground plane (i.e., a glass plate) being included in some images, it was often necessary to remove portions of the images before processing to prevent erroneous vectors. For these scenarios, a simple mask was applied as needed to the ground plane. The second processing technique employed only for the low speed stereo and high resolution data

(the data sets it was available for), was to process the data using a GPU instead of the standard CPU. The GPU was used to significantly increase the speed of the vector calculations (10x sped up) for the larger data sets. Though this method of processing is not as widely used and validated as the CPU processing, it was necessary to produce the large quantity of vectors obtained during the scope of this study. The only significant difference in the processing parameters with GPU processing is the ability to determine a maximum pixel displacement allowed for each pass (a parameter automatically set with the CPU processing). This parameter was kept consistent between the CPU and GPU processing as to avoid errors.

Uncertainty Analysis

The major source of uncertainty in the presented data sets was the error caused by jitter in the vortex location. As will be discussed in more detail later, the position of the forced vortices varied greatly with each vortex event. However, as jitter is a dominant phenomenon in rotorcraft brownout quantification and is influenced by the mean flow (i.e., not random), it should not be treated as a general source of uncertainty. The other large source of error in the data is the instability in the mean flow of the jet. The natural, unforced jet contains small vortical events formed by the Kelvin Helmholtz instability at the outlet of the jet. These vortices combined with inconsistencies in the jet produce a general uncertainty in the ensemble averaged measurements. To determine the quantity of this uncertainty, the root mean square (RMS) of the velocity reported by 500 image pairs in the was calculated. The maximum value of the RMS was divided by the square root of the number of images (500) to produce the standard error of the mean (SEM) velocity. This error was approximately 1.25% of the maximum reported velocity.

Other common errors associated with PIV experiments are those caused by the seeding density, gradients within the interrogation windows, and in-plane and out-of-plane loss of tracer particles. Several steps were taken to minimize these sources of error. The flow was reseeded between every 1000 image pairs to ensure proper levels of tracer particles in each image. The delay time utilized by the PIV equipment was calibrated for each data set to produce an in-plane pixel displacement of approximate $\frac{1}{4}$ of the smallest interrogation window size. A small interrogation window with respect to the image size (32x32 pixels) was used to minimize the strength of the velocity gradients seen in the image. Though these precautions were taken to minimize standard PIV errors, a conservative assumption to estimate the impact of these errors can still be made. It is generally accepted that the assumption of a 0.1 pixel error will represent these error, translating to an additional 1.25% error in the velocity calculations, bringing the total velocity error to 2.5%.

Sub-pixel interpolation errors are commonly reported with PIV data. The magnitude of these errors are represented by calculating a cross correlation between an image pair consisting of identical images (for stereo data, and image quadruplet with two sets of identical images). The result of this calculation, which is expected to be zero as there is no displacement, represents the sub-pixel interpolation error. The maximum value of this error was found to be two orders of magnitude smaller than the standard error of the mean, and therefore was ignored a significant source of error. Utilizing the standard error of the mean as the uncertainty in the velocity values, error propagation is calculated in Appendix C, and resulted in 3.54% error in the vorticity and 4.33% error in the enstrophy.

Chapter 4: Results and Analysis

Collected Data Summary

Throughout the course of this research, several different data collection conditions were employed. As the general direction of the research evolved, different forcing conditions and data-set sizes were imaged. The first data sets were obtained using single waveform forcing conditions. The reason behind the single pulsing was that it allowed for an individual vortex event to be imaged with no interaction between the forced vortices; the influence of each forced vortex on the surrounding flow field completely disappears in the time before the next vortex is formed (0.5 seconds). Though this forcing method was chosen for this advantage, it contained two major drawbacks. The first of these shortcomings was the inability of the jet to accurately reproduce a single forced vortex ring. Two factors decreased the stability of the forced ring: 1) the amplifier demonstrated large amounts of peak overshoot in the signal sent to the forcing subwoofer, which generated unpredictable areas of coherent vorticity in the flow 2) the period between forcing pulses still produced large-scale vortices (albeit less organized and weaker circulation), which naturally rolls up into smaller vortex rings via the Kelvin-Helmholtz instability. After a single forced vortex ring, the jet produced a vortex with circulation twice that of unforced vortices as it returns to this unforced state. Though this vortex ring does not significantly interact with the ground plane or interfere with the primary forced ring, it is not ideal. Because of these faults in the single event forcing conditions, alternate forcing methods were explored. The chosen method for the second half of data acquisition was to utilize continuous forcing. Continuous forcing produces more stable vortex rings that do not have the same drawbacks as the single forced events.

Continuous scoping studies were conducted and the vortex rings were spaced far enough apart to avoid major interactions during continuously forced events.

Several different fields of view were imaged to collect information about vortex ring formation, trajectory, and ground-interaction. These data planes are shown in Figure 4.1. The vertical planes in this figure were imaged with a single camera, producing two-component vector fields. The horizontal planes were imaged with two cameras, producing three-component vector fields, as discussed in the data acquisition section of this thesis. Two different cameras were used during the course of the research project. Initially the Imager Intense 2 Mp camera was used for all data acquisition. For stereo PIV, two Imager Pro X 4 Mp cameras were purchased, leading to the phasing out of the 2 Mp alternative. The forcing conditions, mean flow speed, imaging plane, image quantity, and camera type for each acquired data set are summarized Table 4.1.

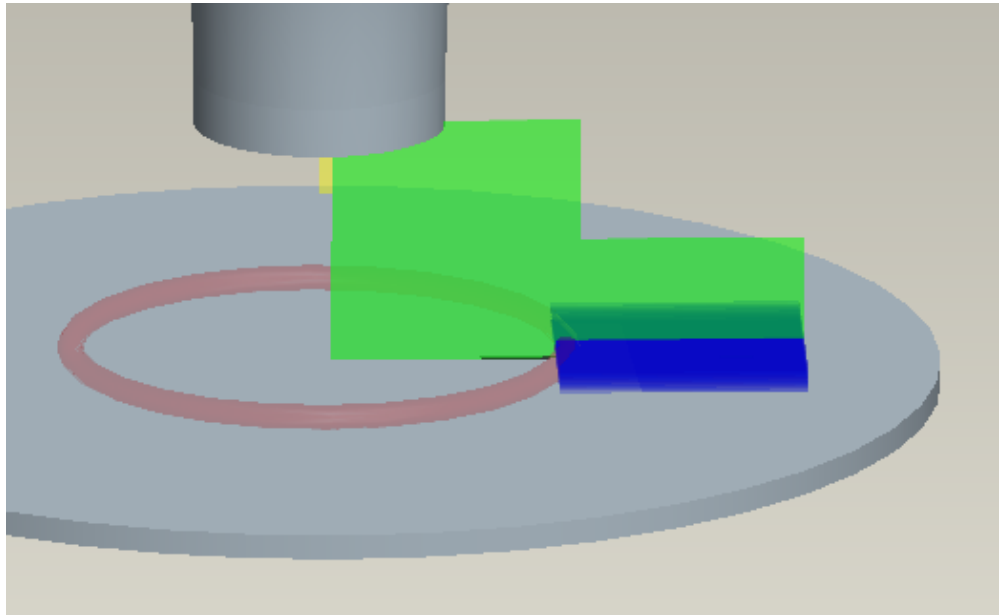


Figure 4.1: The area illuminated by the laser for the different test cases.

Case Scenario	Case Abbreviation	Forcing Condition	Imaging Plane	Image Quantitiy	Camera Type
Initial High Speed Waveform Testing	IHWT	Single Pulse Varying Waveforms Varying Frequencies	10cmx10cm field of view aligned vertically between the nozzle tip and ground plane	50 image pairs per phase 3 phases per forcing waveform	1-Imager Intense 85 mm
Waveform High Speed Formation Scoping	WHFS	Single Pulse Varying Waveforms	3cmx3cm field of view aligned vertically at the nozzle tip	100 image pairs per phase 20 phases per forcing waveform	1-Imager Intense 200 mm l
Waveform Low Speed Formation Scoping	WLFS	Continuous Pulse Sine Wave 12.5Hz	3cmx3cm field of view aligned vertically at the nozzle tip	100 image pairs per phase 20 phases per forcing waveform	1-Imager Pro X 200 mm l
Full Scale High Speed Waveform Tests	FHSW	Single Pulse Negative Sine wave period 75Hz	10cmx10cm field of view aligned vertically between the nozzle tip and ground plane	50 image pairs per phase 20 phases	1-Imager Intense 85mm
Detailed High Speed Single Pulsed Waveform Formation	DHSF	Single Pulse Negative Sine wave period 75Hz	3cmx3cm field of view aligned vertically at the nozzle tip	100 image pairs per phase 50 phases	1-Imager Intense 200mm
High Speed Single Pulsed Interaction	HSIS	Single Pulse Negative Sine wave period 75Hz	10cmx5cm field of view aligned vertically at the ground plane	100 image pairs per phase 20 phases	1-Imager Intense 85mm

High Speed High Resolution Vortex-Wall Interaction	HSHR	Continuous Pulse Sine Wave 75Hz	3cmx15cm field of view aligned vertically at the ground plane beginning at 1R	500 images pairs per phase 40 phases	Imager Pro 4X 200mm
Low Speed High Resolution Vortex-Wall Interaction	LSHR	Continuous Pulse Sine Wave 12.5Hz	3cmx15cm field of view aligned vertically at the ground plane beginning at 1R	500 images pairs per phase 40 phases	Imager Pro 4X 200mm
Stereo Fence Scoping Studies	3DSF	Continuous Pulse Sine Wave 75Hz	10cmx10cm field of view aligned horizontally at the ground plane	100/500 image pairs per phase 20 phases	2-Imager Pro 4X 105mm
Stereo High Speed Vortex-Ground Interaction w/ and w/out a fence	3DHNF/3DHF	Single Pulse Negative Sine wave period 75Hz	10cmx10cm field of view aligned horizontally at the ground plane	50image pairs per phase 20 phases	2-Imager Pro 4X 105mm
Stereo Low Speed Vortex-Ground Interaction w/ and w/out a fence	3DLNF/3DLF	Continuous Pulse Sine Wave 12.5Hz	10cmx10cm field of view aligned horizontally at the ground plane	100/500 image pairs per phase 20 phases	2-Imager Pro 4X 105mm

Table 4.1: A summary of the collected data sets accompanied by abbreviations that will be used for the rest of this document

Scoping Results:

As discussed in the experimental set-up, scoping tests were used to determine the ideal forcing frequency and waveform. From these tests, a high-speed condition of a single period pulse of a 75Hz negative sine wave was selected to force the loudspeaker for the single forcing event studies. At the outlet of the nozzle, this forcing condition produces the ring seen in Figure 4.2. As shown in Figures 4.2a and 4.2b, the shear layer is organized and rolled by the pressure pulse sent from the speaker. A vortex ring is seen to exit the nozzle in Figure 4.2c. As time progresses, more of the shear layer is rolled up into the vortex ring, causing it to increase in both size and strength (4.2d). The ring continues to gather strength as it moves towards the ground plane (4.2e). After producing the primary ring, the jet returns to the natural state consisting of smaller, unstable rings formed by the Kelvin-Helmholtz instability at the outlet of the jet. This return to the natural unforced condition begins with the formation of a trailing vortex at the outlet of the jet. This trailing vortex, seen in Figure 4.2f, is much weaker than the primary forced counterpart and has a negligible effect on the ground plane.

Following the images taken at the nozzle outlet, the full scale ring development was imaged. The results from the full scale imaging are shown in Figure 4.3. Ensemble averages of 50 images pairs per phase were used to observe the ring developing and moving towards the ground plane, and beginning to interact with the ground. The vortex ring exits the nozzle and continues to increase in strength and size as it moves towards the ground plane hyperbolically (4.3a 4.3b 4.3c). Once reaching the ground plane, a spike in the boundary layer is formed by the pressure gradient under the vortex ring (4.3d). The spike is ejected and lifted off of the ground plane forming a secondary vortex

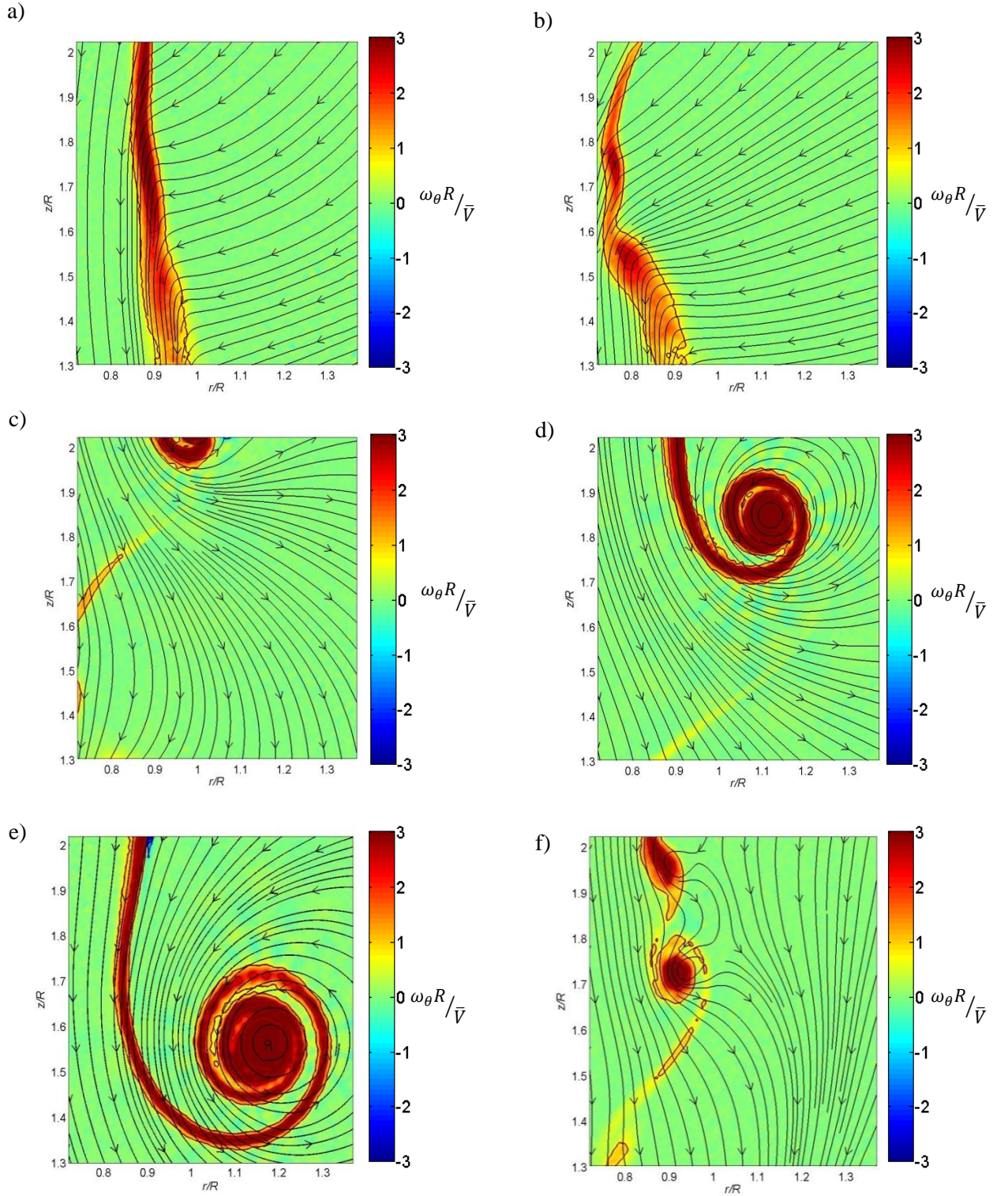


Figure 4.2: DHSF Contours of normalized vorticity for a vortex ring created by a single period of a 150 Hz negative sine wave outset on streamlines of velocity. a)-e) show the formation of the ring and f) captures the trailing vortex

ring of opposite sign as the primary. The primary and secondary ring act together as a vortex dipole lifting off the ground plane and further into the mean flow (4.3e). After the boundary layer separation and vortex rebound, the secondary vortex is dissipated by the primary ring. The primary ring is left weakened, but still maintains its general shape (4.3f). Following the primary ring is a much weaker trailing vortex (4.3f) caused by the jet's return to the mean flow. All of these observations are concurrent with those predicted by previous literature.

Observing the contours of vorticity allows for the imaging of the vortex location at each phase, illuminating the average trajectory for a single pulse forced ring. After the initial roll-up of the coherent vortex, the ring moves in a hyperbolic trajectory towards the ground plane. As noted in the previous literature, the ring is stretched outward as it is forced towards the ground plane by the mean flow. The entirety of the flow (the time mean velocity accompanied by the contours of vorticity following the ring throughout its trajectory towards the ground plane) is seen in Figure 4.4. The stretching, combined with the continuous roll-up of the free shear layer of the jet, slowly increases the average circulation of the primary ring as it moves to the ground, up until the point of impact (Figure 4.4).

The vortex-ground interaction is only roughly imaged in the full scale field of view and requires a more detailed examination. For a greater understanding of the phenomenon that may lead to the uplift of sediment during the vortex-ground interaction, further scoping studies were conducted with a field of view focused about the ground plane. In this region of the flow, vortex jitter is more prevalent. After interacting with the ground plane, the position of the vortex ring in each instantaneous image varies at an

increasing rate over time. Once the primary ring has dissipated the secondary ring, jitter greatly reduces the effectiveness of phase averaging for flow analysis.

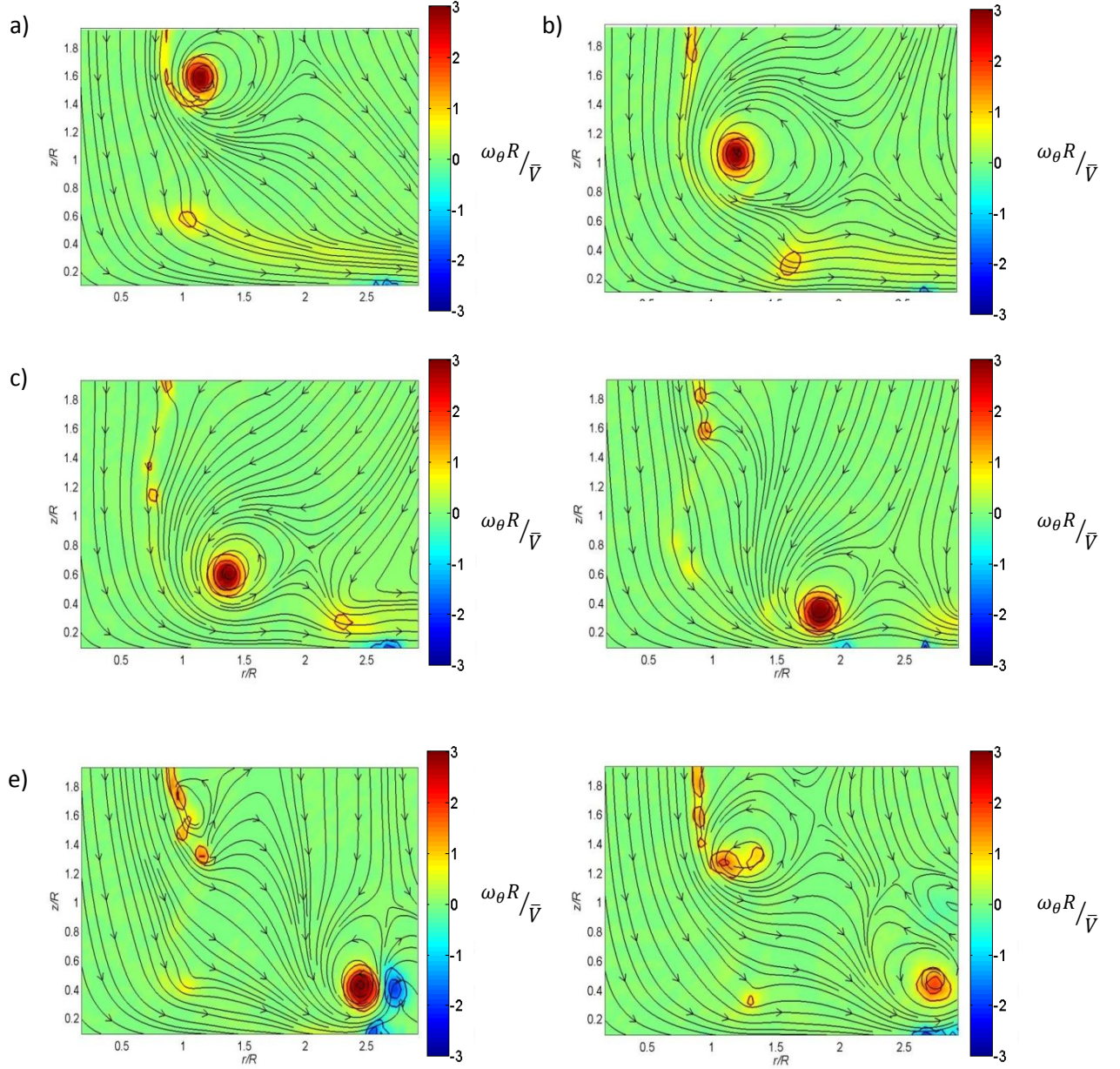


Figure 4.3: FHSW contours of normalized vorticity accompanied by streamlines of velocity are shown for a vortex ring formed by a single period of a negative sine wave

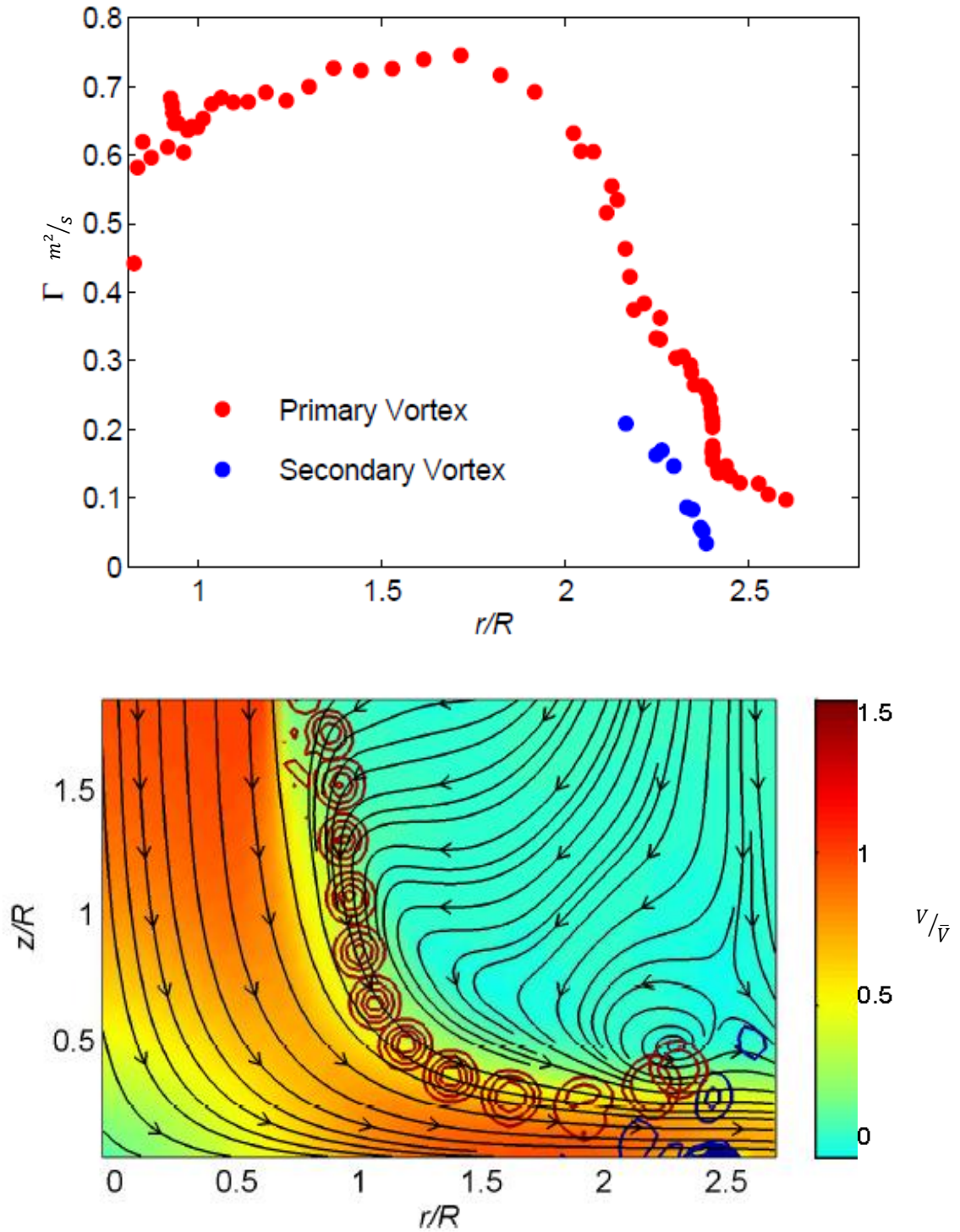


Figure 4.4: FHSW vorticity contours of the evolving primary and secondary vortex ring accompanied by streamlines and background color of the normalized time averaged mean flow. The circulation values of the primary and secondary vortex as a function of the normalized radial position.

The initial vortex ground interaction, seen in Figure 4.3, follows closely to the predicted events in the previous literature. The ground data set confirms the velocity gradients beneath the primary vortex grow the ground plane boundary layer to form a coherent growth radially outward of the primary ring. The boundary is then separated at the spike, forming a secondary vortex ring of negative circulation. This secondary ring continues to grow in strength as the primary vortex causes it to separate from the ground (Figure 4.5a and b), much as the primary vortex continued to roll-up the shear layer of the jet when forming. The secondary ring remains much weaker than the primary ring, obtaining a peak circulation value about the third of that of the primary ring (Figure 4.4). Once the secondary ring is completely separated from the ground plane, the primary and secondary rings act as a counter-rotating dipole, lifting away from the ground plane as a vortex rebound (Figure 4.5c). In between the primary and secondary rings, a high speed jet is formed (Figure 4.6). This jet is a key structure in lifting sediment off the ground plane and forcing it into the mean flow, as it contains the highest area of velocity normal to the ground plane. The stronger primary ring continues to stretch and deform the secondary vortex ring, quickly causing it to lose coherence in the ensemble averaged images. Following the interaction of the rings, the primary ring is left weakened, but is still discernable. However, the primary ring loses its stability during the interaction with the secondary ring, as noted by an apparent sharp drop-off in strength reported by the ensemble averaging (Figure 4.5d). The full-scale ring development tests show an initial agreement with the prior literature, as well as insight into a main cause of sediment uplift

in the jet formed by the counter-rotating pair.

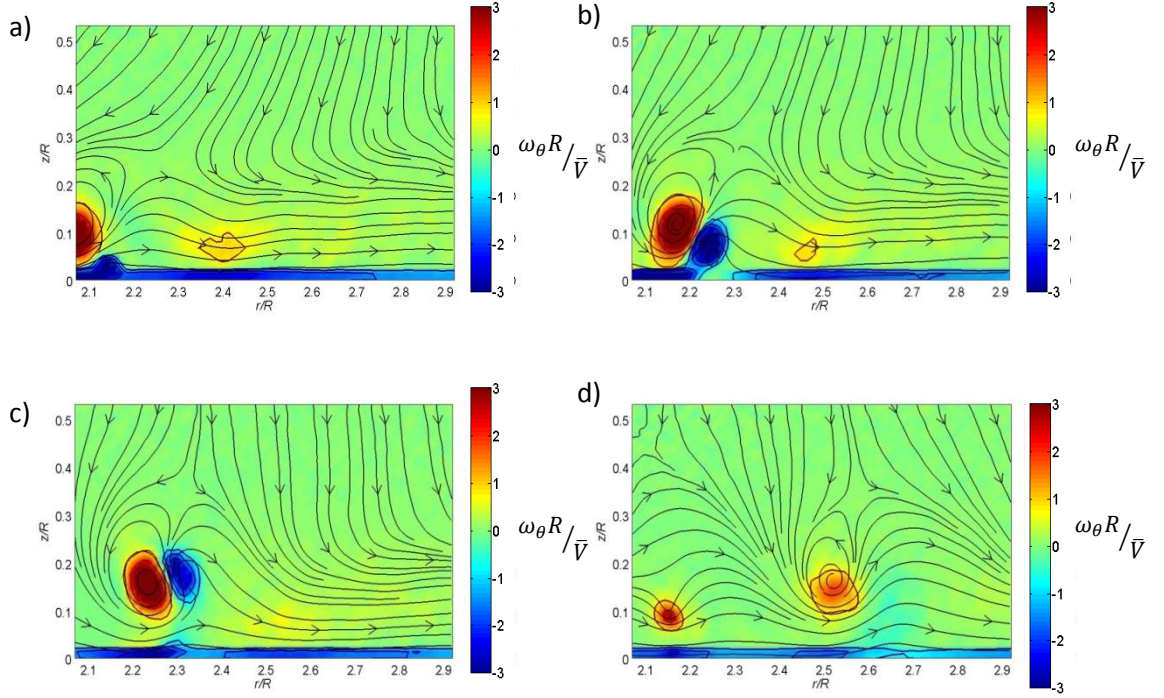


Figure 4.5: HSIS ensemble averaged values of normalized vorticity during vortex ground interaction accompanied by streamlines of velocity. Figures a ($t/T=0.06$), b ($t/T=0.12$), and c ($t/T=0.18$) detail the formation and interaction with the secondary ring. Figure d ($t/T=0.60$), shows the loss in coherence of the ring after interaction.

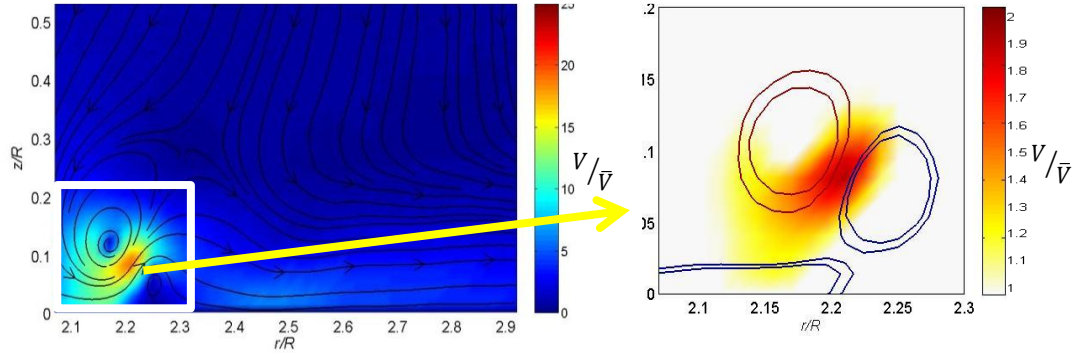


Figure 4.6: HSIS ensemble averaged normalized speed of the flow during vortex interaction illustrating the sizeable fluid jet created between the two vortex rings.

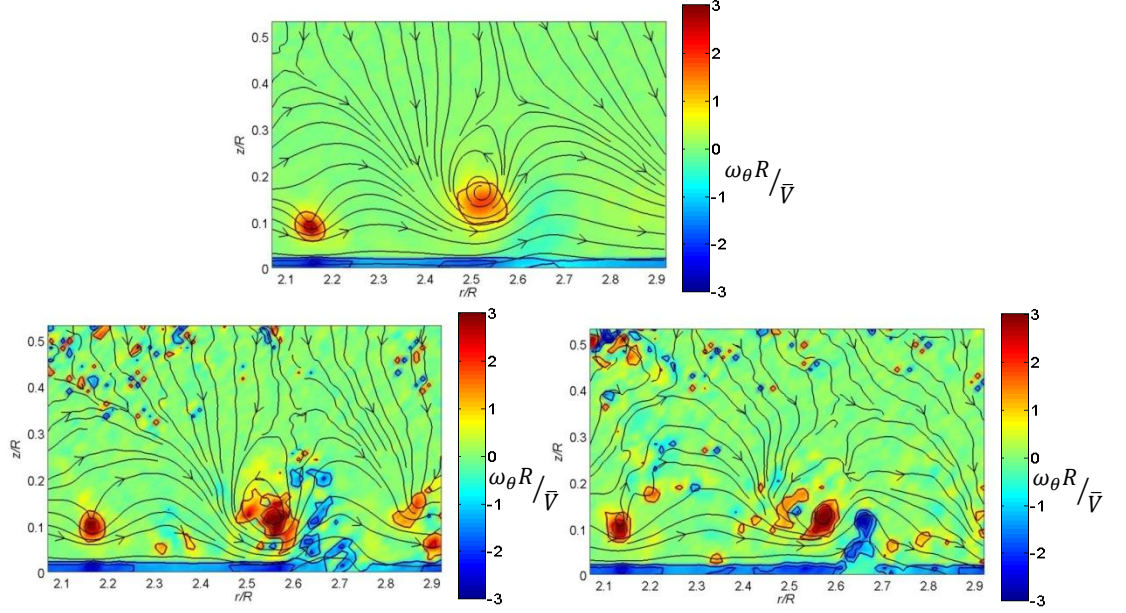


Figure 4.7: HSIS ensemble average normalized vorticity for the vortex ring after interaction (top). HSIS instantaneous images of the vorticity at the same phase (bottom)

To calculate the circulation values for the vortex in areas of the flow with high jitter, simply calculating the circulation from the ensemble averaged field is insufficient (Figure 4.7). Instead, a vortex tracking algorithm must be developed for the instantaneous images (Figure 4.8). The tracking algorithm uses the two-dimensional invariant of the Q-criterion to identify areas of high vorticity and rotation, as to isolate the vortex ring as a separate entity from the ground boundary layer. Areas with a Q-criterion above a threshold value (varied for different phases and forcing conditions, but nominally around 10^5) are identified as areas of interest. These areas are sorted by the sign of vorticity contained within them, i.e. the primary vortex and the secondary vortex are separated (Figure 4.8b). The areas of interest, now separated into positive and negative vortices, are ranked by area, from largest to smallest (Figure 4.8c). The largest area for each sign vorticity (or the two largest in highly turbulent areas) is selected as the vortex

ring. The circulation of the vortex ring is then gathered from these areas by combining them with the initial image of vorticity in the flow (Figure 4.8d). The ensemble average value for the circulation now exists as the average of the instantaneous circulations, as opposed to the circulation of the average. The difference in the circulation calculated by the two aforementioned methods is seen in Figure 4.9. As expected, there is an artificial disappearance of the circulation calculated in the average image brought on by jitter. The vortex jitter washes out coherent structures in the flow, reducing their reported strength. By averaging the instantaneous values of the circulation, a gradual decrease in the vortex strength is uncovered, suggesting that the primary vortex dissipates slowly as it interacts with the secondary ring.

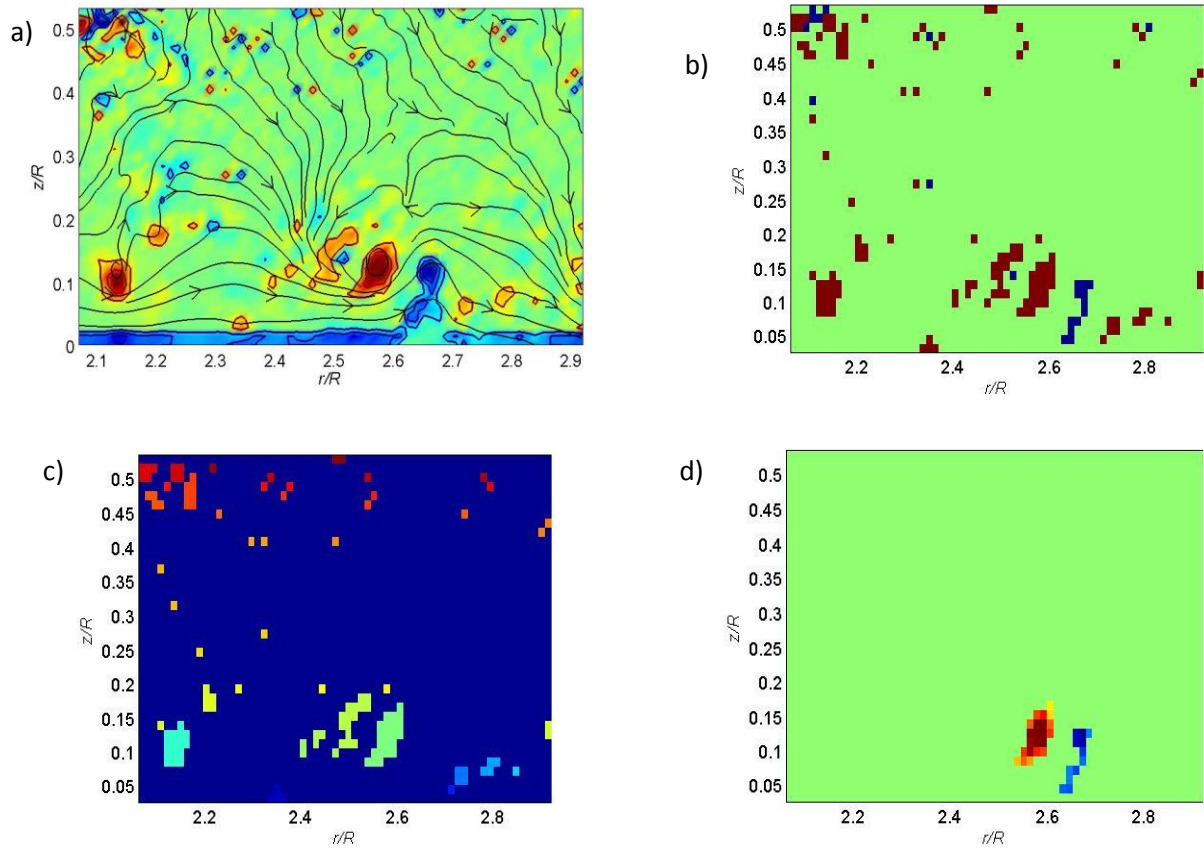


Figure 4.8: a) The normalized vorticity of the original image after the interaction of the primary and secondary vortex ring. b) The identification of areas above the Q -criterion cutoff (positive vorticity red, negative blue). c) The sorting of the positive vorticity identified by size. d) The final image is used to calculate circulation

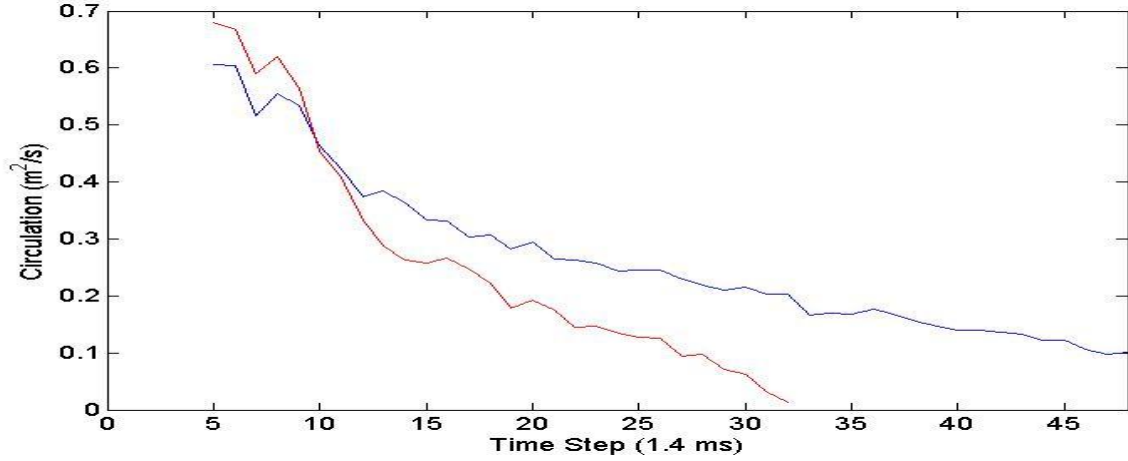


Figure 4.9: The circulation values of the vortex breakdown calculated as the circulation of the ensemble average (red) and the average of the instantaneous circulations (blue)

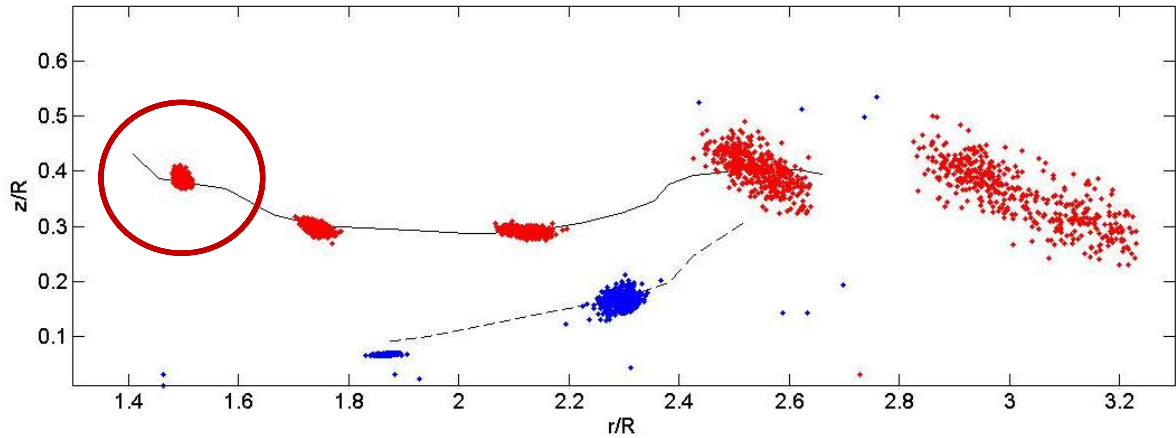


Figure 4.10: A scatter plot of the vortex weighted centroids of the primary (red) and the secondary (blue) ring. The ensemble averaged centroid path for each the primary (solid) and the secondary (dashed) ring are also shown. The primary vortex core size is approximated with the red circle.

From each identified vortex, the vorticity weighted centroid can also be calculated. The vorticity weighted centroid can be utilized to track the evolution of jitter in the primary vortex ring as it develops and interacts with the ground plane. Figure 4.10 is formed by plotting a scatter plot of the position of the centroid of the primary and secondary ring at different phase angles throughout the ring evolution. Though the ring begins as a stable event with jitter contributed to random fluctuations with a magnitude of

0.2R (at $r/R=1.5$), it quickly loses the stability after interacting with the ground plane. When the primary ring begins to form the secondary counterpart at the ground plane ($r/R=1.75$), the jitter begins to increase in magnitude to a total core displacement of 0.4R. At this location, the vortex core centroid is distributed with a coherent bias. The scatter plot is seen to skew with the streamline associated with the ensemble averaged vortex trajectory of the primary ring core. This skewing suggests that jitter is favored along the primary ring trajectory, and therefor produces an artificially elongated ring. As the ring progresses through the breakdown process, the jitter magnitude continues to increase significantly. After the primary ring has completely dissipated the secondary counterpart, the total displacement of the instantaneous centroids exceeds 3R (at $r/R=3$). Such significant amounts of jitter must be taken into account when drawing conclusions

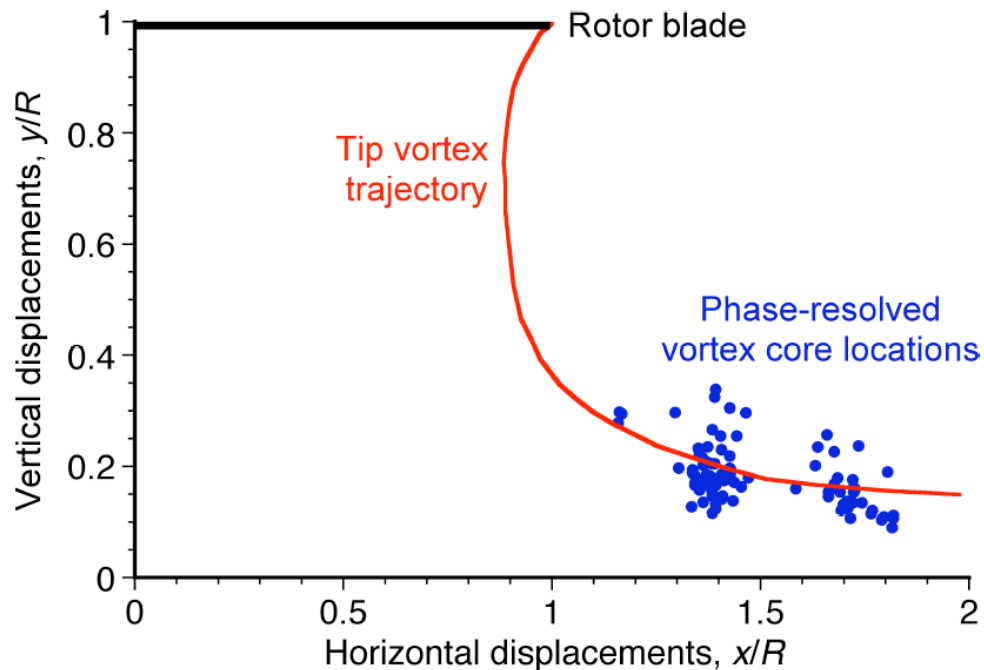


Figure 4.11: The vortex core location for a single phase from an actual rotor experiment (Johnson, 2008)

from ensemble averaged data sets. Jitter is also a significant contributor in rotorcraft flow, as larger instabilities are seen during the development of the helical rotor-tip vortices. As seen in Figure 4.11 (Johnson 2008), rotorcraft flow contains significant jitter prior to the introduction of the instabilities of the vortex-ground interaction. The influence of jitter in the reported velocity quantities is important for thoroughly detailing the effect of vortex-wall interactions in this study as well as applications to full-scale rotor studies.

Once the vortex structures have been identified within each frame, it is of interest to ascertain what contribution this jitter may have towards producing the fluctuating signals shown in Figure 4.12. To determine this, a set of ensemble-averaged statistics were generated based on a mean flow centered about the identified coherent vortex structures. The results of the shifting process is shown in Figure 4.12, and compared to the original “unshifted” data for a vortex early in the flow, prior to when it has interacted with the ground plane and produced a significant secondary vortex. The main feature to note is that the amplitude of the apparent Reynolds stress and turbulent kinetic energy has been significantly reduced. For the Reynolds stress, the magnitude has decreased by an order of magnitude, and the shape of the stress now shows a more symmetric quadrupole shape. The turbulent kinetic energy has decreased by a factor of 6, but the shape is altered such that the contours of the turbulent kinetic energy now align much close to the vorticity. Both of these trends indicate that the fluctuations with the intrinsic coherent vortex are relatively small at this stage of development, and that the signatures seen in the ensemble mean presented in Figure 4.12 are dominated by the jitter component. This has implications for modeling and interpreting the flow measurements, as standard turbulence

models would need to be adjusted to account for this stochastic variability in such a coherent structure.

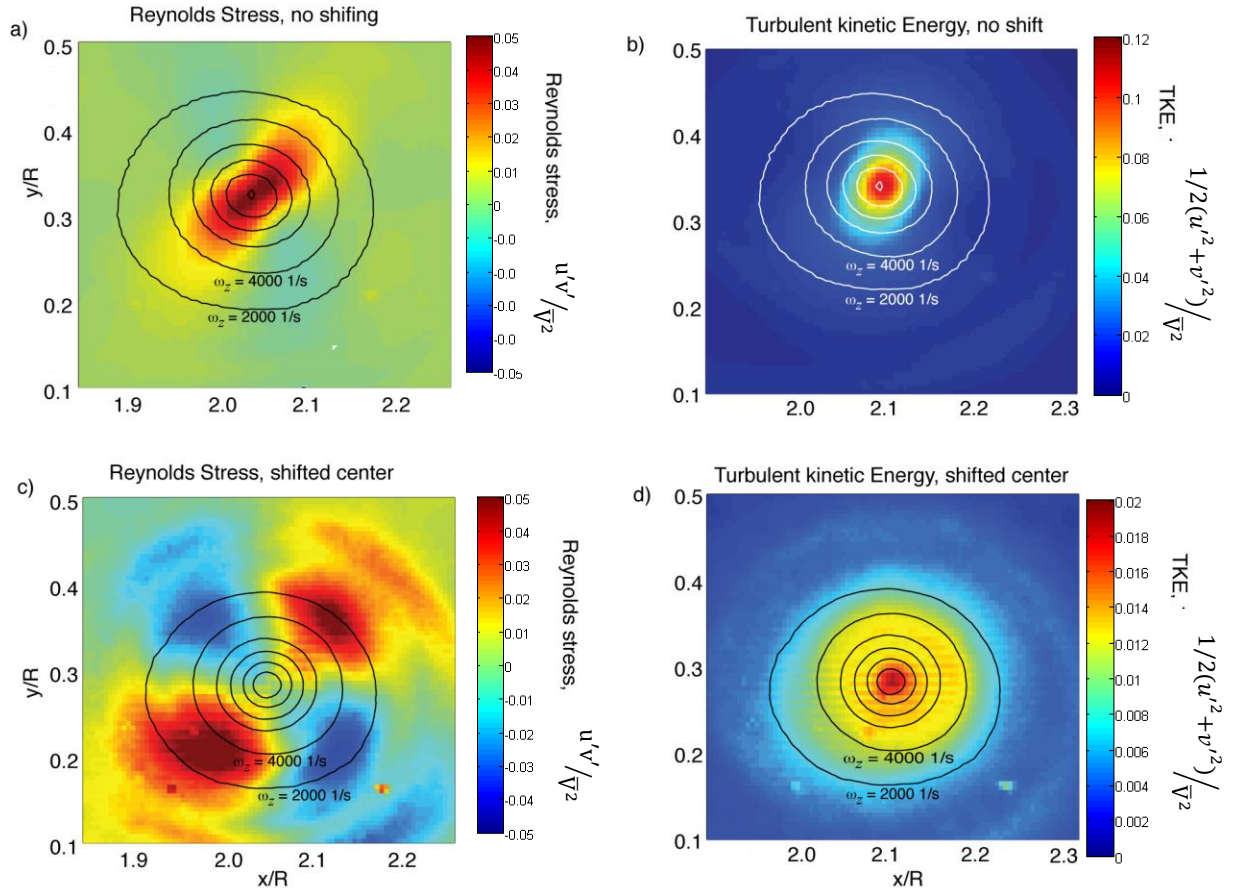


Figure 4.12: Ensemble averaged normalized a) Reynolds stress and b) turbulent kinetic energy for the primary coherent vortex. The same quantities are plotted in c) and d), but the vortex centers have been aligned for each snapshot in an attempt to remove the effect of the “jitter” in spatial positioning of the vortex.

The vortex location algorithm illuminates the need to consider the effect of jitter on all quantities reported in the flow. Jitter can be a large factor in contributing to the turbulence characteristics of the flow, which can change quantities key in uplifting sediment.

High-Resolution Two Component Data:

High resolution data sets were taken to ensure an adequate amount of data points were obtained to fully resolve the complex structures of brownout flow. The PIV images were taken with a 4 Mp Imager 4x camera and a 200mm lens, leading to a 3x3 cm field of view containing 130x130 vectors. Seven overlapping fields of view spanned the radial direction outward of the inner nozzle to capture the vortex approaching and interacting with the ground plane. The data was mosaiced during post-processing to generate a single, complete field of view. At the overlapping areas of the fields of view, slight variations in overlap convergence are noticed. The lack of ideal matching between views can be attributed to an increase in jitter reducing the convergence of the radially outward fields of view and the absence of a temperature controlled environment (in the high speed data only). Continuous forcing was chosen for these tests, as the periodic structures are more useful for comparison with numerical simulations. Temporally, 40 phase angles evenly divide a single vortex period to allow for periodic averaging and fluctuation analysis. At each phase, 500 images pairs were taken in order to balance convergence and reasonable storage demands. To determine the relative effects of Reynolds number changes, two different data sets were collected. The first of these sets (referred to as “high-speed” data, HRHS), has a mean jet exit velocity of 10 ms^{-1} and a forcing frequency of 75 Hz. The second (“low-speed”, HRLS) data set had a mean jet exit velocity of 1 ms^{-1} and a forcing frequency of 12.5 Hz. The previously mentioned triple decomposition was applied to each data set to separate turbulence effects caused by the periodic and stochastic fluctuations.

High Speed Data:

Velocity and Vorticity:

Analyzing the high speed data sets, the vortex rings follows patterns discussed in previous literature. Both components of the velocity (V_r and V_z) display the characteristic shape associated with a vertical slice of a vortex ring. As seen in the ensemble averaged velocity (Figure 4.13), the vortex ring is indicated by an area of high positive radial velocity below and radially outward of the core, and negative velocity above and to the left. In both figures, the primary ring has begun to form the secondary vortex, duplicating the expected vortex signature with the opposite sign near the ground plane. When observing the time averaged flows (Figure 4.13), the mean flow accompanying the vortex ring is visible throughout the imaging area. The time averaged radial velocity (\bar{V}_r) has a peak positive velocity of approximately 10 ms^{-1} between $1.5 < r/R < 2.25$ corresponding to the horizontal jet between the primary vortex ring and its image (wall interaction). The mean velocity demonstrates a small rebound upwards at $r/R=2$, where the primary vortex is known to form the secondary vortex and separate from the wall. \bar{V}_z suggests that the largest wall normal velocities exist as the vortex ring is being forced towards the ground by the jet. A peak in wall normal velocity is seen in the area of rebound ($r/R=2$) which agrees with the forming of the jet between the two interacting vortex rings.

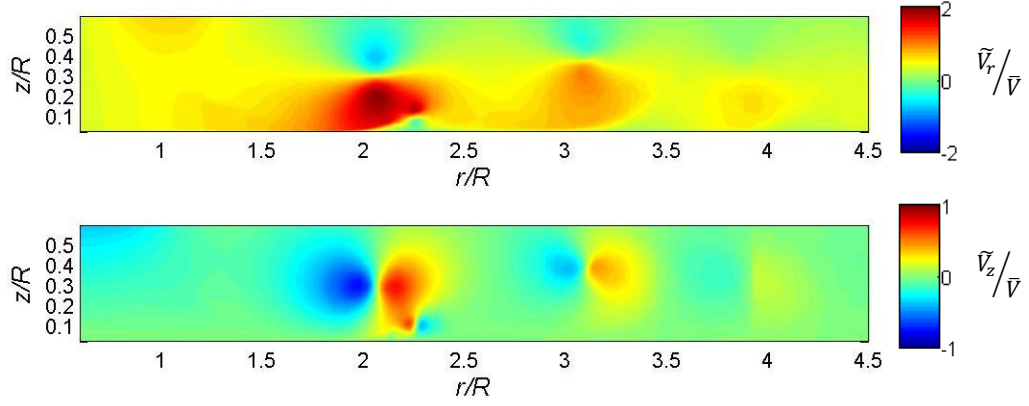


Figure 4.13: Ensemble average velocity of HSHR (\tilde{V}_r top and \tilde{V}_z bottom) at time $t/T=.025$. The primary vortex ring is seen at $r/R \approx 2$ while starting to form the secondary vortex ring.

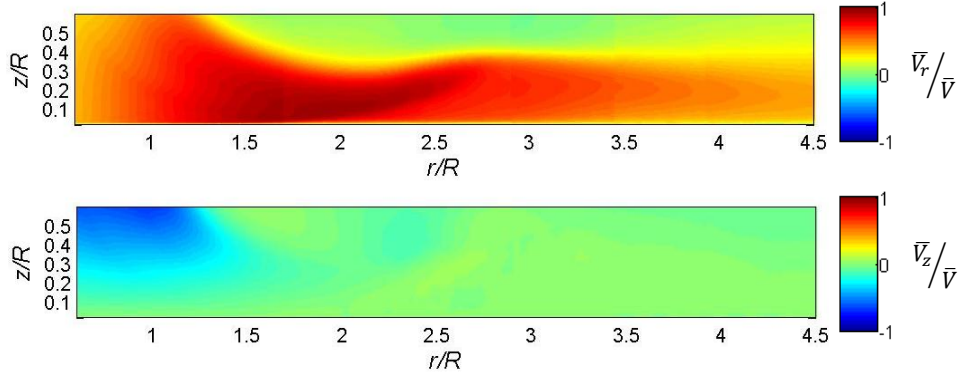


Figure 4.14: Time average normalized velocity from HSHR (\bar{V}_r top and \bar{V}_z bottom).

By tracking the vorticity, the ensemble averaged vortex trajectory near the ground plane can be visualized (Figure 4.15 and 4.16). As the vortex ring first approaches the ground plane, the naturally occurring boundary layer begins to form the “spike” first noted by Magarvey and McLatchy in 1964. This spike grows as the ring is stretched and continues to move closer to the ground plane (Figure 4.15b and 4.16a). Eventually the spike forms into a secondary vortex and separates from the ground plane forming the characteristic dipole seen in vortex-ground interactions (Figure 4.15c and 4.16c). The boundary layer continues to be lifted into the mean flow after the secondary vortex has

separated (Figure 4.16d), continuing to strengthen the secondary vortex in a manner similar to the development of the primary ring. As the dipole progresses, the secondary ring is wrapped around the primary and weakened. Following the complete wrapping of the secondary ring, jitter begins to dominate the flow, slowly washing out the ensemble averaged structures seen in the earlier phase angles. As the interaction between the two vortices is a highly non-linear event, similar flows are expected to quickly diverge from each other, i.e. cause jitter in the vortex location. In these areas in particular, the stochastic fluctuations are expected to increase with the rising influence of the jitter. After the ejection of the secondary vortex, the boundary layer is still lifted into the main flow, however with much higher jitter in the location, and therefore appears washed out in the ensemble images (Figure 4.15a and 4.16a). The continuation of the boundary layer to be uplifted into the flow field leads to the possibility of a tertiary vortex being formed,

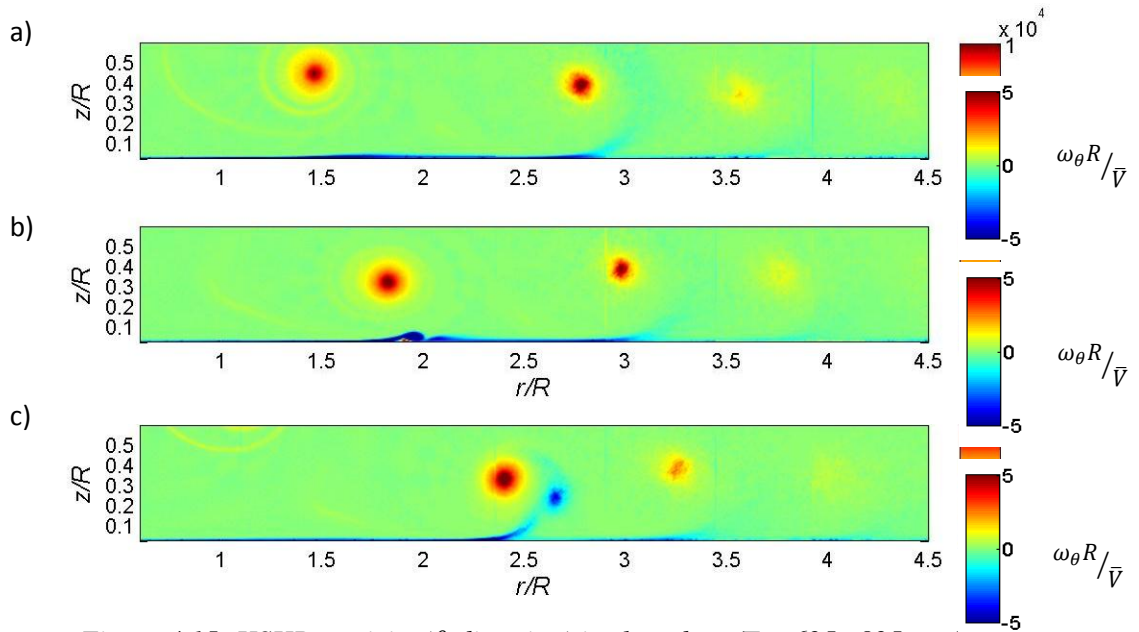


Figure 4.15: HSHR vorticity (θ -direction) is plotted at $t/T = .625, .825$, and $.925$ respectively. In each image, three separate vortex events are visible.

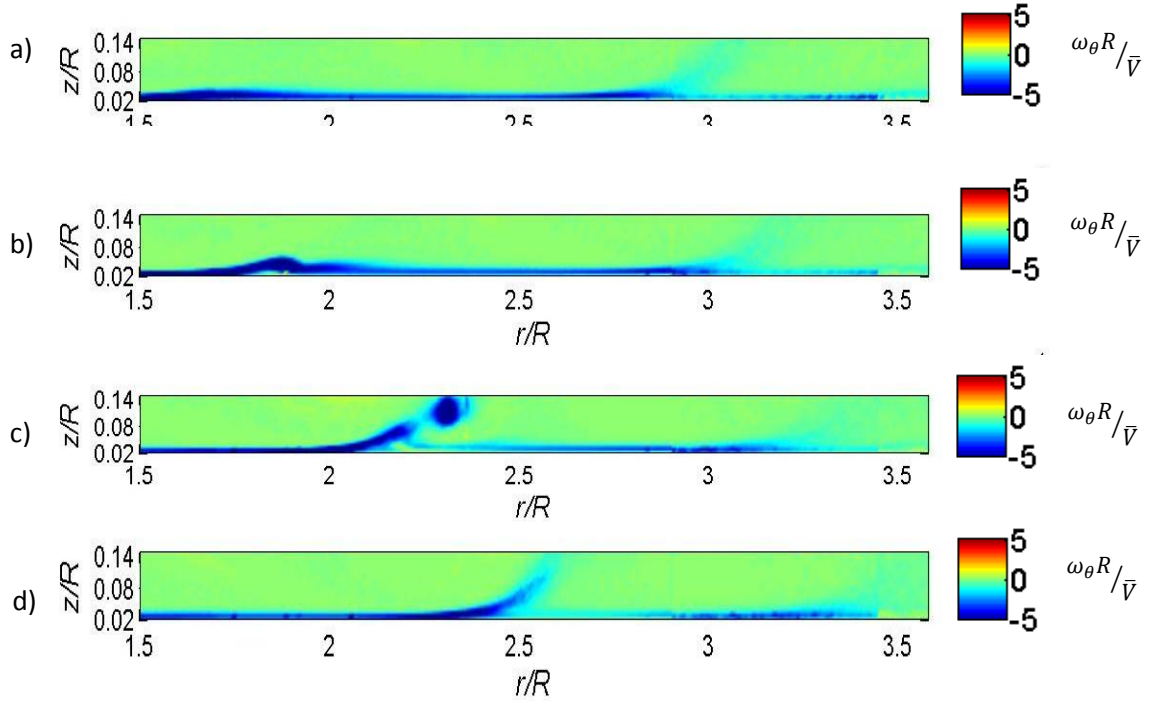


Figure 4.16: HSHR vorticity (θ -direction) is plotted at $t/T = .225, .27, .35$, and $.425$ respectively on a larger scale. The boundary layer is visible as the area of negative vorticity near the ground plane.

which will become important in later discussions of the vortex-ground interaction.

The observations of the velocity and vorticity plots provide insight into the sediment uplift associated with brownout flow. From the experimental data, it is possible to conclude that the vortex is responsible for the highest radial and wall normal velocities, suggesting that the vortices are the most pivotal flow structures for rotorcraft brownout. These results indicate that a reduction in the coherence and circulation of the rotor-tip vortices at the ground plane may be the most effective fundamental mitigation technique for reducing the effect of brownout. As seen in an earlier figures of a rotorcraft hovering over sediment (Figure 2.3 and 2.4), circular erosion patterns are seen in the ground plane. These patterns stem from the increased wall normal velocities at the

interaction point of the primary vortex and the wall. Increased sediment erosion patterns in these circular regimes have been documented by Mulinti and Kiger (2010). In an experiment conducted with the same test set-up as this study, eroded rings were among the first structures noticed in the sediment bed when exposed to forced vortex rings. These rings may alter the sediment uplift patterns in similar ways as the later discussed radial fence introduction, and offer a key insight into a possible factor leading to the initial development and location of the brownout cloud.

Periodic Fluctuations:

A standard triple decomposition can be employed to develop a further understanding of the mechanisms surrounding the observed turbulence in the flow. The triple decomposition separates the effects of periodic and stochastic fluctuations. First, the periodic component of the fluctuations is analyzed, as one would expect these to dominate in a flow largely driven by a highly repeatable structure. The periodic

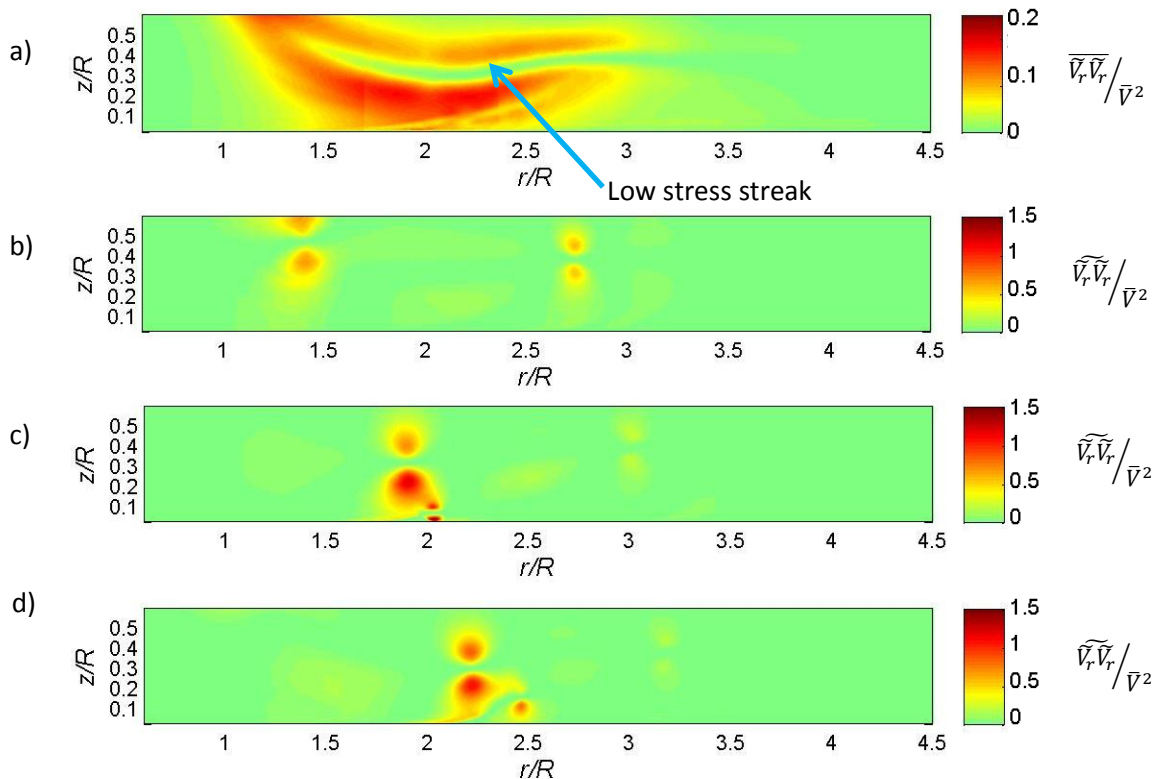


Figure 4.17: HRHS radial normal periodic stresses ($\tilde{v}_r \tilde{v}_r$) are plotted as a time average and ensemble averages at $t/T = .575, .925, \text{ and } .125$ respectively.

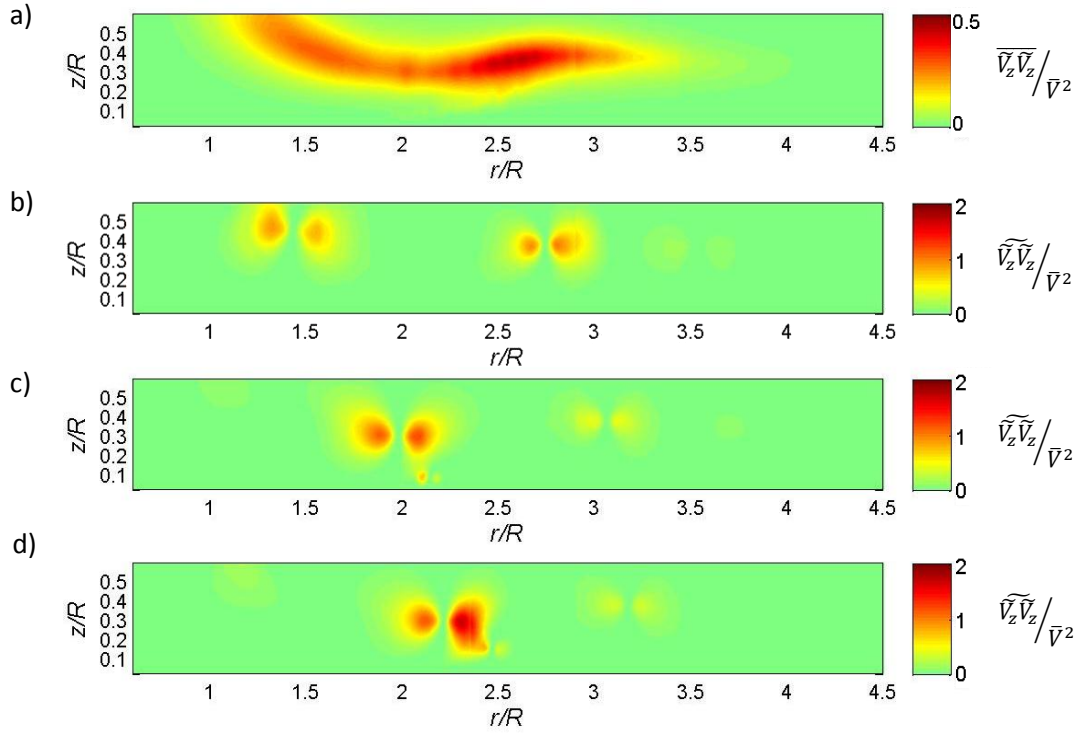


Figure 4.18: HSHR wall normal periodic stresses ($\tilde{v}_z \tilde{v}_z$) are plotted as a time average and ensemble averages at $t/T = .575, .925$, and $.125$ respectively.

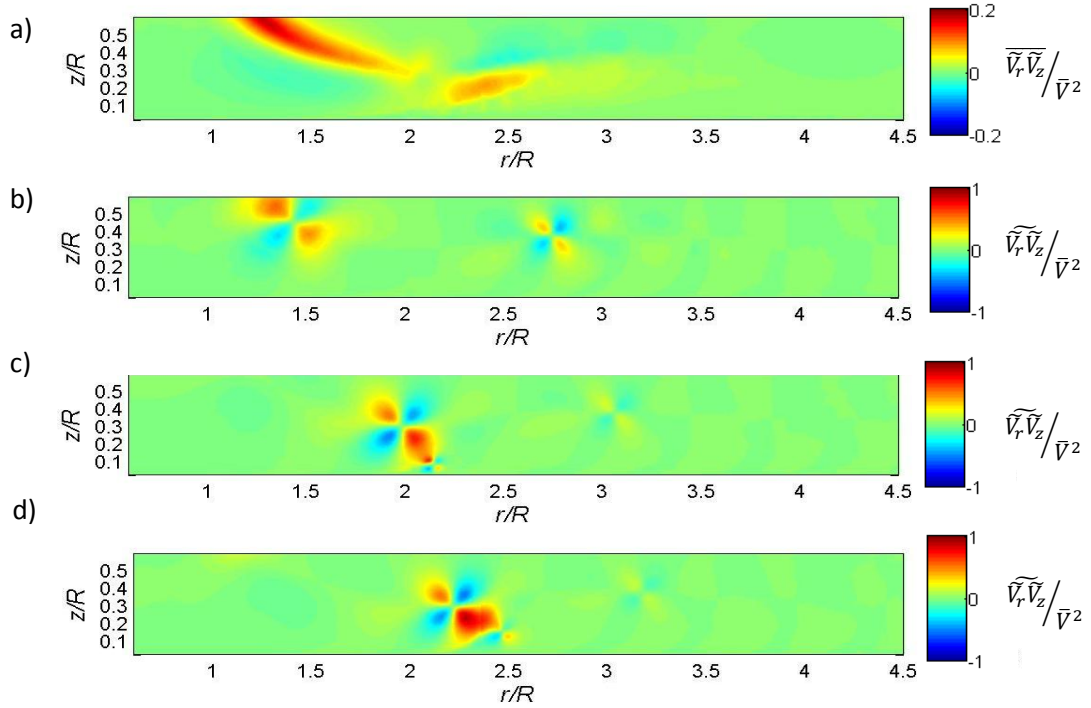


Figure 4.19: HSHR Reynolds shear periodic stresses ($\tilde{v}_r \tilde{v}_z$) are plotted as a time average and ensemble averages at $t/T = .575, .925$, and $.125$ respectively.

fluctuations are broken down into phase averaged events as well as complete time averages for radial normal, wall normal, and Reynolds shear stresses. These periodic Reynolds stresses ($\tilde{V}\tilde{V}/\bar{V}$) are shown in Figures 4.17, 4.18 and 4.19 normalized by the mean jet velocity. Observing the time averaged radial normal stresses, an area of low stress is seen to follow the trajectory of the center of the vortex, surrounded above and below by areas of high stress. The origin of these low and high stress streaks can be accounted for by viewing the individual phase components of the periodic fluctuations. The areas of radial velocity with the highest magnitude (above and below the vortex ring core) are the areas corresponding to the highest velocities induced by the primary vortex. At the core of the vortex, the lack of induced rotation reduces the reported velocities to that of the ring translation velocity. The ring translation velocity fluctuates from the mean velocities significantly less than the induced rotation velocities, as it is only dependant on the forced mean flow. Therefore, the fluctuations about the center of the vortex ring are much smaller than those directly above and below the ring center, so there exists the streak of low periodic fluctuations along the path of the vortex core. A second streak of low fluctuations is in the secondary vortex core, but is not as pronounced. In this area of the flow, vortex jitter is much more dominant, leading to the weakening of structures seen in time and ensemble averages. This phenomenon is not observed in the wall normal fluctuations, as the areas of high induced velocity (radially inwards and outwards of the vortex core) are aligned perpendicular to the path of the vortex.

Observing the individual phase ensemble fluctuations, the primary vortex develops areas of high periodic stresses in the same regions as the corresponding areas in the velocity plots. The secondary vortex is seen to initiate as its own structure with

similar characteristics as the primary vortex, although smaller in size. As the secondary vortex lifts off the ground, the fluctuations closest to the primary ring are integrated into the larger ring, increasing the magnitude of the fluctuations of the primary vortex. This merging of the fluctuation structures is representative of the formation of the high-velocity jet at the center of the vortex dipole. Though the two lobes of fluctuations around the primary ring are initially equal in magnitude, accelerations caused by the wall (i.e., an image vortex ring) and the aforementioned interaction with the secondary ring causes an increase in the fluctuations associated with the positive velocity areas of the vortex ring. The increase in the positive lobe is also seen in both the shear stresses and the wall normal stresses; as they include an initial symmetric stress structure that is unevenly accelerated over time.

From the analysis of the periodic Reynolds stresses, the importance of the vortex-wall interaction in sediment uplift again becomes prevalent. The acceleration of the induced vortex velocities by the wall plane (image vortex) produce significant uplift structures near the wall. Also, the introduction of the secondary vortex and the jet between the vortex dipole increase the stresses near the ground. The primary and secondary vortex introduce the highest vertical stresses seen in the flow, therefore contributing significantly to sediment uplift. A flow with a weaker vortex, or no tip vortex at all, might larger patterns of saltation and scour as opposed to uplift.

Because the interaction of the two vortices is dominated by a random event (the wrapping of the secondary vortex around the primary), the magnitude of the periodic fluctuations drastically reduces once the primary and secondary ring interact. This reduction is brought on by the increase of jitter in the flow after the ground interaction.

Vortex jitter reduces the strength of the ensemble averaged structures and, therefore, the effects these structures have on the periodic fluctuations. The wall normal stresses have the highest magnitude of the three discussed periodic stresses, with an ensemble peak magnitude 33% greater than the radial normal stresses, and a time average peak that is 150% greater. The increase in the wall normal fluctuations compared to the radial fluctuations can be accounted for by the fact that at the strongest area of interaction between the primary and secondary vortices (i.e., immediately after the formation of the secondary vortex), each vortex is forcing the other upwards. This dipole interaction offsets the normally equal periodic fluctuations demonstrated by a circular vortex core.

Stochastic Fluctuations:

Examining the stochastic fluctuations illuminates the Reynolds stresses not caused by the periodic structures in the flow. The stochastic fluctuations can be viewed instantaneously, as phase averages, or time averages across an entire forcing period. Because the data is the result of multiple image planes being mosaiced together, visualization of the instantaneous events is reasonable within the subframe in which the original data was captured (each plane captures a different vortex event.) The structures seen in the phase averaged stochastic fluctuations (Figure 4.20) are much more irregular than their periodic counterparts. The peak magnitudes of the stochastic stresses are significantly lower than the periodic fluctuations; slightly less than an order of magnitude lower. The wall normal stresses peak at about 66% higher than the radial stresses, suggesting that higher fluctuations occur normal to the wall, either uplifting or bombarding sediment into the flow. The stochastic fluctuations are mainly present in the area of the flow most dominated by jitter, between $2 < r/R < 4$. The diminishing of the

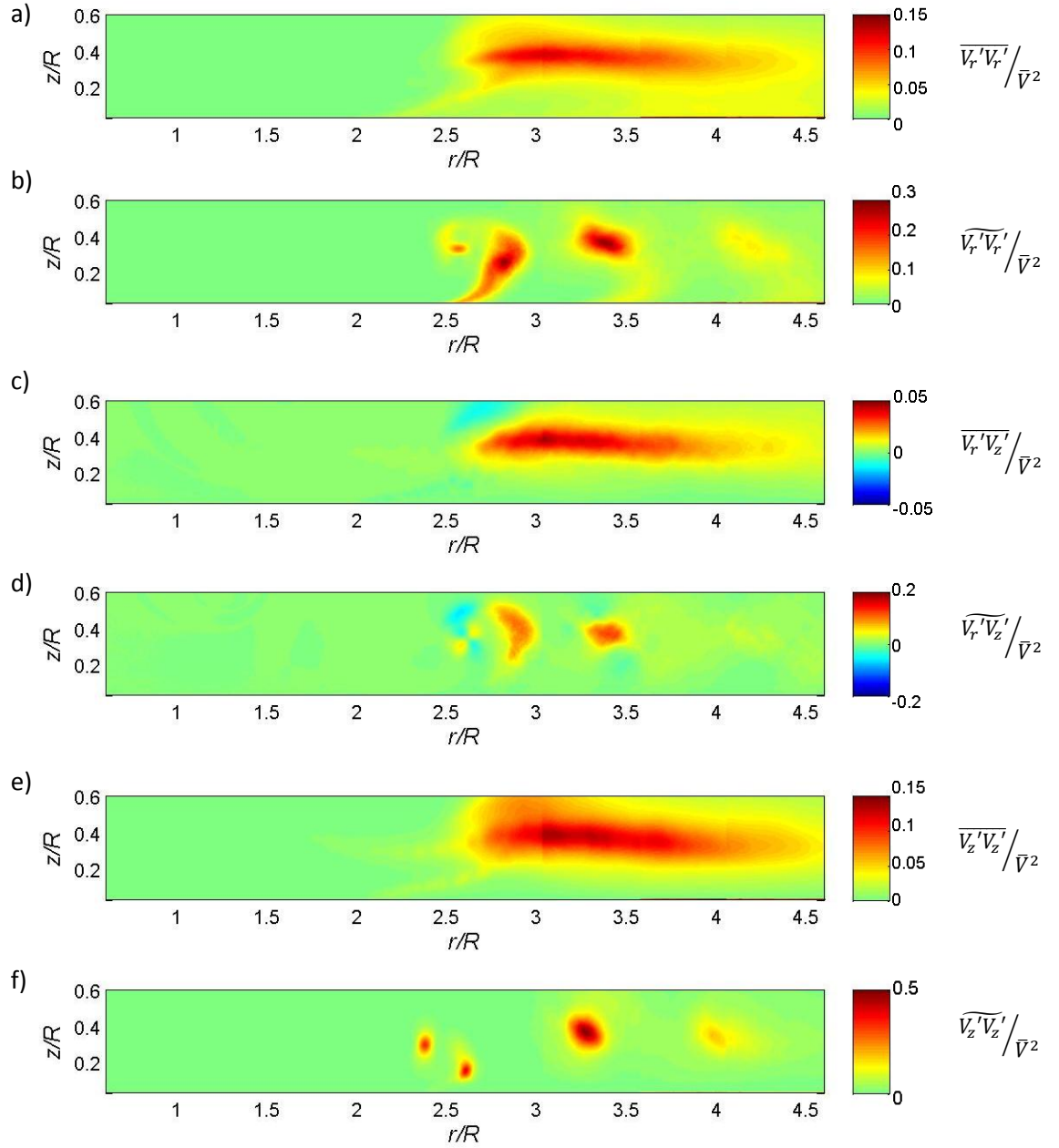


Figure 4.20: HSHR stochastic stresses are shown. From top to bottom, the images show time averaged radial stresses $\overline{V_r'V_r'}$, ensemble averaged radial stresses $\widetilde{V_r'V_r'}$ at $t/T=.3$, time averaged shear stresses $\overline{V_r'V_z'}$, ensemble averaged shear stresses $\widetilde{V_r'V_z'}$ at $t/T=.3$, time averaged wall normal stresses $\overline{V_z'V_z'}$, and ensemble averaged wall normal stresses $\widetilde{V_z'V_z'}$ at $t/T=.15$.

periodic stress by the jitter coupled with an increase in stochastic fluctuations in this region brings the periodic and the stochastic stresses to similar magnitudes, and eventually, forces the stochastic stresses to overtake the periodic fluctuations. Outside this area, the stochastic fluctuations are attributed to turbulence in the flow in the absence of a strong vortex structure. The ensemble averaged stochastic fluctuations show a larger structure corresponding to the area dominated by the secondary vortex. This increase in event size is contributed to the jitter of the secondary vortex being much larger than that of the primary. The wrapping of the secondary vortex around the primary is an azimuthally unstable event, leading to the secondary vortex appearing at different locations in each instantaneous cut-plane of the ring, and thusly adding to the stochastic fluctuations.

Low Speed Data:

Velocity and vorticity:

The analysis of the low speed data will focus on the differences between the low and high speed sets, as the majority of the features produced by these flow conditions are similar. The primary differences are ones due to scaling of viscous effects from the lower Reynolds number associated with the lower speed flow, which can be expected to have two possible effects: 1) an increase in relative size because of the increased influence of viscous diffusion at lower Re conditions, and 2) a decrease in the growth rate of the three-dimensional structures, again because of the increased stabilization effects of viscosity. After analysis of the ensemble average velocities, both the radial and wall normal components of the velocity show similar structures to the high speed data (with

similar magnitudes after normalization by the mean jet exit velocity). However, in the low speed data the secondary vortex presents with an increased ensemble average strength, an observation initially contradictory to the previous studies by Walker *et al.* (1897), whose results suggest an increase in secondary vortex strength with an increase in Reynolds number. This apparent increase in vortex strength, however, is in reality an artifact from smearing in the ensemble averages brought on by jitter in the higher Reynolds number case. The increase in Reynolds number of the flow reduces the damping of the fluctuations in the vortex leading to jitter.

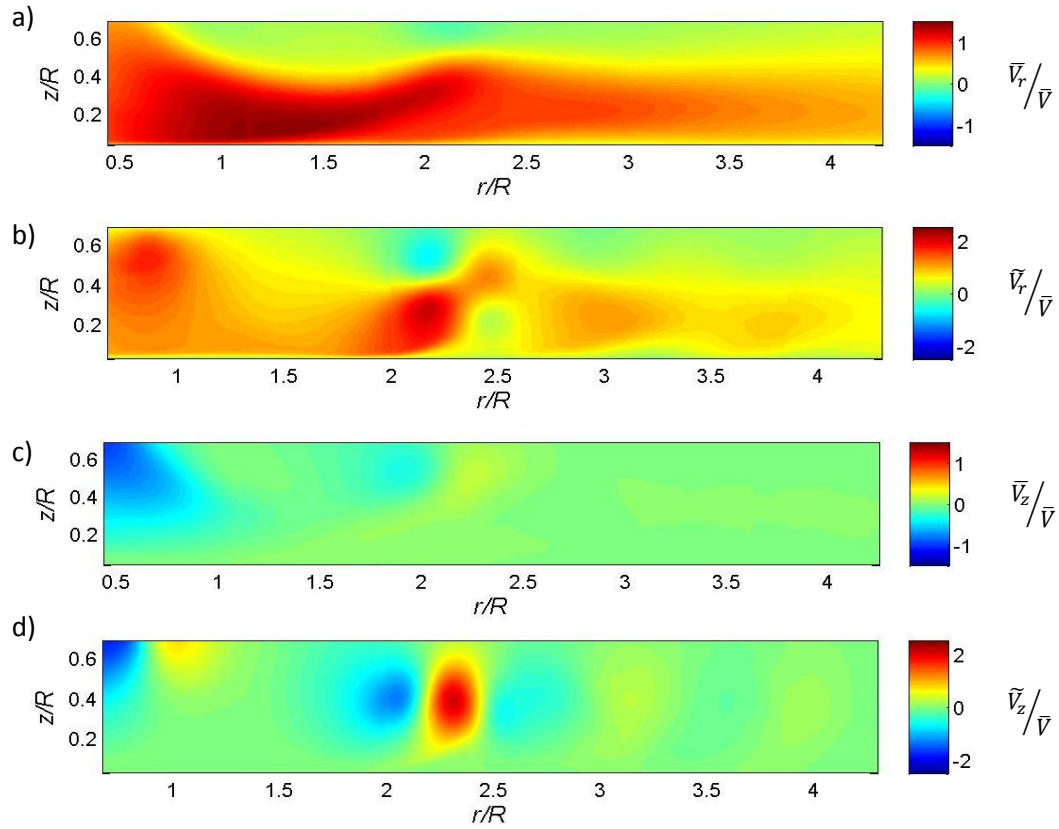


Figure 4.21: Velocities from LSHR. From top to bottom, the images show time averaged radial velocity (\bar{V}_r), ensemble averaged radial velocity (\tilde{V}_r) at $t/T=0.025$, time averaged wall normal velocity (\bar{V}_z), and ensemble averaged wall normal velocity (\tilde{V}_z) at $t/T=0.025$

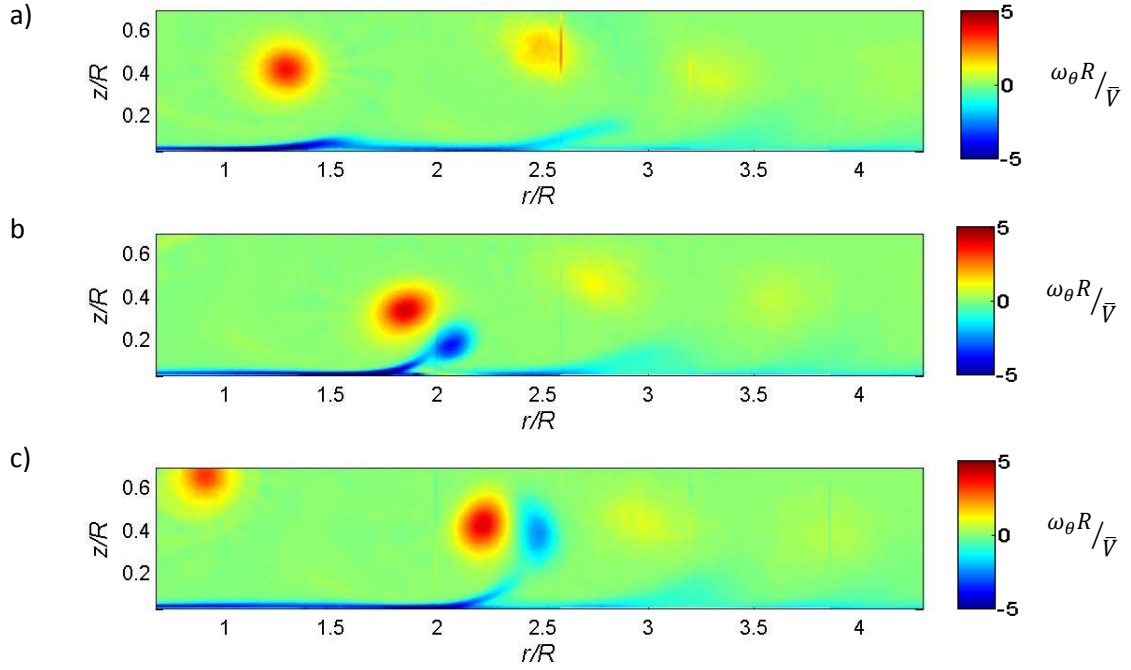


Figure 4.22: LSHR vorticity (θ -direction) is plotted at $t/T = .45, .85$, and $.075$ respectively. In each image, three separate vortex events are visible.

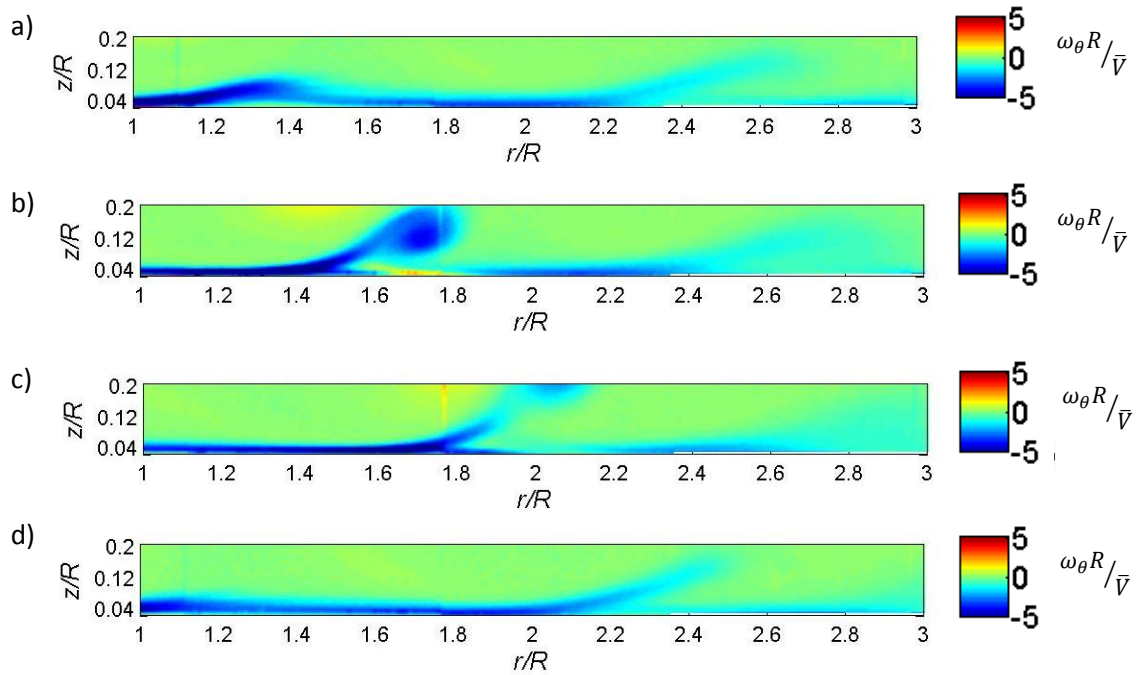


Figure 4.23: LSHR normalized vorticity (θ -direction) is plotted at $t/T = .225, .27, .35$, and $.425$ respectively on a larger scale. The boundary layer is visible as the area of negative vorticity near the ground plane.

Observing the vorticity of the low speed flow, qualitatively similar structures are exhibited. The forced boundary layer forms a secondary vortex and a rebound occurs, leading to the flow being dominated by jitter. A closer look at the ground plane of the low speed flow illuminates a significant variation between the two data sets. The boundary layer of the low speed conditions is twice as thick as its high speed counterpart ($0.05R$ vs $0.025R$), leading to the rollup of a larger secondary vortex with respect to the primary core. The secondary vortex formed in the low speed conditions has a peak ensemble averaged radius of approximately 71% of the primary core, as opposed to the high speed conditions which produce a ratio of 53%.

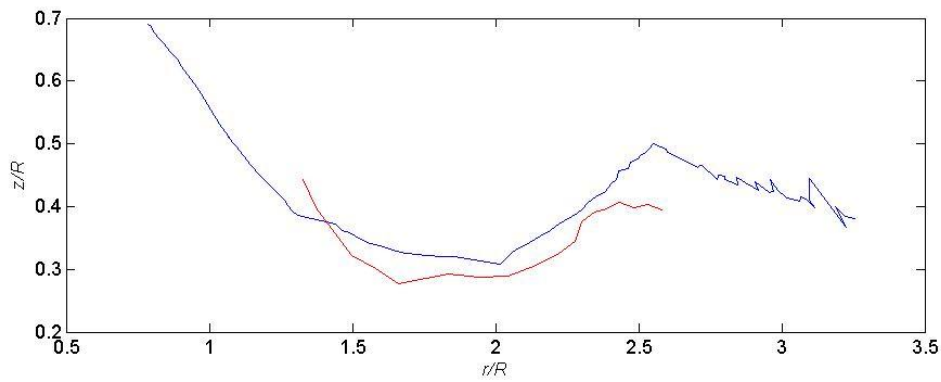


Figure 4.24: A comparison of the trajectory of the high speed (red) and low speed (blue) vorticity

Tracking the trajectories of both vortices was conducted with the vortex identification algorithm previously discussed. The results of this tracking are seen in Figure 4.24. The figure demonstrates that the trajectories of the vortices are qualitatively similar as both vortex rings approach the ground at the same location. As expected, the higher Reynolds number vortex travels closer to the ground. This trajectory was predicted by Walker *et al.* 1987 noting that the higher the Reynolds number, the closer

the vortex follows a hyperbolic trajectory to the ground before forming a secondary vortex.

Periodic Stresses:

The periodic stresses of the low speed data (Figures 4.25, 4.26, and 4.27) are similar to the high speed data in shape and magnitude. Some slight variations in the periodic fluctuations are seen in the time averaged radial stresses. Though both high and low speed images show a low stress streak following the trajectory of the primary core, the streak is slightly shorter in the low speed data. In the high speed radial stress average, the streak is seen to extend across an area of $r/R \approx 1.5$, as compared to an approximate

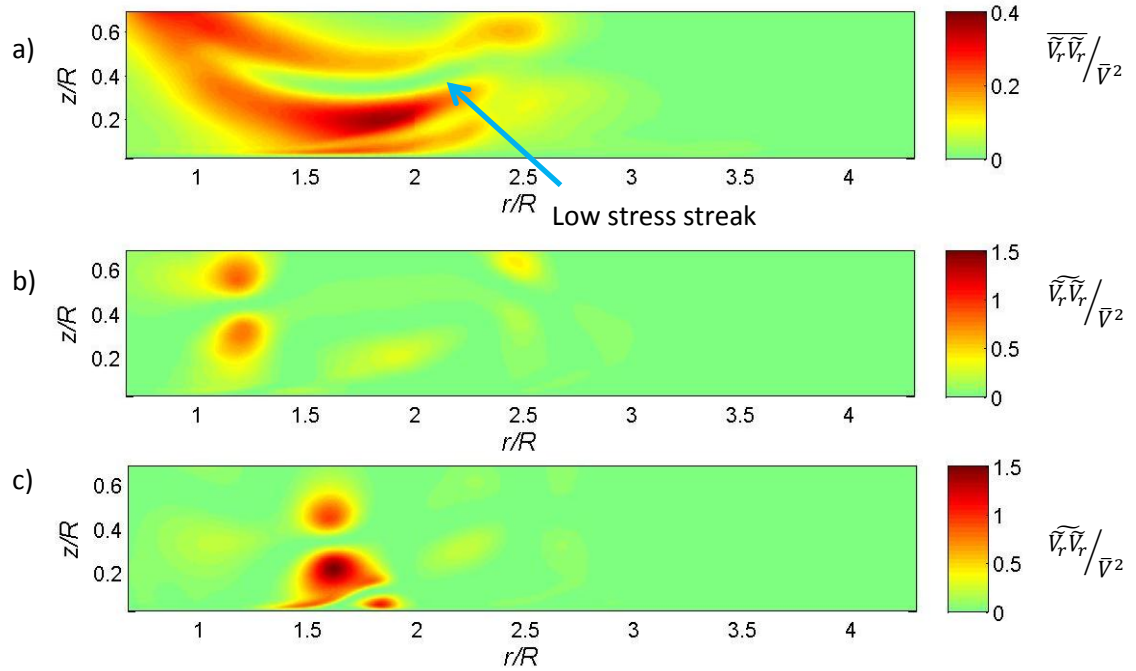


Figure 4.25: LSHR periodic radial normal stresses ($\tilde{V}_r \tilde{V}_r$) are plotted as a time average and at $t/T = .325$ and $.7$ respectively

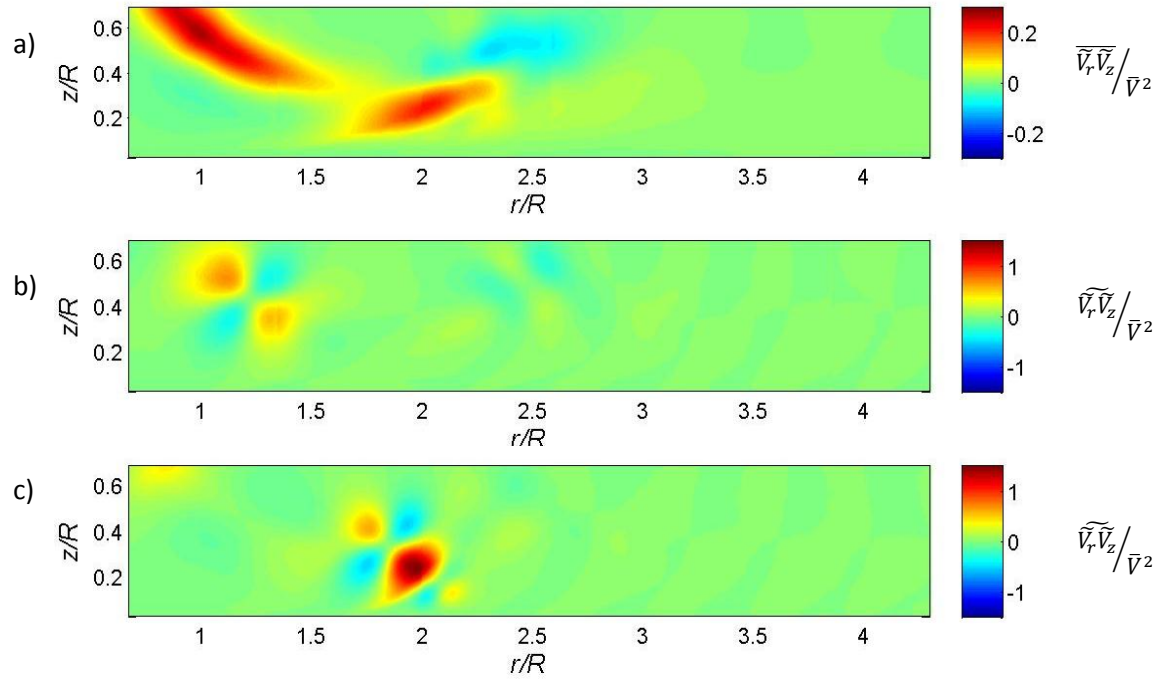


Figure 4.26: LSHR periodic Reynolds stresses ($\tilde{v}_r \tilde{v}_z$) are plotted as a time average and at $t/T=.325$ and $.7$ respectively

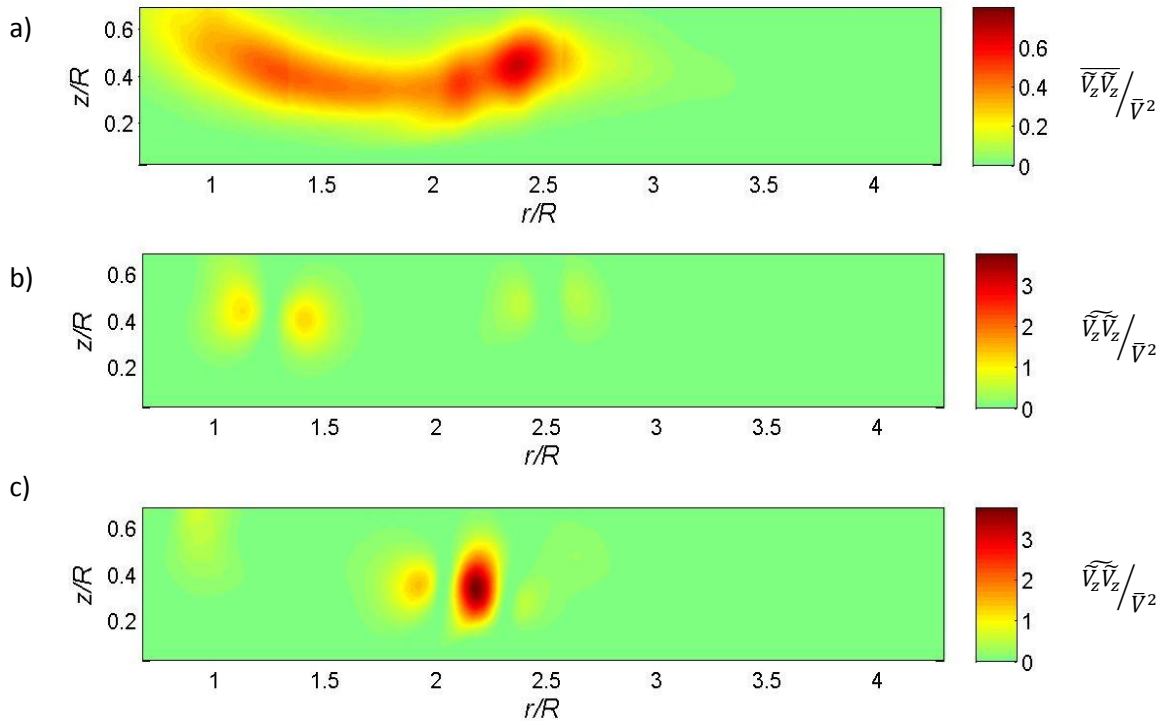


Figure 4.27: LSHR periodic wall normal stresses ($\tilde{v}_z \tilde{v}_z$) are plotted as a time average and at $t/T=.325$ and $.7$ respectively

streak length of $1R$ in the low speed data. This difference stems from the convection speed of the vortex ring during the ground interaction. The slower co-flow of the low speed data compresses the radial region at which the interaction occurs, creating similar structures of stress existing in shorter regions of the flow. The same phenomenon is seen in the wall normal stresses, with the area of high stress being compressed from a region of approximate length $2R$ down to $1.5R$.

Stochastic Fluctuations

The stochastic fluctuations demonstrate the largest variation between the stresses seen in the high and low speed data sets. The stochastic data exhibits the most variance in magnitude between the high and low speed data sets, with the low speed values producing a 50% dropoff in the wall normal Reynolds stresses between the high and low speed conditions. There also exists a change in the structures in the stochastic stresses between the test conditions. In the low speed data, the stress structures are less coherent; they are smeared in the ensemble averaging and show significantly less definition in the time averaging. To understand this smearing, the jitter in the low speed data is analyzed and compared with the high speed conditions.

Figure 4.29 displays the instantaneous positions of the primary vortex core for the low speed (blue) and the high speed (red) rings. The low speed vortex jitter appears to manifest as random fluctuations of the core, i.e. the primary core location is dispersed randomly in a circular pattern. The high speed ring, on the other hand, mainly fluctuates with the streamlines of the average velocity. A bias in the fluctuations can be derived from the influence of the mean flow on the downstream jitter. Small variations in the

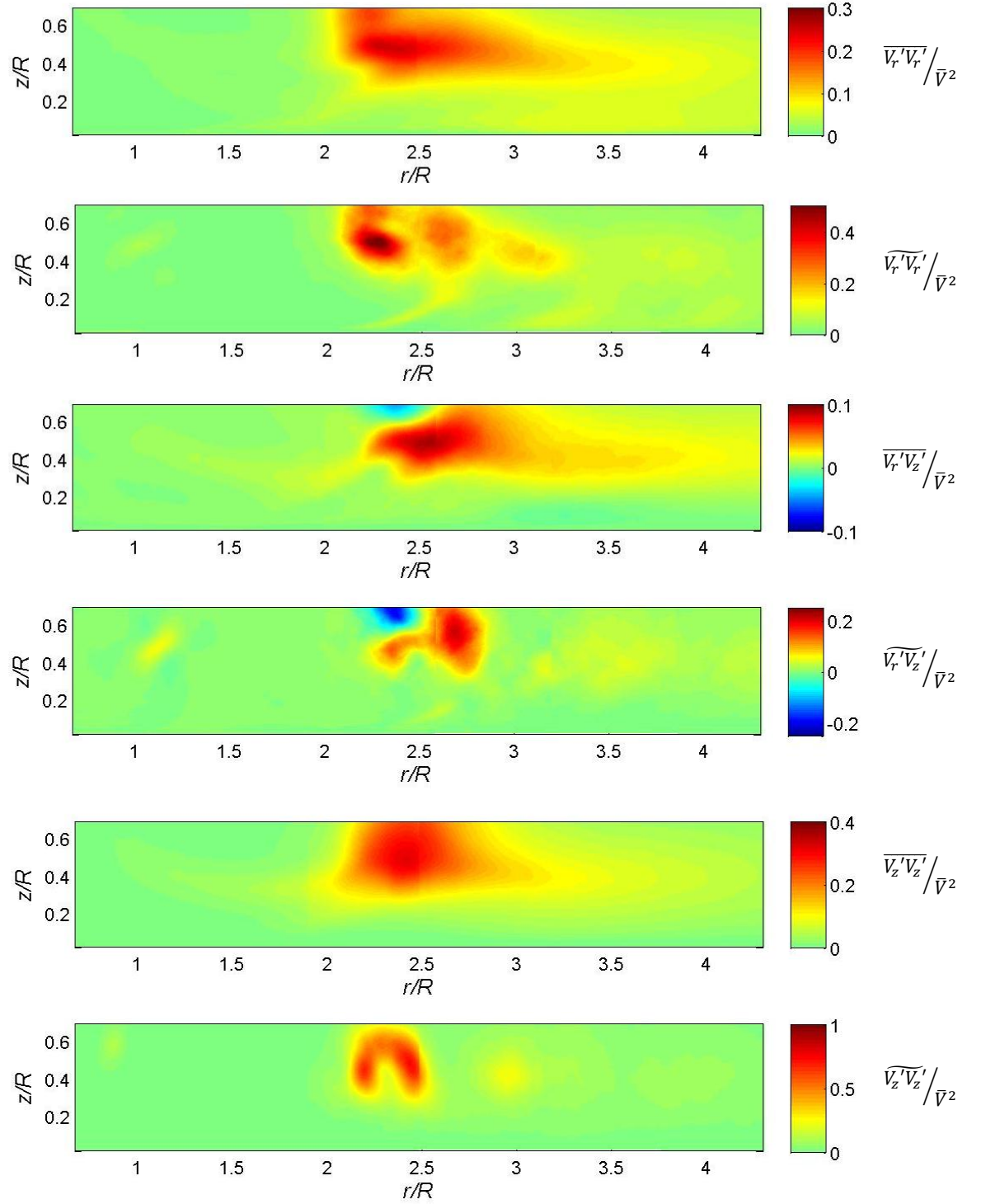


Figure 4.28: LSHR stochastic stresses are shown. From top to bottom, the images show time averaged radial stresses $\overline{V_r'V_r'}$, ensemble averaged radial stresses $\widetilde{V_r'V_r'}$ at $t/T = 0.3$, time averaged shear stresses $\overline{V_r'V_z'}$, ensemble averaged shear stresses $\widetilde{V_r'V_z'}$ at $t/T = 0.3$, time averaged wall normal stresses $\overline{V_z'V_z'}$, and ensemble averaged wall normal stresses $\widetilde{V_z'V_z'}$ at $t/T = 0.15$.

position of the high speed vortex core are grown by the relatively strong mean flow accompanying the ring. The low speed conditions have a much weaker mean flow, and therefore do not exhibit this bias. This bias in the fluctuations leads to the increase stochastic fluctuation coherence in ensemble averaging for the high speed test conditions. As the high speed vortex jitter is biased along the streamlines of the mean-flow, it can be assumed that the jitter is more influenced by the mean flow. In the low speed jitter, however, is evenly distributed in a random pattern, leading to the conclusion that inequalities in vortex generation and instabilities in the dipole interactions are the dominant contributors in jitter. The general shape of the jitter will alter the appearance of the ensemble fluctuations, as mentioned earlier in the discussion of the effects of jitter on structures of Reynolds stresses.

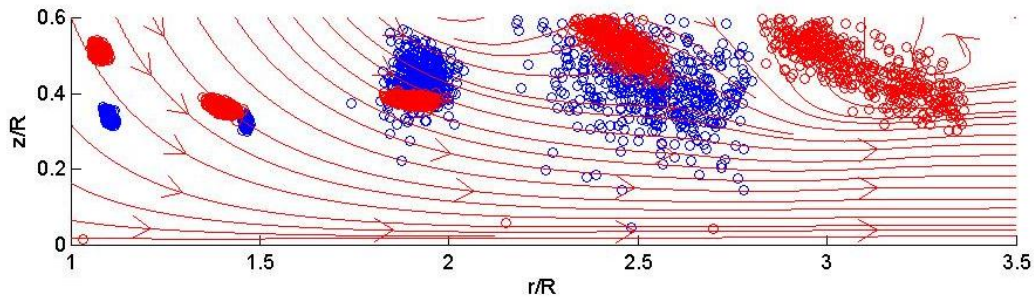


Figure 4.29: The centroid of the vortex ring for the high speed data (red) and the low speed data (blue) as time progresses accompanied by streamlines of time averaged high speed velocity

Profile Decomposition:

To obtain a more quantitative view of the effect of the vortex rings on the turbulence of the mean flow, profiles of the fluctuation velocities must be analyzed. Vertical profiles of the periodic fluctuations at different phases and radial locations are examined. These profiles are seen in Figures 4.30, 4.31, and 4.32.

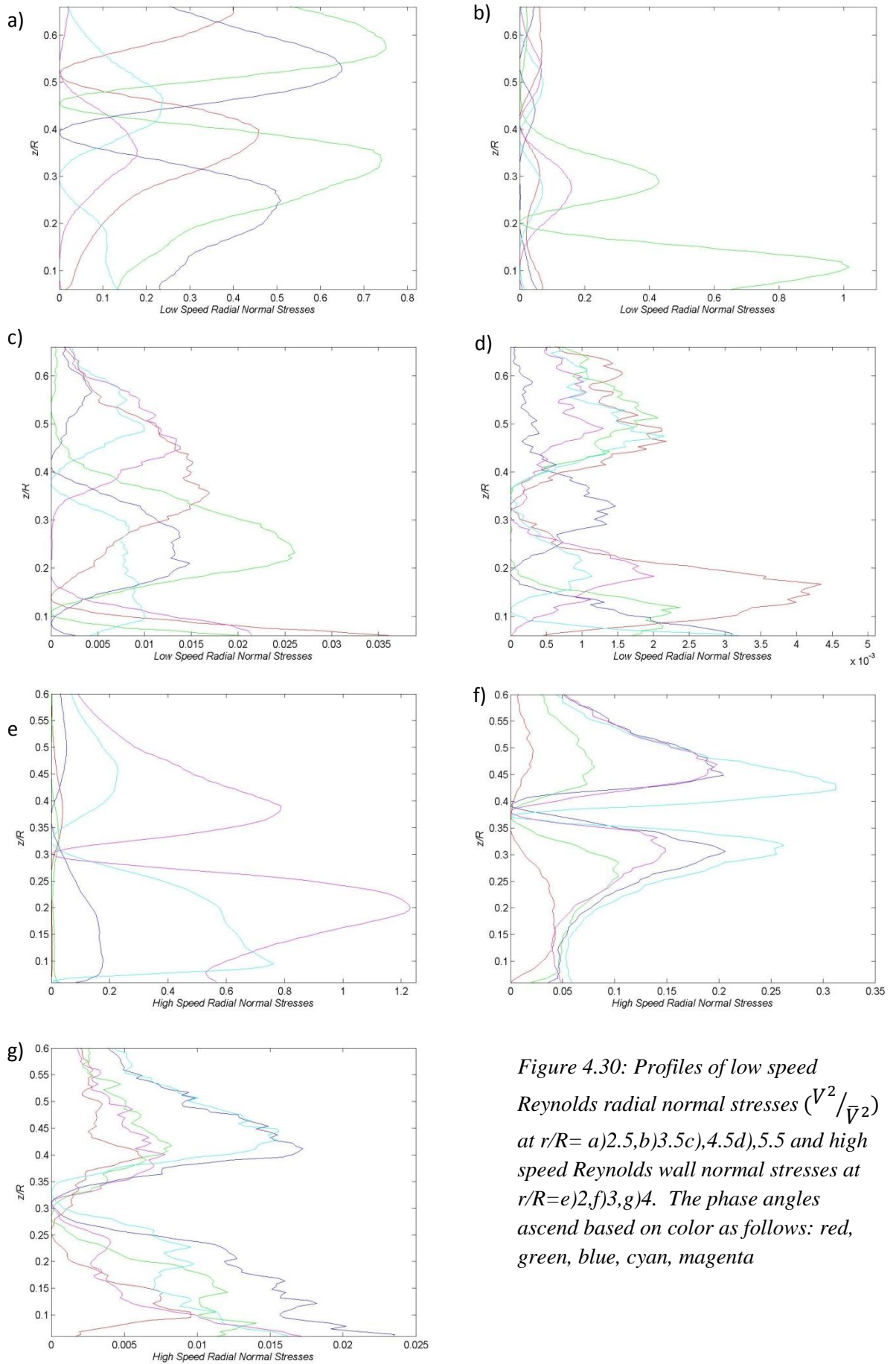


Figure 4.30: Profiles of low speed Reynolds radial normal stresses (V^2/\bar{v}_2) at $r/R=$ a)2.5,b)3.5c)4.5d)5.5 and high speed Reynolds wall normal stresses at $r/R=$ e)2,f)3,g)4. The phase angles ascend based on color as follows: red, green, blue, cyan, magenta

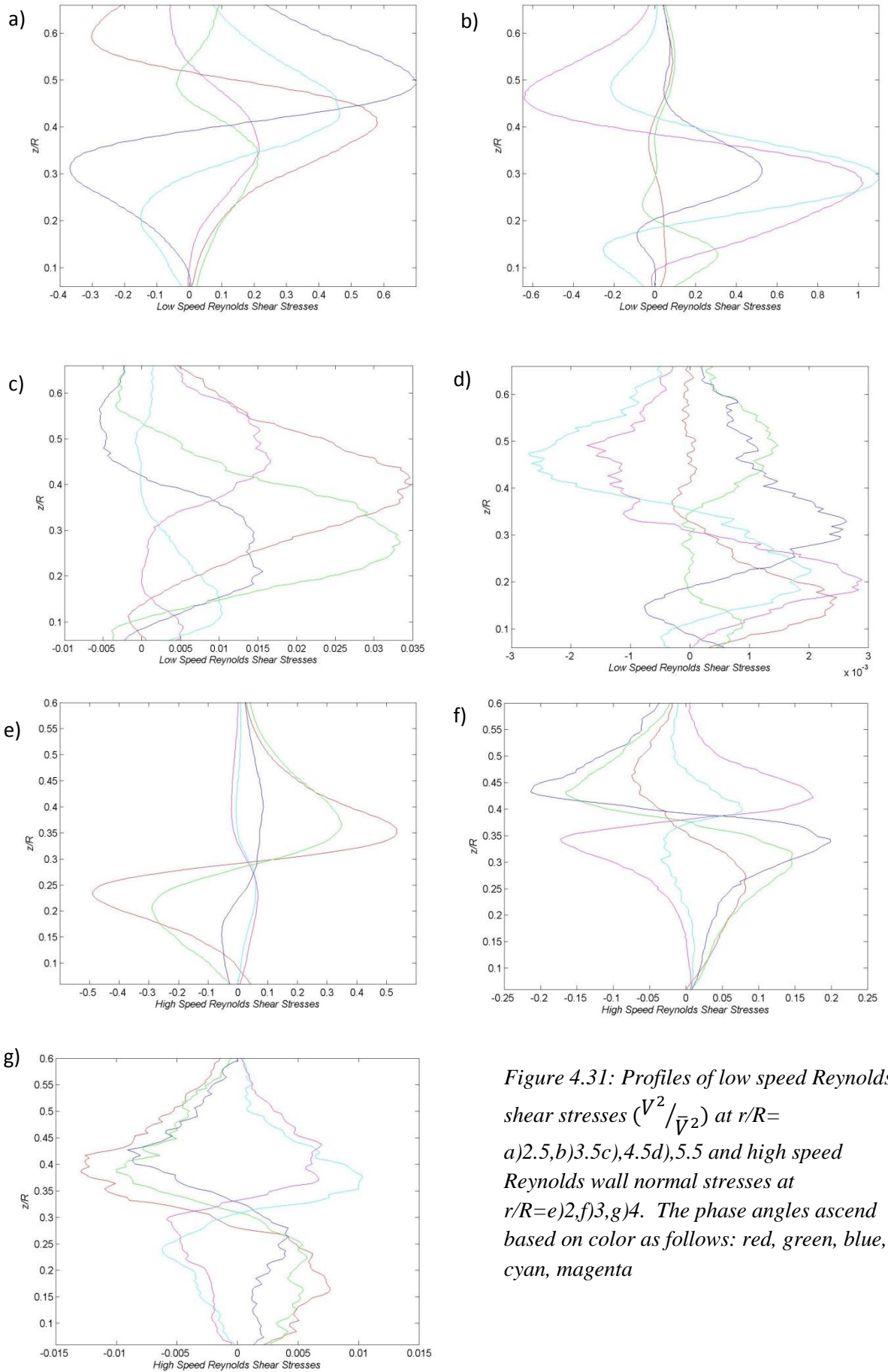


Figure 4.31: Profiles of low speed Reynolds shear stresses (V^2/\bar{v}_2) at $r/R=$ a)2.5,b)3.5c),4.5d),5.5 and high speed Reynolds wall normal stresses at $r/R=e)2,f)3,g)4$. The phase angles ascend based on color as follows: red, green, blue, cyan, magenta

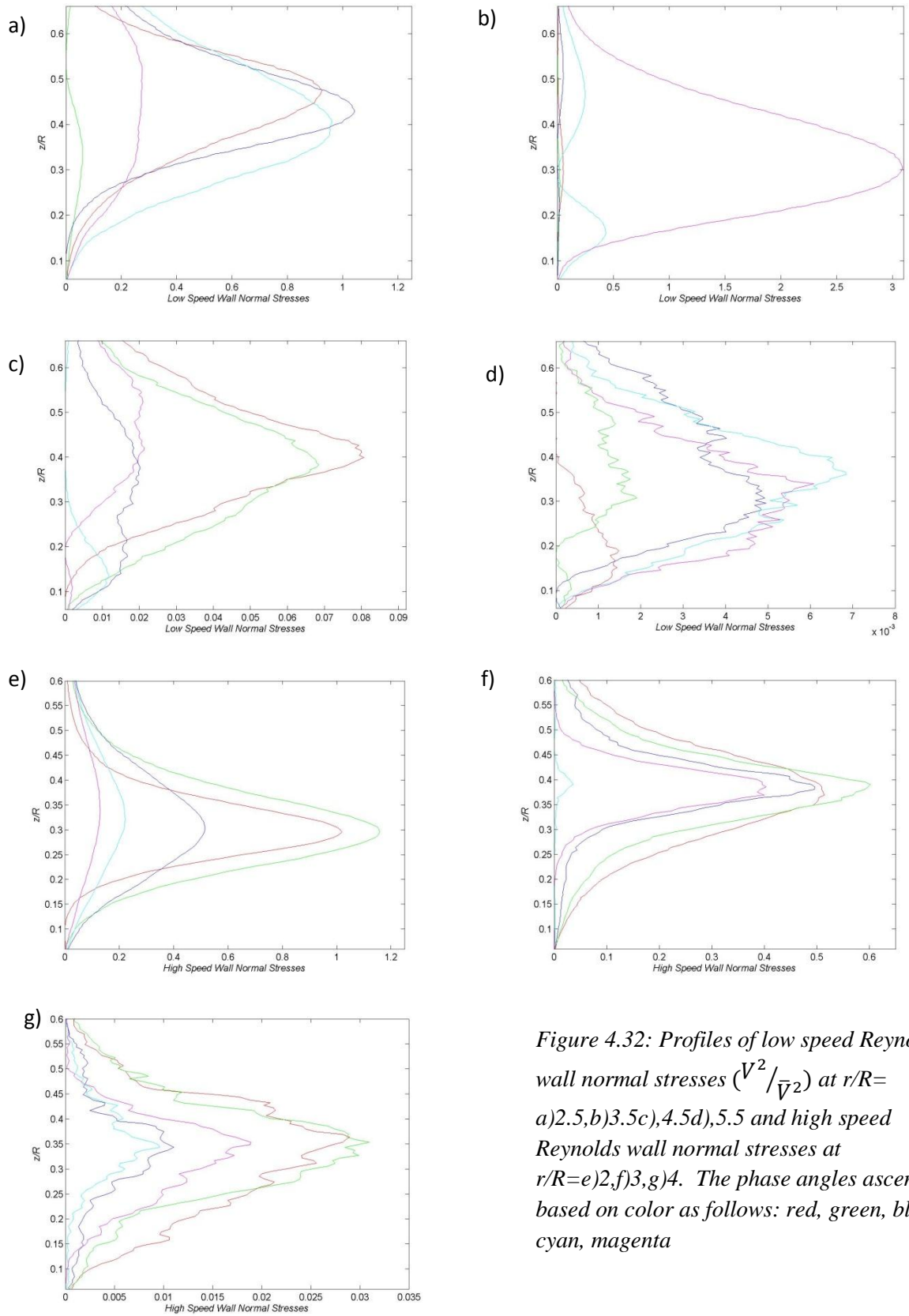


Figure 4.32: Profiles of low speed Reynolds wall normal stresses (V^2/\bar{V}_2) at $r/R=$ a)2.5,b)3.5,c)4.5,d)5.5 and high speed Reynolds wall normal stresses at $r/R=e)2,f)3,g)4$. The phase angles ascend based on color as follows: red, green, blue, cyan, magenta

The periodic profiles at different phases illuminate the influence of the periodic structure (i.e., the forced vortex ring) on the area of interest at given phase angles. These fluctuations are depicted in Figure 4.30. The profiles show at the initial radial location ($r/R=2$ for high speed and $r/R=2.5$ for low speed), the vortex ring has a pronounced effect on the flow. The profiles are smooth and show three individual peaks at the phases influenced by the vortex ring. The upper two peaks are equal in magnitude and come from the two areas of high fluctuations depicted in the surface plots previously discussed. The third peak (closer to the ground plane) is the increase of fluctuations brought on by the formation of the secondary vortex and is significantly smaller than the upper two. The profiles radially outward of this position begin to differ between the high and low speed sets. At the next radial location, the high speed radial normal periodic fluctuations decrease while in the low speed data, these fluctuations increase. This difference indicates that the high speed vortex ring begins to encounter the effects of jitter (a reduction in coherent fluctuations) sooner than the low speed ring, a theory supported by the findings shown in Figure 4.29.

The next radial position sees a drop in both the high and low speed periodic radial fluctuations. Though the peak shrinks significantly at this location, the general shape of the fluctuation profiles remains the same, suggesting that the vortex ring still greatly influences the flow. Also in this area of the flow, the effects of jitter begin to become more apparent in the profiles. Contrary to the previously seen smooth profiles, these profiles appear wavy, suggesting they are less converged than the earlier radial positions. The next outward radial location was not obtained for the high speed conditions, but in the low speed data shows further deterioration of the influence of the vortex ring. The

profiles of the periodic fluctuations in this section appear random in nature, and miniscule in magnitude. This pattern indicates the flow field follows the time average flow in this region, and the primary vortex is no longer significantly accelerating its surroundings. These profiles appear less converged than the previous set, suggesting that the fluctuations are even more random in this area of the flow.

The profiles generated for the shear periodic Reynolds stresses and the wall normal periodic Reynolds stresses are plotted in Figures 4.31 and 4.32. The patterns exhibited in the profiles progressing radially outward are similar to those described in the radial normal Reynolds stresses, i.e. the profiles lose coherence as their radial location increases. The major difference seen in these two components of the stresses are the general shape of the profiles. The wall normal periodic Reynolds stresses show two distinct peaks instead of the three peaks seen in the radial velocity. The lack of a third peak stems from the direction of the profiles. In the radial fluctuations, the profiles include two peak areas of fluctuations (above and below the vortex ring). For the wall normal stresses, the peaks of velocity occur in front of and behind the vortex ring, preventing them both from affecting the wall normal direction profiles simultaneously. The Reynolds shear stresses differ in that they include the negative fluctuation values seen as a result of the rotation of the vortex ring. The relative size of the positive and negative components of the radial and wall normal velocities caused by the vortex rotation in relation to the magnitude of the mean flow determines the overall sign of the Reynolds shear stresses.

An important conclusion gathered from the profiles of the coherent stresses is the coherent effect of the forced vortex ring on the flow. The strength of the vortex ring

leads to its initial domination of the flow field, however dissipation of energy into smaller scale structures eventually erodes the influence of the primary ring. Previous literature (Walker *et al.* 1987 Didden and Ho 1985) suggests that the interaction with the secondary vortex increases the dissipation rate of the primary vortex. This idea is supported by the general trend in the circulation seen in Figure 4.9 as well as the large decreases in Reynolds stresses documented in the profiles (Figures 4.30, 4.31, and 4.32). The decrease in coherent vortex influence of the flow leads to smaller sediment uplift forces associated with the vortex.

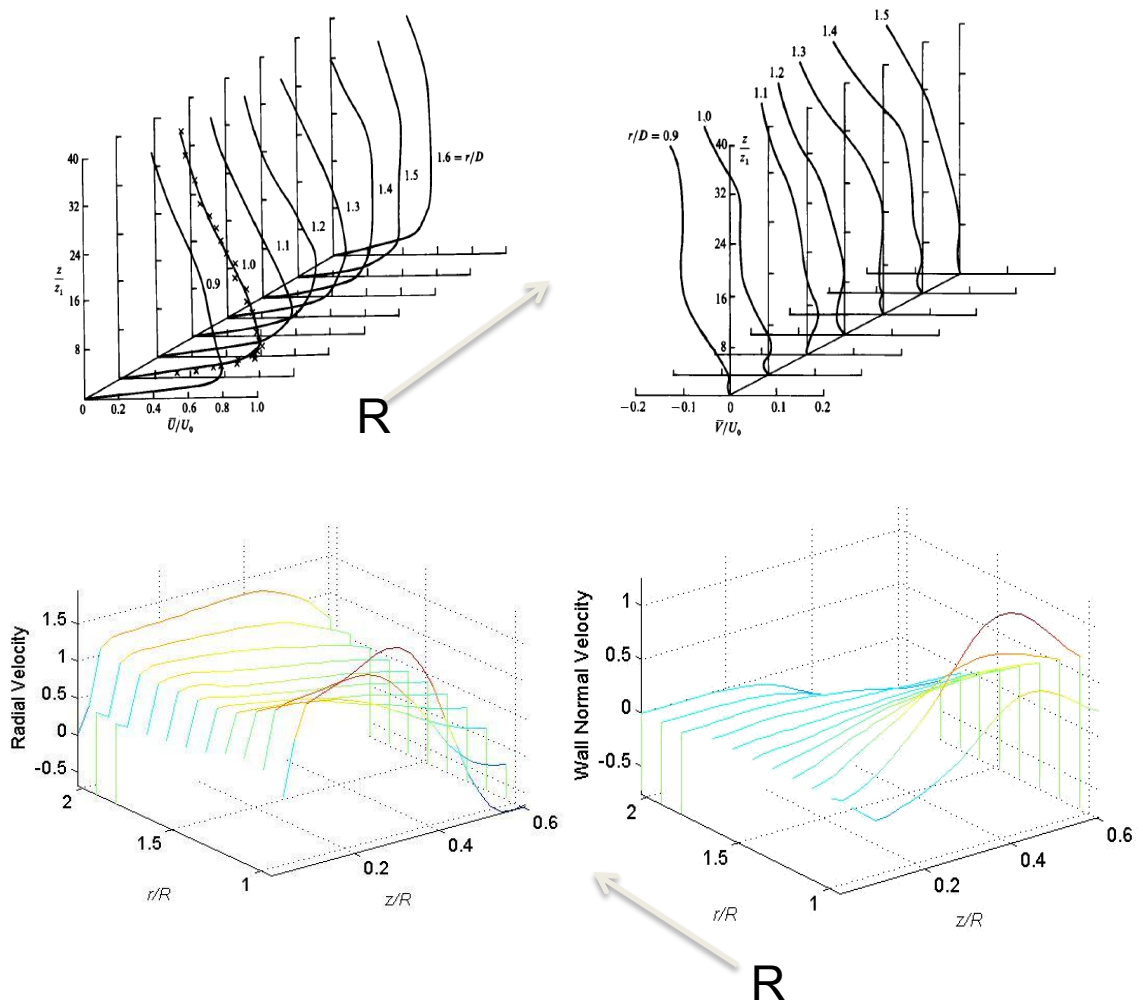


Figure 4.33: Waterfall profiles of radial normal (left) and wall normal (right) velocity from the experiments of Didden and Ho, 1987 (top) and this study (bottom)

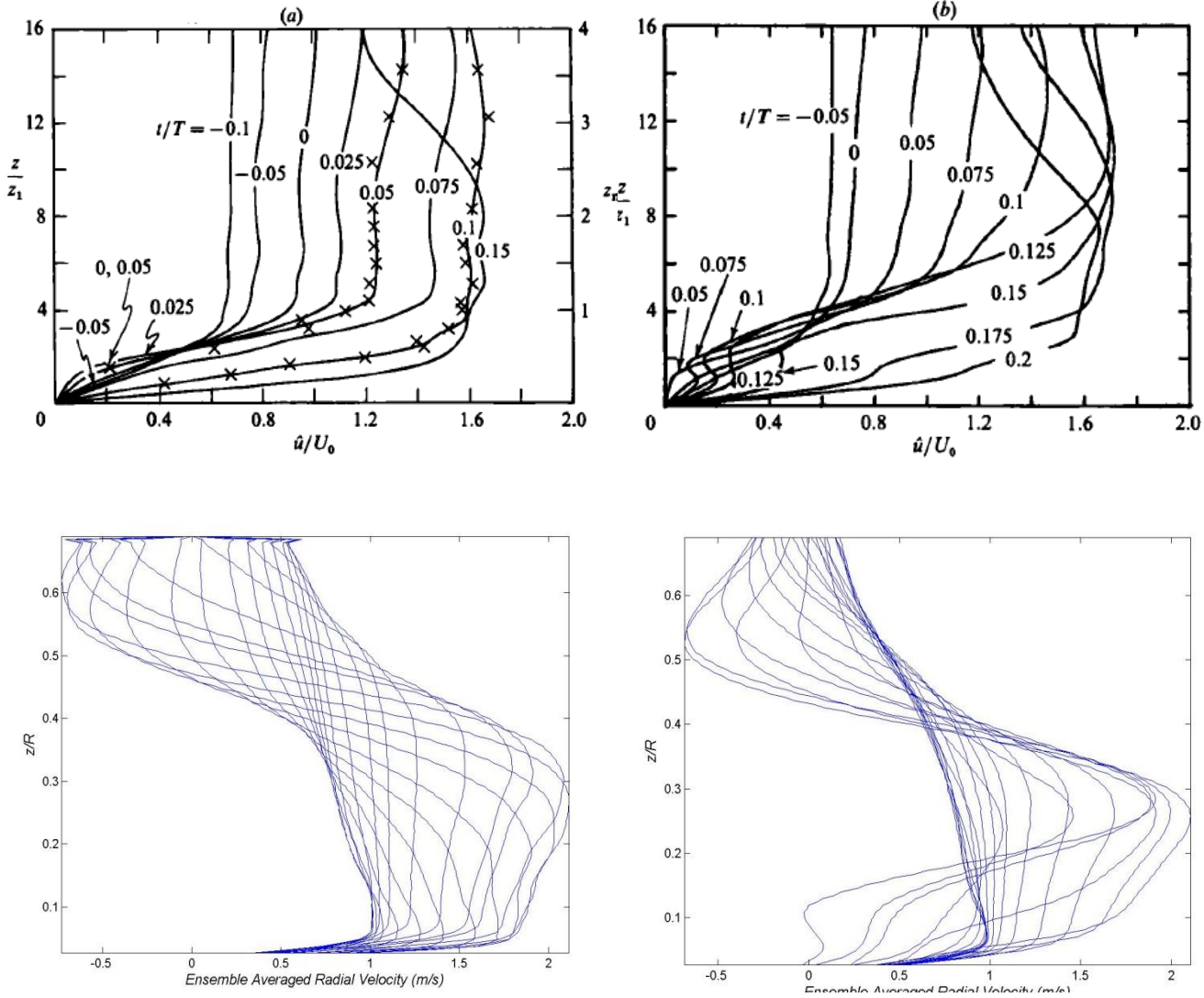


Figure 4.34: Detailed profiles of radial normal velocity from at the point of vortex-ground contact (left) and separation (right) in the experiments of Didden and Ho, 1987 (top) and this study (bottom). In the later radially outward profiles, the point where the vertical gradient of the radial velocity is zero is known as the unsteady separation point

Profiles of velocity can be used for validation of the experimental facility and test conditions with those of the previous literature. Didden and Ho (1985) detailed the presence of a vortex ring creating a wall jet in terms of the radial and wall normal velocities. For the purposes of data comparison, the low speed data will be analyzed, as it is more comparable to the experimental conditions seen in Didden and Ho's work. The

first reported data involved the depiction of radial and wall normal velocities at different radial positions. Their findings compared to similar quantities obtained from this study are shown in Figures 4.33. The radial average velocities close to the interaction point of the vortex form a positive peak close to the wall that eventually transitions into a stable positive plateau, similar to the figures presented in Didden and Ho's research. The peak represents the high speed wall jet formed under the vortex ring, where the plateau represents the smearing of this acceleration during the rebound. The wall normal velocities are mostly negative, especially in the upper portions of the flow, corresponding to the impinging velocity of the jet. As Didden and Ho first reported, there exists a region of negative velocity in the flow, corresponding to the separation region. Also displayed by Didden and Ho were detailed overlaid plots of this ensemble averaged radial velocity. These plots are generated for the data in this study and seen (Figure 4.34). The waterfall plots agree well with Didden and Ho's finding, showing initially a stable peak in the radial velocities where the flow is not separated. As the vortex progresses radially outwards, a significant vertical gradient is seen near the wall. As the gradient increases, there exists a point where $\partial V_r / \partial z = 0$ referred to as the unsteady separation point. The data from this study agrees well with the previous findings of Didden and Ho, validating the functionality of the current experimental set-up.

Effect of the fence

To begin to fully dissect the volumetric data set obtained of the high speed vortex-wall interaction with the addition of a radial fence, the data must be assembly into an ensemble averaged 3-dimensional matrix. The individual planar data is averaged for

each phase, to allow for the viewing of periodic velocity and fluctuation components. Though this ensemble averaging lessens the magnitudes of the reported vorticity, it is necessary to produce a volumetric data set that can be viewed meaningfully. The instantaneous images vary too much between each forced vortex event at the observed location in the flow to combine them into a meaningful volumetric set. Once formed from the individual planes of data, the ensemble averaged volumetric data set can be viewed in two ways, with 3-D iso-surface plotting or with 2-D cut plane plots. Utilizing the cut planes to describe features initially seen in the iso-surface plots is the most effective method of documenting the secondary vortex wrapping and the effect of the axial fence. Initially, the vorticity in the r , θ , and z directions are plotted and analyzed. The z -component of vorticity allows for an easy depiction of the secondary vortex when it is bent and stretched perpendicular to the ground plane. The r -component of the vorticity is equivalent to the vorticity presented with the two-dimensional data, i.e. rotation inducing velocities in the radial and wall normal directions. The θ -vorticity details both the segments of the primary vortex that lie outside the rz plane due to the areas of vorticity consistent with the secondary vortex being bent perpendicularly to the direction of travel of the primary ring. All three components of vorticity are important to fully understand wrapping of the secondary vortex.

3d- Visualization:

The θ -component of the vorticity provides a view of the majority of the primary vortex ring as it interacts with the ground, as well as the secondary vortex before it is affected by the fence. As shown in Figure 4.34, the primary vortex is radially retarded by

the fence structure. The vortex ring forms a horizontal kink at the center line of the plane (the azimuthal angle of the fence), bending inwards. This kink is the first sign of deviation from the standard expected symmetric ring produced by the axial jet. The secondary vortex, is altered significantly by the introduction of the fence (as to be expected by the previous discussions). Because the secondary vortex is weaker than the primary and closer to the fence, the influence of the fence is anticipated to be much more dramatic on the secondary ring. Figure 4.35 shows the exaggerated kink

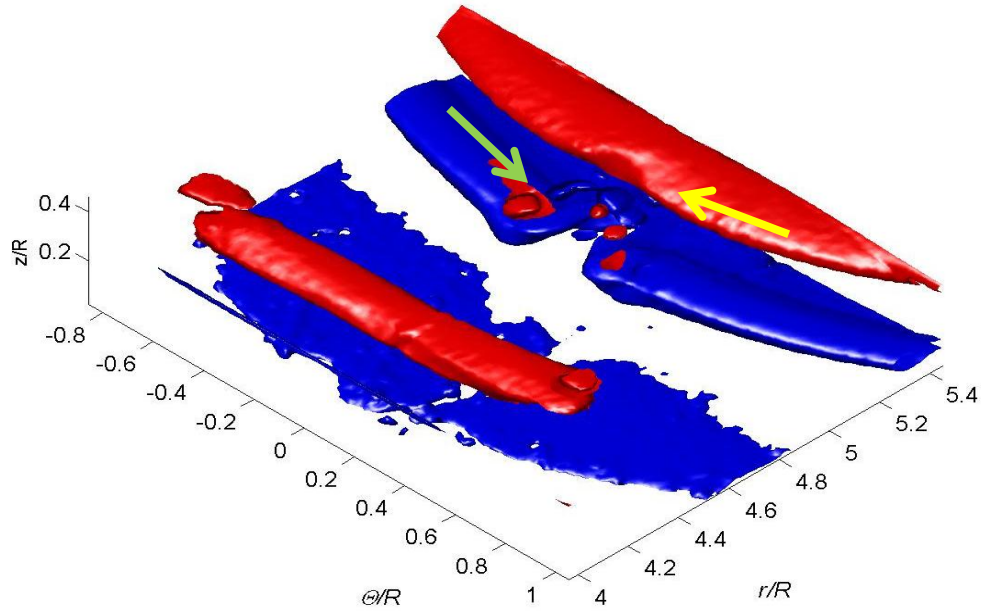


Figure 4.35: The Θ -component of the normalized vorticity at a phase of $t/T=.45$ and contours of $5 \omega_{\theta} R / \bar{V}$. The retardation of the primary vortex is shown by the yellow arrow. The exaggerated kink in the secondary vortex caused by the radial fence is shown (green arrow).

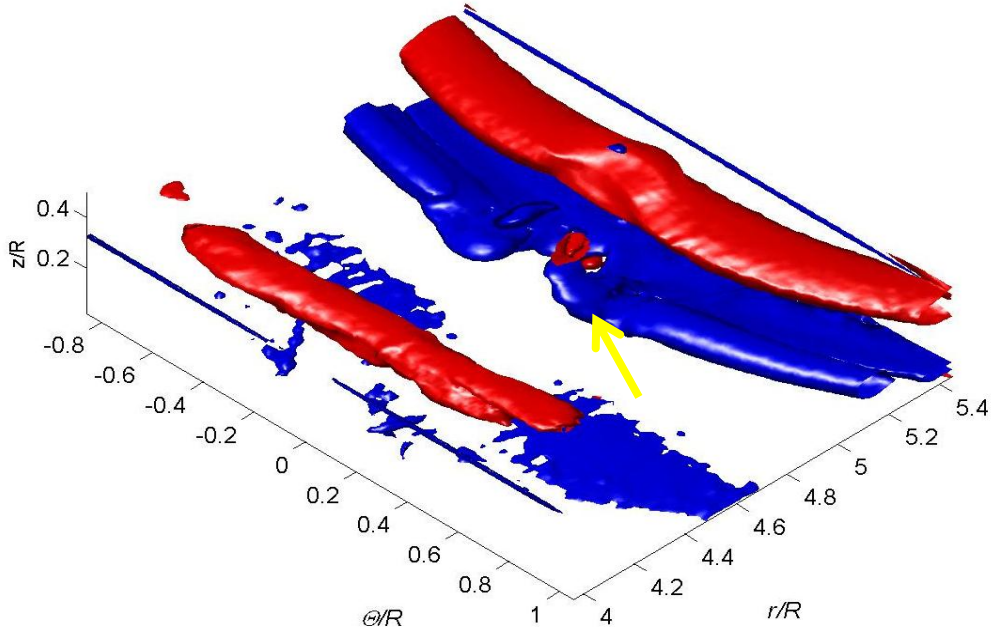


Figure 4.36: The Θ -component of the normalized vorticity at a phase of $t/T=.55$ and contours of $5\omega_{\theta}R/\bar{V}$. The kink caused by the radial fence is shown by the arrow (yellow)

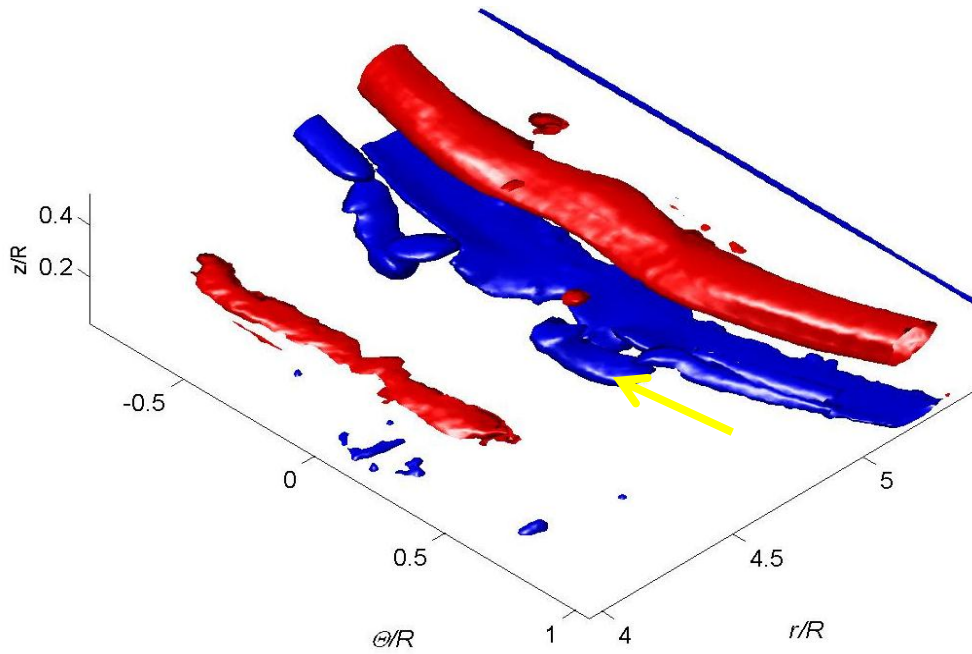


Figure 4.37: The Θ -component of the normalized vorticity at a phase of $t/T=.70$ and contours of $5\omega_{\theta}R/\bar{V}$. The legs under the primary vortex are shown by the arrow (yellow).

formed in the secondary vortex ring immediately after it passes over the radial fence. As the ring continues forward, the kink begins to spread azimuthally outwards as the secondary ring is wrapped around the primary (Figure 4.36). After significant wrapping has occurred, the secondary vortex forms legs beneath the primary, as illustrated in Figure 4.37. These legs concur with the simulations of Luton and Ragab (1997). After the wrapping of the secondary vortex around the primary ring, the primary forced vortex appears smaller in size, but still coherent. The continuation of the primary vortex after the dissipation of the wrapping event was noted by Walker *et al.* (1987) and leads to the continued, although lessened influence of the vortex structure on the flow (i.e., accelerating the boundary layer with a favorable pressure gradient leading to possible relaminarization as described by Yuan and Piomelli 2010).

To further characterize the 3-dimensional wrapping, the z -component of vorticity needs to be examined, as most of the secondary vorticity is “bent” into this direction during the wrapping via the realignment of the vortex ring. The z -vorticity forms a stretched dipole near the fence location (Figure 4.38). This dipole is again representative of the kink formed in the secondary vortex as the instability generated at the fence is grown by the induced flow field of the primary vortex. As the dipole continues to develop, it begins to cause other kinks to form in the secondary vortex azimuthally outward from the fence. These additional kinks are easily depicted in the plots of the z -vorticity, as seen in Figure 4.38. The original secondary vortex disturbance and the additional formed kinks continue to traverse azimuthally outward from the fence location and begin to form legs underneath the vortex (Figure 4.39). The leg structures underneath the vortex may be important in the field of sediment uplift as they induce a

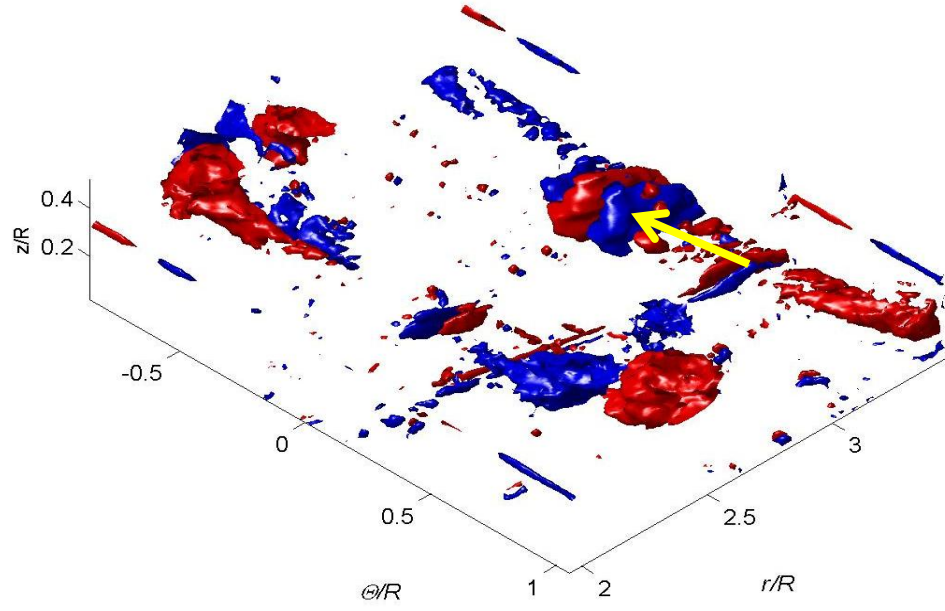


Figure 4.38: The z - component of the normalized vorticity at a phase of $t/T=.35$ and contours of $1 \omega_z R / \bar{V}$. The first kink in the secondary vortex is formed (yellow arrow).

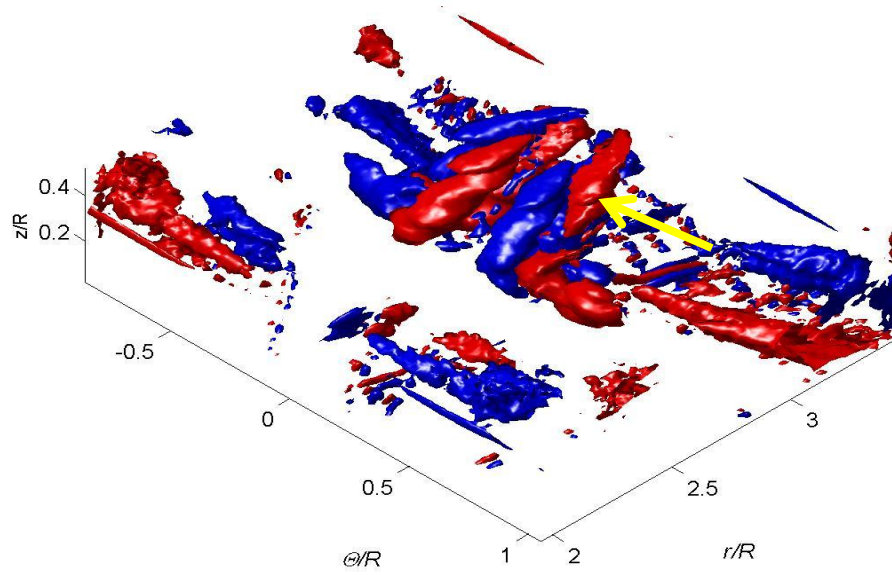


Figure 4.39: The z - component of the normalized vorticity at a phase of $t/T=.60$ and contours of $1 \omega_z R / \bar{V}$. The additional kinks forced upwards by the first vortex kink are visible (yellow arrow).

velocity near the ground plane in the wall-normal direction. Figure 4.40 offers proof of another unexpected flow phenomenon that the second kinks formed by the stretching of the first kink are wrapped under the first kink above the primary vortex. The simulations of Luton and Ragab (1997) show the dipoles of two adjacent vortex kinks wrapping over the primary vortex simultaneously and, therefore, being positioned side-by-side over primary ring. However, in these simulations the kinks are formed at similar times by random disturbance to the flow. In this study, the first kink is formed by the fence, and the secondary kinks are forced upwards by the first kink. This difference leads to the kinks wrapping around the primary vortex at staggered times, causing the first vortex kink to be at a greater height when the secondary wrapping events begin, allowing crossover in the secondary vortex. As the growth of these secondary kinks continue,

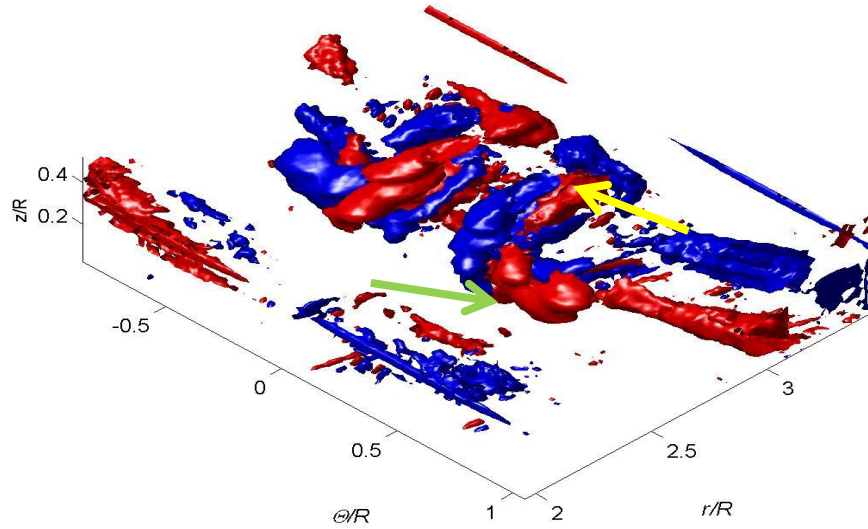


Figure 4.40: The z - component of the normalized vorticity at a phase of $t/T=.70$ and contours of $1 \omega_z R / \bar{V}$. The secondary kinks wrap beneath the loop of the primary kink (yellow arrow). The secondary vortex forms legs under the primary ring (green arrow).

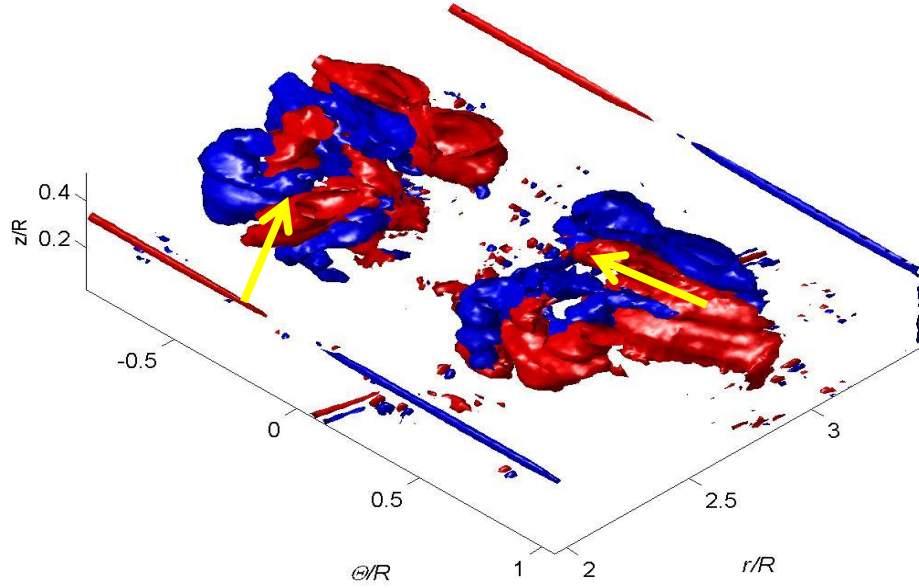


Figure 4.41: The z -component of the normalized vorticity at a phase of $t/T=.90$ and contours of $1 \omega_z R / \bar{V}$. The secondary vortex is bent and curved above the primary vortex (yellow arrows).

the loops spread further outwards (Figure 4.41), similar to the final loop positions seen demonstrated by Luton and Ragab (1997).

The enstrophy allows for a complete viewing of all components of the vorticity in a single figure. Though plots of the enstrophy neglect the sign of the displayed vorticity, it provides a view of the general shape of the vortex events. The enstrophy confirms the previously discussed characteristics of the wrapping event. Figure 4.42 shows the initial development of the disturbance of the secondary vortex caused by the fence; the primary vortex is mainly undisturbed, while the secondary vortex displays an initial kink. As the vortex progresses and the kink is stretched, the secondary vortex wraps around the primary, as seen in Figure 4.43. The secondary vortex forms a loop over the primary and is spread outward with the introduction of the secondary kinks (Figure 4.44)

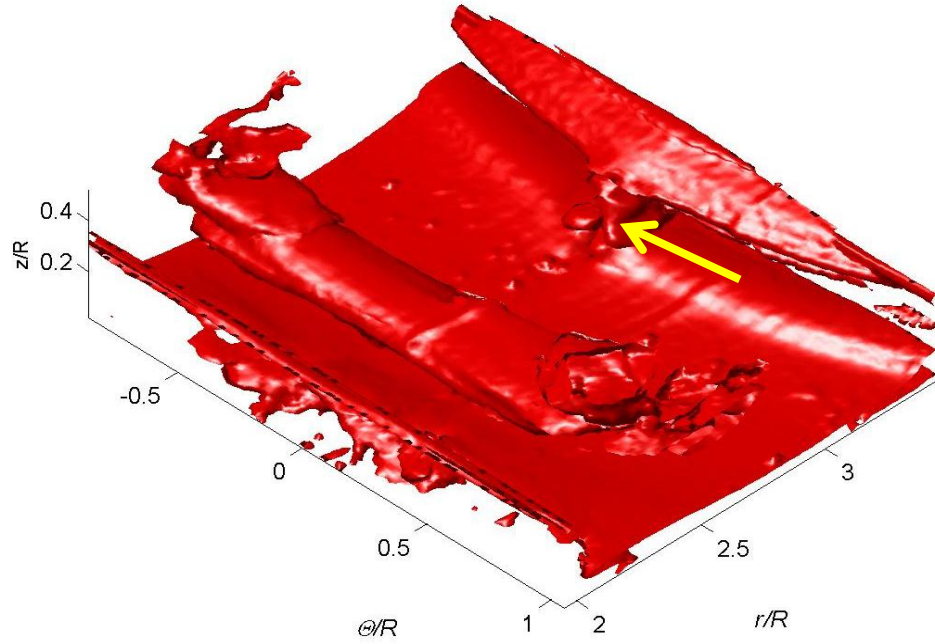


Figure 4.42: The normalized enstrophy at a phase of $t/T=.35$ and contours of $2.5 \omega R/\bar{V}$. The initial kink in the secondary vortex is seen (yellow arrow).

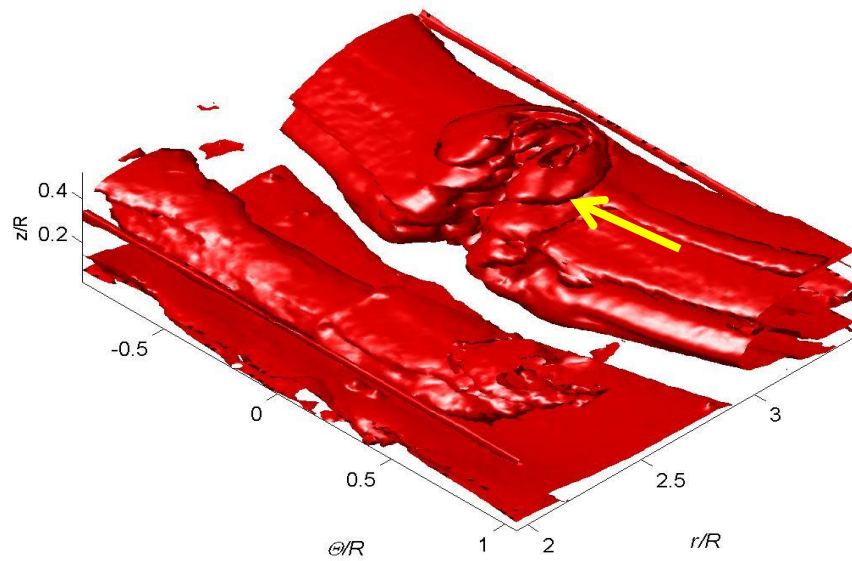


Figure 4.43: The normalized enstrophy at a phase of $t/T=.60$ and contours of $2.5 \omega R/\bar{V}$. The secondary vortex completely wraps around the primary vortex forming a loop (yellow arrow).

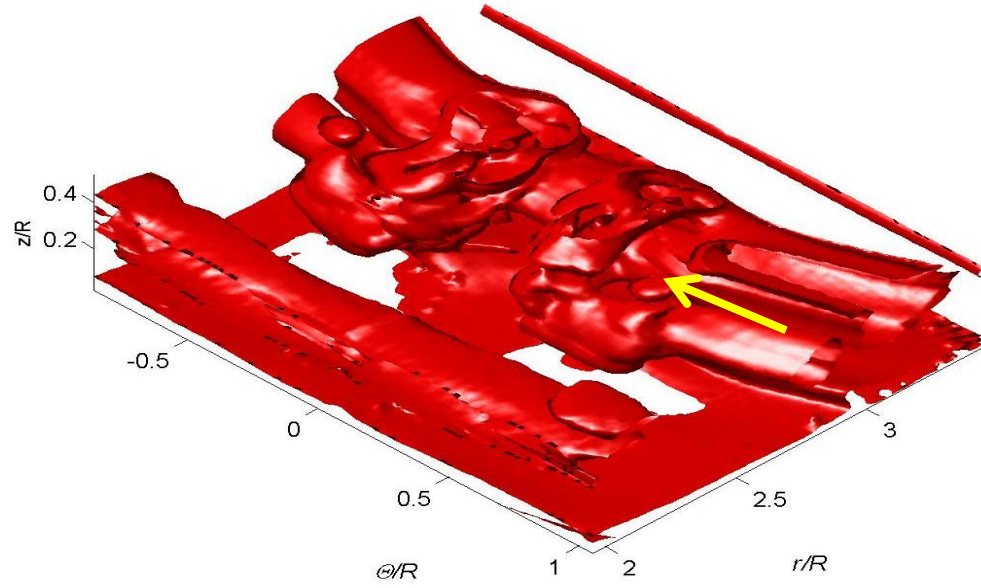


Figure 4.44: The normalized enstrophy at a phase of $t/T=.75$ and contours of $2.5 \omega R/\bar{V}$. The loop above the primary vortex is bent and stretched outward (yellow arrow).

Cut-plane Analysis:

To describe the features shown in the 3-dimensional renderings of the vorticity, specific cut-planes in the r , θ , and z directions must be viewed. These cut-planes create a more simplistic view of the wrapping phenomenon and provide a more detailed insight into the predicted wrapping events.

Z- vorticity

At the lowest planes of the data set ($0 < z/R < .06$), the vorticity is dominated by turbulent flow instabilities and noise in the images (i.e., reflections of the laser sheet on the ground plane and illumination of stagnant dust particles on the ground plane, Figure 4.45). The z -vorticity is never a significant contributor in this region. Initially, the majority of the vorticity in this location is in the axial direction, similar to the vorticity

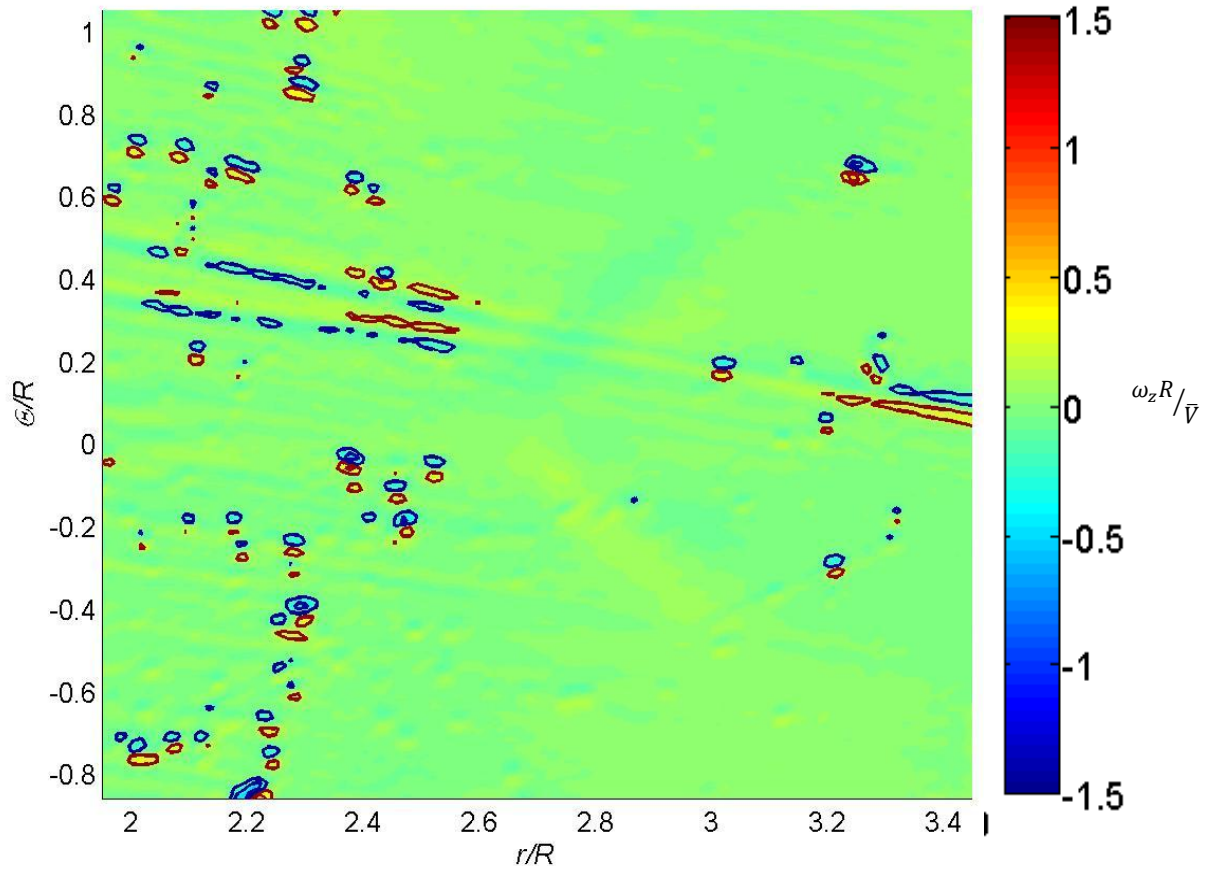


Figure 4.45: The z -component of the normalized vorticity near the ground plane. The vorticity is dominated by reflections as this height

seen in the 2-dimensional data sets. As time progresses and the secondary vortex ring is bent, the majority of the vorticity exists in the r and z direction, as the secondary vortex forms legs under the primary.

In the mid-range of the data set, ($.08 < z/R < .28$), the z -component vorticity begins to develop stronger structures in the flow-field (Figure 4.46). These structures are a direct result of the wrapping of the secondary vortex around the primary. At the first instance these structures are notable with the given vorticity contours of $20 \text{ m}^2\text{s}^{-2}$ ($t/T=0.3$), a vorticity dipole is seen radially outward of the location of the primary vortex. This dipole is representative of a spike in the secondary vortex brought on by the tripping

of the boundary layer. Once the spike is high enough, its vertical momentum forces the beginning of secondary spikes azimuthally outwards of the primary spike formed by the fence. These new boundary layer spikes begin forming dipoles similar to the primary kink, but less coherent in the ensemble averaged data. The secondary vortex ring moves above the field of view of the lower planes, as the rebound forces it vertically upwards.

A distinct feature of the wrapping event is discovered in these cut-planes. In the low-speed data set, a tertiary vortex is seen developing radially inward of the secondary vortex spike. Previous literature has reported the formation of a tertiary vortex forming under the primary vortex after the completion of the first rebound event, with the same direction of rotation as the secondary ring. This tertiary ring was reported to grow in strength as the Reynolds number of the primary ring increases; the added turbulence adds to the magnitude of the vortex-ground interaction. However, in the high-speed data, the tertiary vortex is not seen in the ensemble averages, suggesting that the tertiary vortex seen in the low-speed data set is not caused by the same phenomenon. Instead, the tertiary structures appear as secondary separation events occurring at the boundary layer under the primary vortex. The tertiary ring is an additional separation of the boundary layer that fails to separate with the generation of the secondary vortex. The tertiary ring follows the secondary ring wrapping pattern, and appears azimuthally inside of the initial disturbance of the secondary ring. The tertiary ring appears smaller in magnitude than the secondary ring, and is seen developing later in the flow. Several factors may influence the appearance of the tertiary ring in the low-speed data set and not in high speed data. The first of these reasons could be the location of the fence forcing the

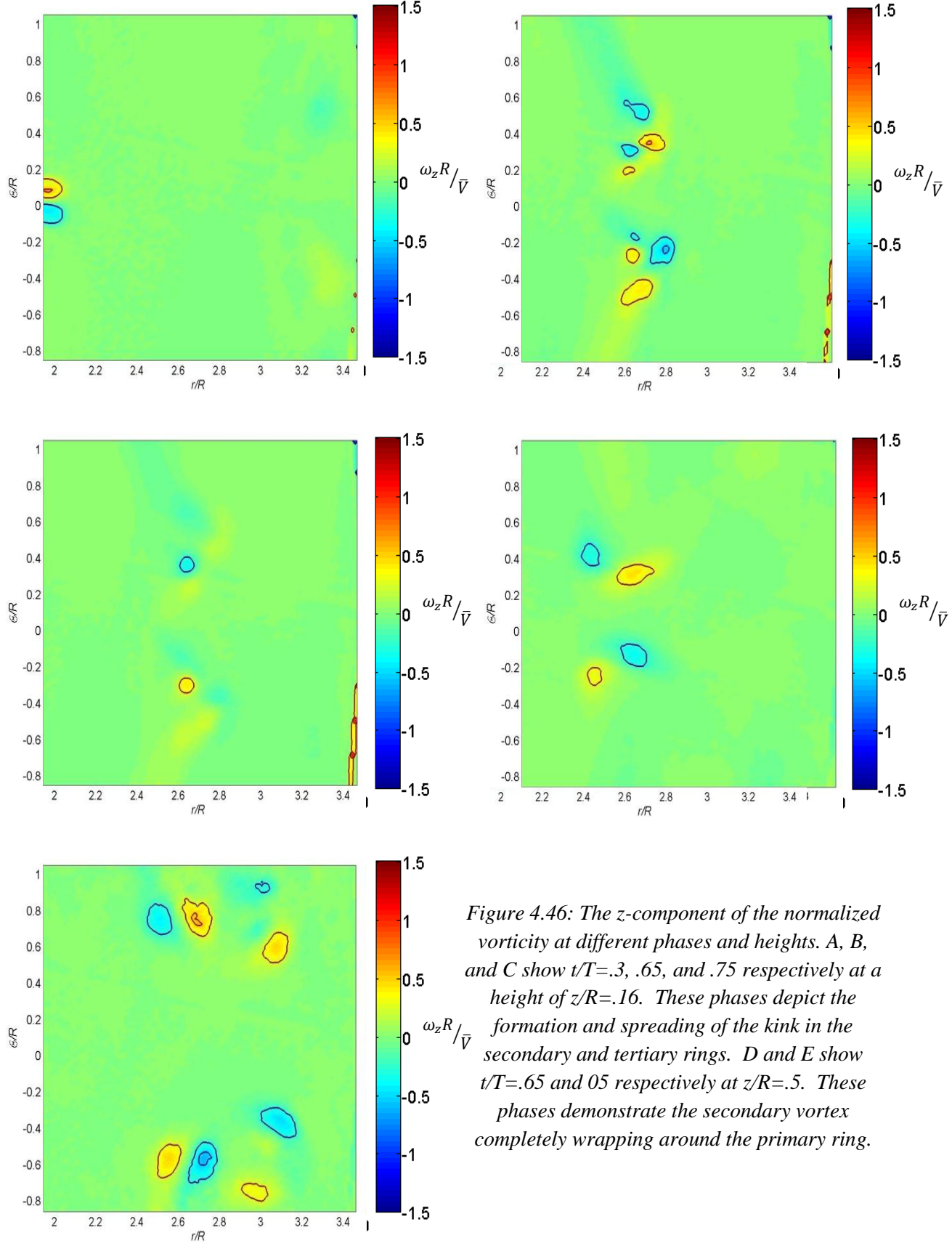


Figure 4.46: The z -component of the normalized vorticity at different phases and heights. A, B, and C show $t/T = .3, .65$, and $.75$ respectively at a height of $z/R = .16$. These phases depict the formation and spreading of the kink in the secondary and tertiary rings. D and E show $t/T = .65$ and $.05$ respectively at $z/R = .5$. These phases demonstrate the secondary vortex completely wrapping around the primary ring.

wrapping event with respect to the trajectory of the primary vortex. Further tests must be done to determine the effect of a normalized fence distance on the wrapping event. The second factor leading to the introduction of the low-speed tertiary vortex is the increased thickness of the boundary layer for lower speed flows. In lower Reynolds number flows, it is expected to have a more dispersed boundary layer under the primary ring. Again, further studies of the effect of fence size on the tertiary ring may determine the factors leading to this discrepancy between the high and low-speed data sets.

The highest planes of data ($.3 < z/R < .5$) provide insight in to the wrapping of the secondary vortex ring above the primary. This complete wrapping is illustrated in the vorticity plots by the emergence of z-component vortices radially inward of the primary vortex ring. These vortices represent the boundary layer spikes in the secondary vortex being stretched up and entirely over the primary ring. The displayed vorticity is a cross-section of the secondary ring as it travels down the posterior side of the primary ring. As the data planes move higher in the z direction, it becomes easier to track the complete wrapping events from earlier phase angles. By viewing the vorticity at the highest plane ($z/R=0.5$) the wrapping can be fully detailed. As seen in Figure 4.46, the secondary vortex spike is initially visible strictly radially outward of the primary vortex ($t/T=0.65$) but soon is wrapped entirely over the primary ring ($t/T=0.05$). The loop of counter-rotating vorticity wrapped behind the primary vortex spans a larger angle than the initial spike, a general shape documented by Luton and Ragab (1997). As time progresses, the secondary spikes forced by the upwards momentum of the initial kink in the secondary vortex begin to also wrap around the primary ring ($t/T=.05$). These spikes of vorticity are of the opposite sign rotation as the original kink, and thus form dipoles with the already

existing vortex loop. Unlike the dipoles formed radially outward of the vortex which are aligned azimuthally, the dipoles formed behind the primary vortex are side-by-side in the radial direction and rotate outwards as time progresses. This pattern suggests that the initial spike is wrapped “loosely” around the primary ring, allowing the secondary spikes to partially pass under the initial spike of the secondary vortex. This observation is also supported by the radial distance between the outward and inward appearances of the vertical vorticity. At the phase where the secondary wrapping event is first noticed ($t/T=0.05$ at $z/R=0.5$), the vortices of the primary wrapping event are separated by a distance of approximate $0.5R$, while the secondary wrapping events vortices are $0.25R$ apart. The proximity of the vortex tube location behind and in front of the nozzle for these spikes suggests that the secondary spike is wrapped tighter around the primary vortex at this phase angle.

Because of the steady decrease in strength of the primary vortex, the difference in wrapping height of the primary and secondary spikes in the secondary vortex can be explained by the smaller vertical velocities associated with the primary vortex during the wrapping of the secondary spike. Also, the longer the spike is subjected to the induced velocities of the primary vortex ring, the more drastic the stretching and wrapping events are. Though the primary kink is initially wrapped tightly around the primary, it is constantly pushed upwards and away from the primary ring by the strong up-wash velocity radially outward of the primary ring. The tertiary vortex does not produce a noticeable, complete wrapping in the ensemble averaged data. This lack of wrapping may stem from the tertiary vortex forming further into the rebound event, so interacting with the primary ring from a greater vertical separation than the secondary ring.

Looking at cut-planes of the z -vorticity in the θ - z plane, the vertical stretching of the secondary and tertiary vortex becomes clearer. As seen in Figure 4.49, which depicts the vortex interaction at a phase of $t/T=0.6$, the secondary vortex is drawn upwards around the primary vortex ring, as expected. At a radial distance of $r/R=2.15$, there exists two additional vertical streaks of z -vorticity that are of the opposite sign as those representing the wrapping of the secondary vortex. These streaks coordinate with the secondary ring being wrapped into legs under the primary vortex, forming a “loop” radially outward of the vortex, as illustrated in Figure 4.49. Observing radially inward of the vortex ring (at position 2.14), two vertical streaks of z -vorticity are shown, representing the vertical component of the secondary vortex looping around the primary. The secondary ring forms a loop behind the primary vortex, as seen in Luton and Ragab’s

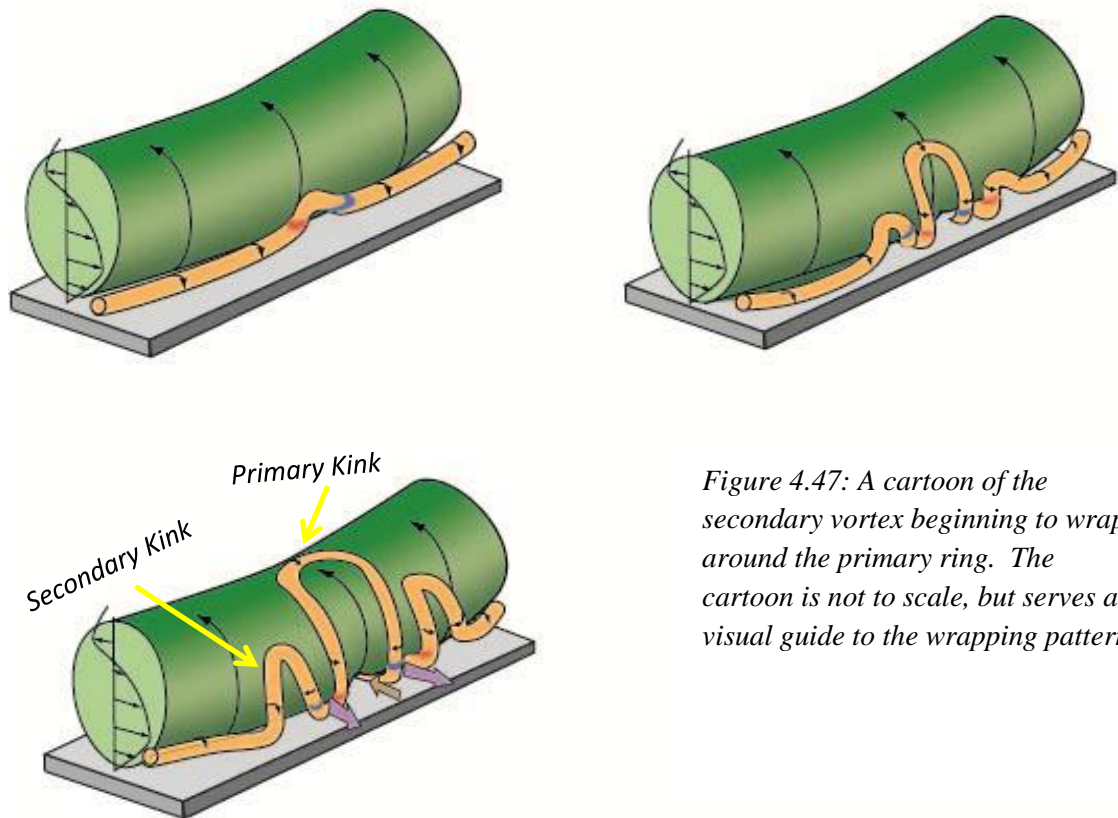


Figure 4.47: A cartoon of the secondary vortex beginning to wrap around the primary ring. The cartoon is not to scale, but serves as a visual guide to the wrapping patterns.

simulations. Between the primary and secondary vortex ring, two smaller streaks extending up over the primary ring are visible. The streaks are similar to the aforementioned events of vorticity corresponding to the wrapping of the secondary vortex, but are of a smaller magnitude. The streaks are indicative of the tertiary vortex beginning to wrap around the primary vortex ring, like its secondary counterpart. This tertiary vortex never fully wraps around the primary vortex ring before being dissipated by the primary ring and becoming dominated by jitter.

r - vorticity

The r -component of vorticity illustrates the areas of the flow domain where the vortex tubes lie in the radial direction. As the rings are formed perpendicular to this direction, this component is the least prevalent in the flow. Analyzing the r -component of vorticity in r - z planes reveals information about the kink formed under the primary vortex. As seen in Figure 4.48, four lobes of r -vorticity are seen at phase $t/T=0.6$ and radial location $r/R=2.14, 2.42$, and 2.61 . These lobes are of alternating sign, suggesting they are formed from a single vortex tube alternating directions of travel, as seen in the predicted loop below the primary vortex. Further description of the kink in the secondary vortex appears via the comparison of the z and r -component vorticity in the same area of the flow (Figure 4.48 and 4.49), showing that the z -vorticity connects the lobes of the r -vorticity. The noteworthy aspect of the kink exposed by the r -vorticity is the fact that the bend in the secondary vortex under the primary vortex remains in the r - z plane, and does not traverse azimuthally. The four lobe vorticity pattern is also seen radially inward of the primary vortex (at position $r/R=2.61$), existing as a signature of the secondary vortex forming a loop around the primary. Employing a side-by-side comparison of the z and r -

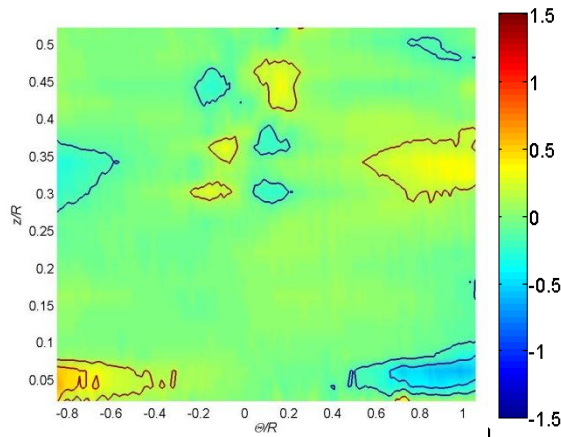
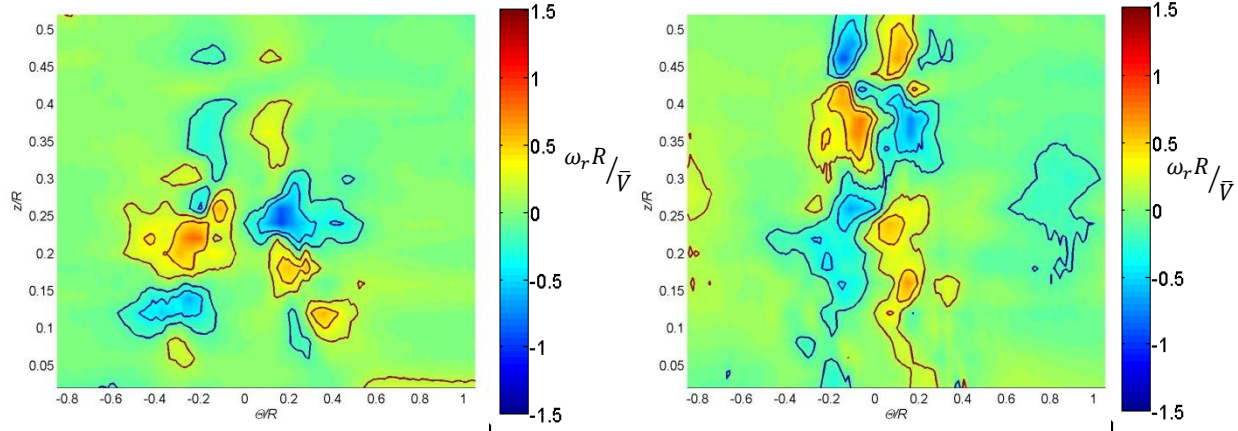


Figure 4.48: The r -component of the normalized vorticity at $r/R=2.15$, 2.42 , and 2.61 respectively at $t/T=.6$. The figures show different instances of vorticity around the legs beneath and loops over the primary vortex ring.

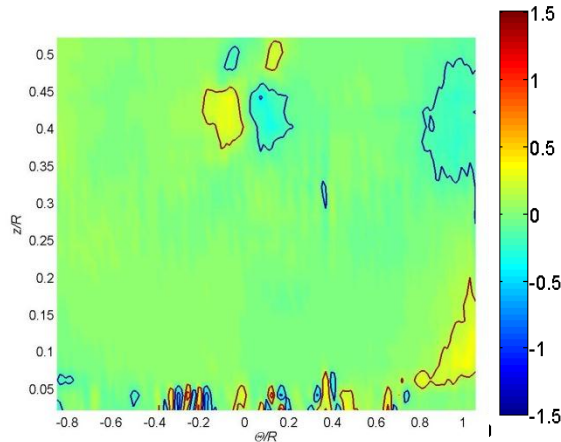
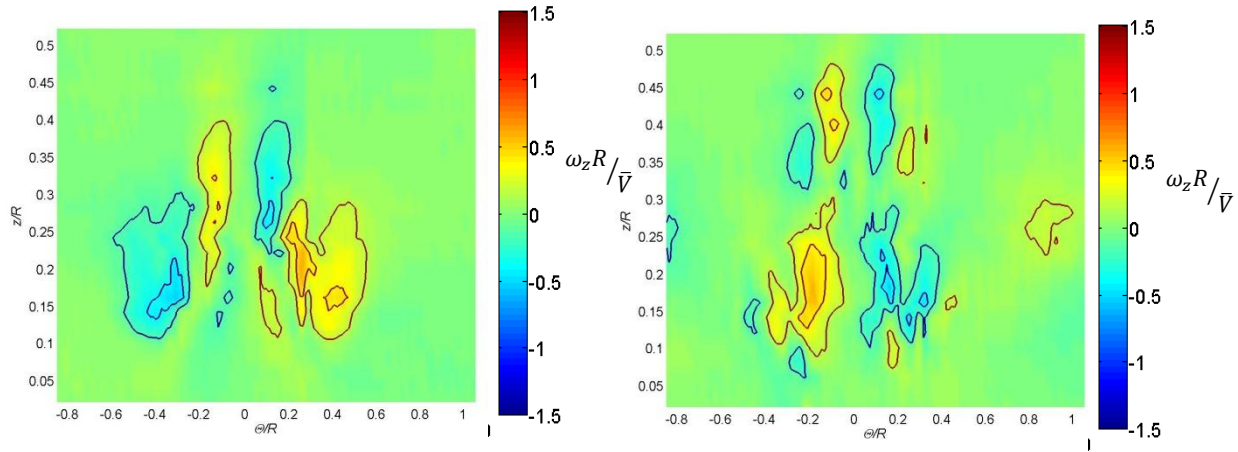


Figure 4.49: The z -component of the normalized vorticity at $r/R=2.15$, 2.42 , and 2.61 respectively at $t/T=.6$. The figures show different instances of vorticity around the legs beneath and loops over the primary vortex ring.

vorticity components for the same plane shows the z -vorticity tubes connecting the r -vorticity lobes. The complete looping of the secondary vortex above the primary ring is visualized by this component of the vorticity.

θ -vorticity

The θ -component of the vorticity in the 3-dimensional data corresponds to the displayed vorticity in the 2-dimensional imaging previously discussed. The majority of the vorticity for the primary vortex, as well as the initial stages of the secondary vortex

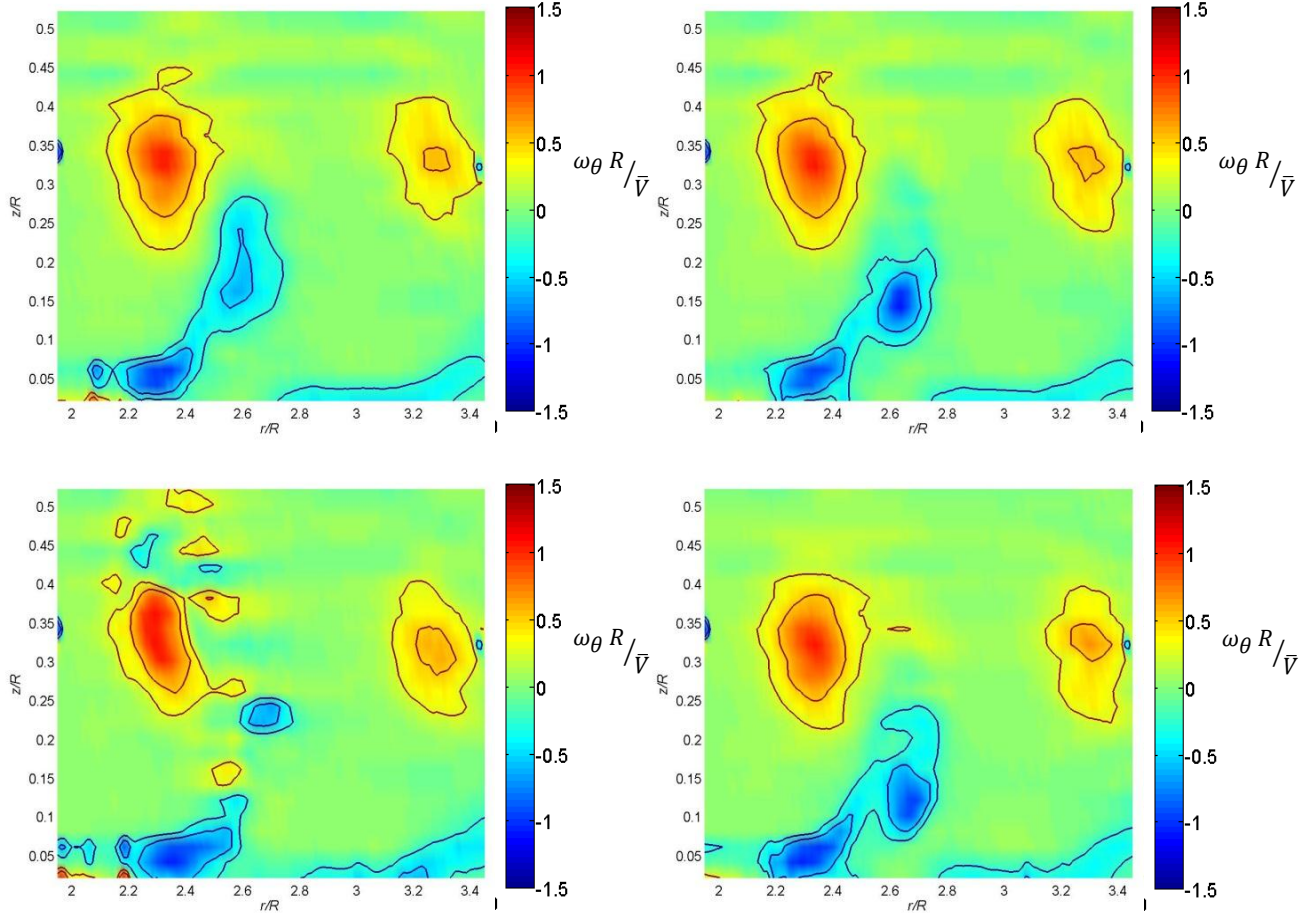


Figure 4.50: The θ -component of the normalized vorticity at $\Theta/R=-1.41$, -1.30 , -1.05 , and $-.50$ respectively at $t/T=.65$. The figures show the wrapping pattern of the secondary vortex around the primary.

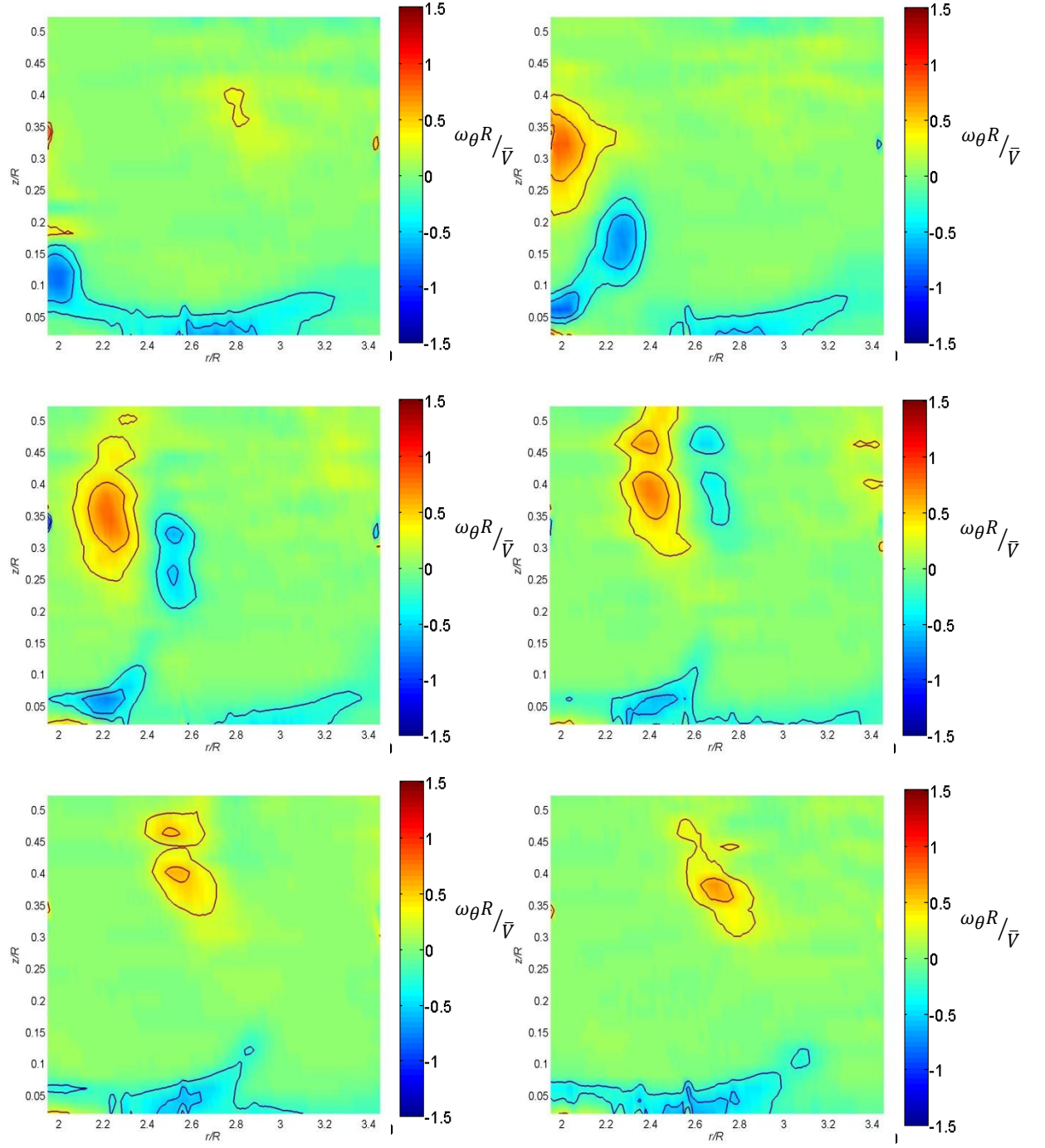


Figure 4.51: The Θ -component of the normalized vorticity at $y/R = -0.9$ and $t/T = 0.4, 0.55, 0.60, 0.75, 0.9$, and 1.05 respectively. The figures show comparable vortices to those seen in the 2-Dimensional data; i.e. a secondary vortex formation and vortex rebound.

exists as θ -vorticity, because of the initial alignment of the vortex ring. Viewing the θ -primary ring interacts with the ground and forms the secondary ring. Figure 4.51 shows a strong similarity to the previously discussed 2-dimensional data, suggesting that the stereo camera calibration and data processing methods provide an accurate depiction of the flow mechanisms surrounding the vortex ring. Dissecting a single phase of the θ -vorticity over different r - z planes shows the shape of the secondary vortex ring during the growth of the initial disturbance. Figure 4.51 displays the r -vorticity over azimuthally different cross-sections. In this figure, the secondary vortex is shown to first bend slightly upwards around the primary ring before traversing back down under the primary vortex. After the secondary ring reaches its lowest point, it begins to ascend for the primary disturbance. This instability is pulled much higher on the primary vortex than the initial upwards disturbance of the ring before beginning to descend back down the primary ring. The secondary ring then repeats this pattern, in the reverse order, suggesting that the effect of the radial fence is symmetric about the axis of the fence. A cartoon of the shape of the secondary vortex ring at this phase is approximately depicted in Figure 4.47.

Other knowledge gained from exploring the θ -component of the vorticity at different phases includes the validation of the tertiary vortex. Figure 4.50 shows the formation of the tertiary vortex. In this figure, the trailing vorticity left behind the secondary ring is shown to roll up into a tertiary coherent vortex, confirming the idea that this vortex is responsible for trailing structures of vorticity that are the same sign as the secondary ring.

Instantaneous Imaging

Ensemble averaging techniques can mask flow features seen in the instantaneous images obtained from PIV. Flow structures that vary in location from image to image are often washed out during ensemble averaging. Also, the intensity of reported structures is lessened by vortex jitter. To observe the effects of ensemble averaging and verify the conclusions obtained from it, it is important to also take into consideration instantaneous images of the flow field. The instantaneous images, however, can only be viewed in the r - θ planes that they were obtained in. There exists too much variation between the instantaneous images to form a volumetric data set that would be beneficial in determining flow structures.

Several key flow structures are observed in the instantaneous images. The first of these is the formation of the tertiary vortex. Figure 4.52 shows the secondary and tertiary vortex ring wrapping around the primary vortex. In the ensemble images of the tertiary vortex, it seemed to be of a significantly smaller magnitude than the primary. However, the instantaneous images show that the tertiary vortex is, in fact, initially equal in magnitude to the secondary ring. Also, the instantaneous image depicts the true shape of the tertiary vortex hidden by ensemble averaging. The tertiary vortex is significantly elongated compared to the secondary ring. This elongation stems from the boundary layer remaining stretched and uplifted into the flow after the secondary ring is formed (as seen in Figure 4.52a), leading to a much less organized tertiary ring. These stretched areas of the tertiary vortex continue in the flow at later phases (Figure 4.52b). Also, the tertiary vortex is seen to form dipoles as it moves radially forward in the flow. As the image plane height increases, the strength of the tertiary vortex in the z -direction is

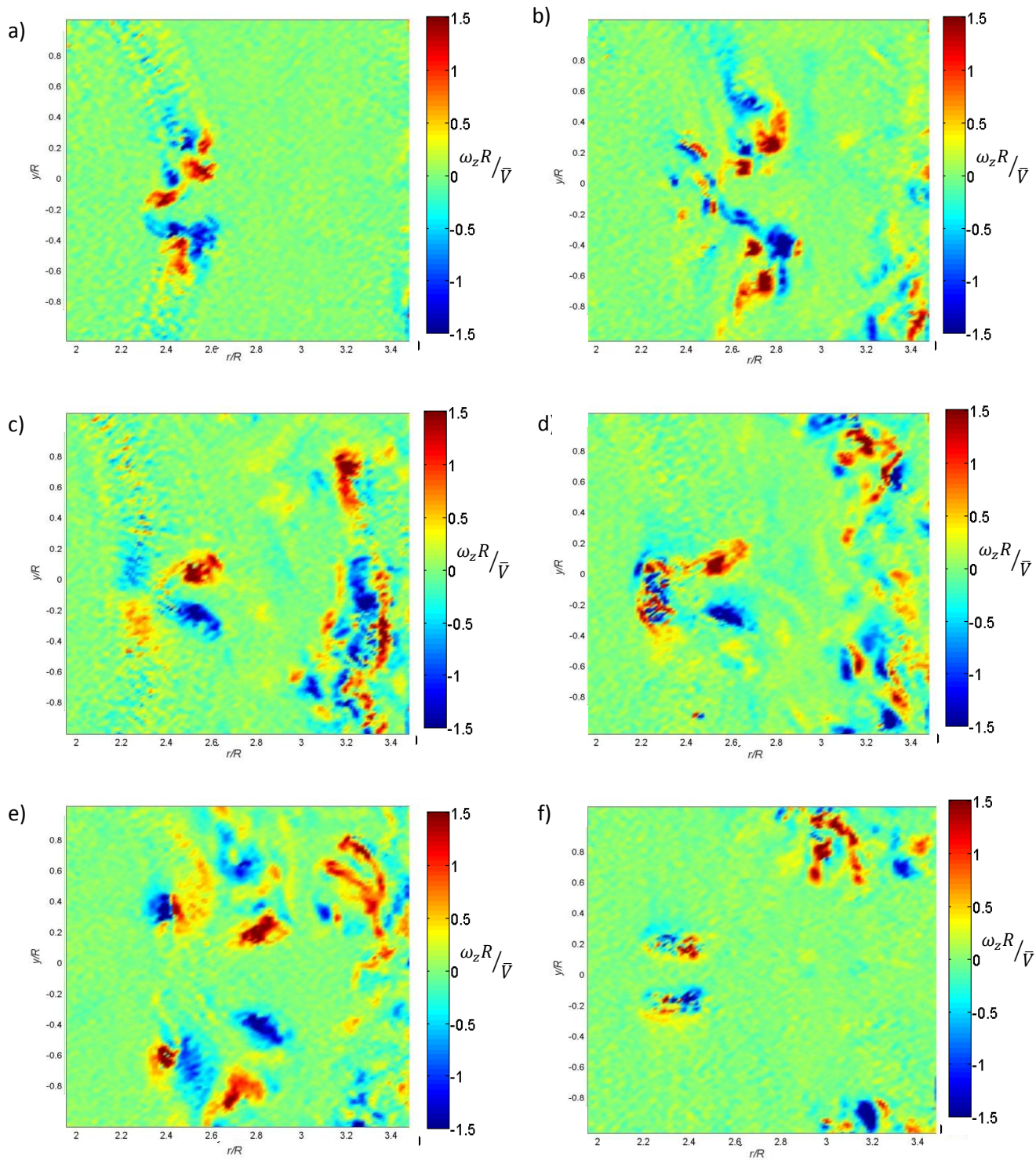


Figure 4.52: Instantaneous plots of vorticity for heights and phases; a) $z/R=.14$ $t/T=.55$ b) $z/R=.2$ $t/T=.70$ c) $z/R=.32$ $t/T=.60$ d) $z/R=.58$ $t/T=.65$ e) $z/R=.58$ $t/T=.80$ f) $z/R=.5$ $t/T=.65$

significantly weaker than that of the secondary vortex (Figure 4.52b). The loop around the primary vortex can be seen to cause an area of scattered vorticity behind the primary ring, signifying a stretched and dissipated secondary vortex that lies mainly in the $r-\theta$ plane (Figure 4.52c). At even higher planes, the initial rollup of the secondary vortex is seen to completely wrap around the primary, as shown by a streak of the aforementioned scattered vorticity connecting the fence-induced dipole radially outward of the primary vortex to the loop trailing it (Figure 4.52d). As this loop progress in time and the primary vortex rebounds higher into the flow, the streaks of scattered vorticity organize (Figure 4.52e), and eventually become coherent areas of vorticity (Figure 4.52f), suggesting that the secondary vortex now crosses the imaging plane perpendicularly.

Quantitative effect of the fence:

The dramatic influence of the fence can be seen in the time-averaged radial velocity field (Figure 4.53). For the case with no fence, the flow is nominally axisymmetric, albeit with notable azimuthal variation for $r/R > 3$ due to possible low-frequency variation in the outer flow and the relatively small number of samples. For the case with the fence, the radial velocity exhibits a sharp bifurcation downstream of the primary vortex impingement location ($r/R = 2$), leading to two high-speed streaks (marked BB in the figure) straddling on either side of a low-speed valley (line AA). The included angle between the two streaks is approximately 35° . Beyond $r/R \approx 3.4$ the mean radial velocity field appears quite similar to the case with no fence.

The cause of these streaks becomes apparent when examining the ensemble-averaged velocity fields and the various moments of the periodic and stochastic

fluctuations (Figure 4.54). Examining first the ensemble-averaged wall-normal velocity, \tilde{v}_z , it can be seen that the fence perturbs the secondary vortex to form a kink that bumps up into the higher speed primary vortex ($t-t_0 = 2.8$ ms), as noted in previous literature on impacting vortex rings. This vorticity forms a dipole with an induced velocity that opposes the mean flow, and hence forms the low speed region noted in Figure 4.54. The strength of the vorticity is significant, with peak values approaching 50% of the primary

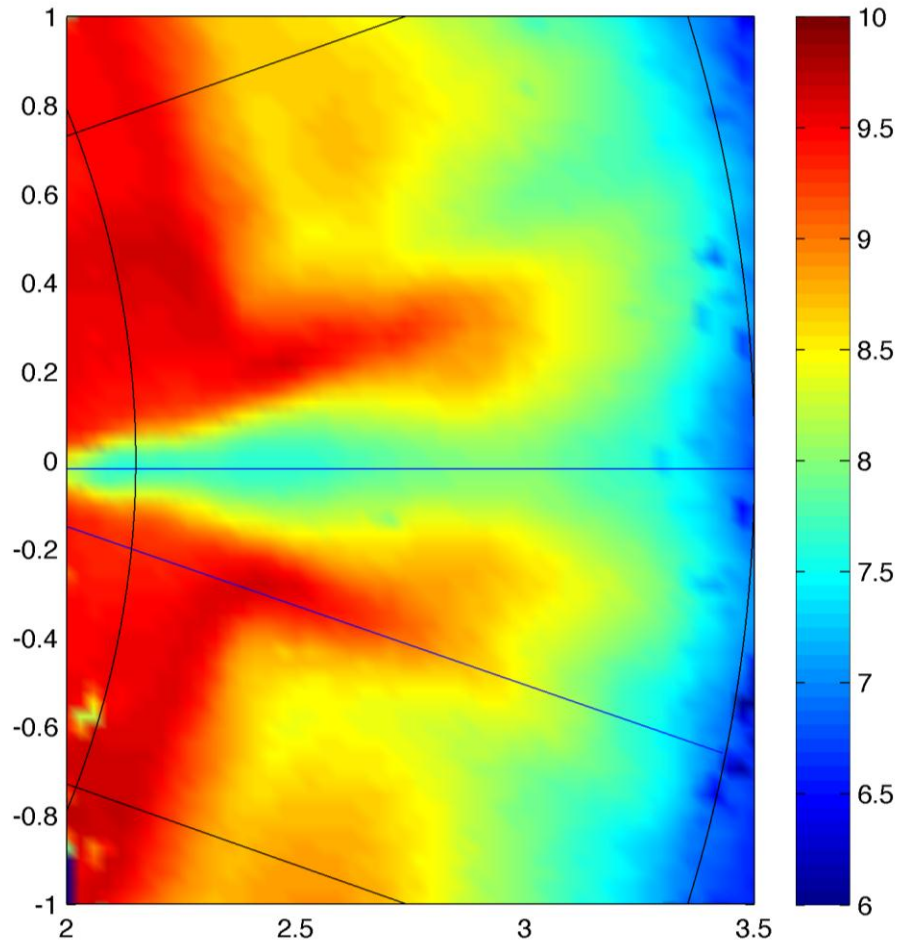


Figure 4.53: Time-averaged radial velocity, \bar{v}_r for a plane $z/R = 0.02$. The case with no radial fence is shown on the left, and the case with a radial fence is shown on the right (location indicated by grey stripe). The region used to calculate the azimuthal averages is shown by the black sector, and to sectional lines, AA and BB are indicated.

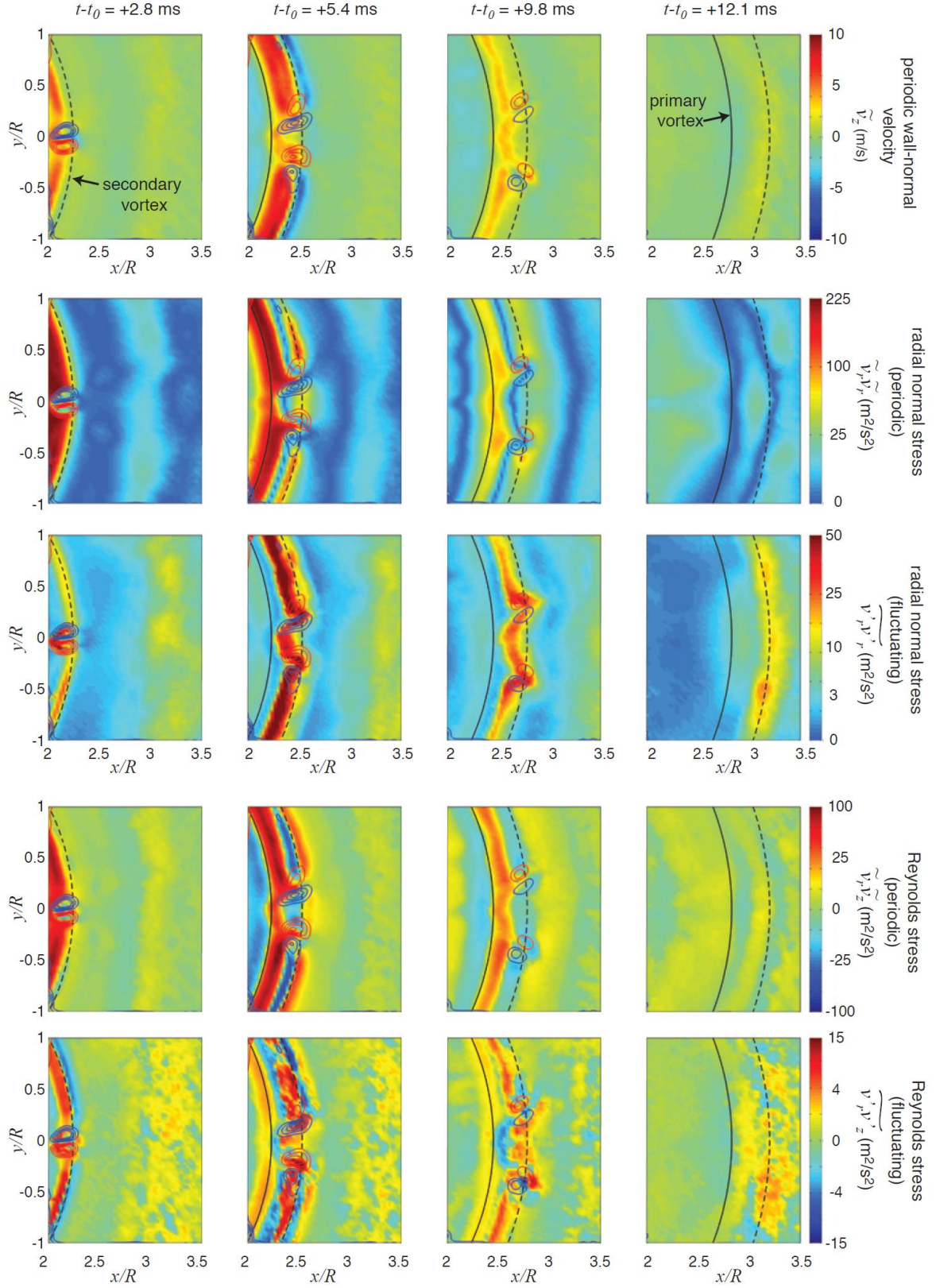


Figure 4.54: Ensemble-averages of the wall-normal velocity and periodic and stochastic Reynolds stresses in a plane parallel to the wall at $z/R = 0.02$. Note that the color scale for the stress components is stretched quadratically to capture the large variation. The location of the primary (solid line) and secondary (dashed line) vortex core is indicated by the corresponding black line. Contours of the wall-normal vorticity component (ω_z) are shown at several positive (red) and negative (blue) thresholds (1000 to 4000 1/s in 1000 1/s increments).

vortex. Note also that the vorticity contours shown in Figure 4.55 indicate only the wall-normal vorticity magnitude and, therefore, represents a fraction of the three-dimensional magnitude (unless the vortex is oriented perpendicular to the page, which is not known from the current data).

By $t - t_0 = 5.4$ ms, the original pair of vortices have spawned new opposite-signed partners and are beginning to move away from the radial plane where they originated. This observation is consistent with additional kinks developing in the secondary vortex and being pulled down into the lower speed region beneath primary vortex. Similar shear-instability-driven vortex dynamics have been noted in other systems, such as in free-shear mixing layers (Choi & Lasheras, 1989), where smaller vortices are reoriented and intensified as they are pulled in a straining field between larger neighbors. Also visible at this instance, is the strong upwelling between the primary and secondary vortex cores, flanked on either edge by significant but slightly weaker downwash on the opposite sides of the respective vortex cores.

As the primary vortex moves past $r/R = 2.4$ ($t - t_0 = 9.8$ ms), the strength of the upwash starts to dramatically decrease and the dipole pairs of the secondary vortex continue to separate further from their plane of origin. Finally, by $t - t_0 = 23.8$ ms, the vortex signature has decreased to less than 20% of its original value, and has lost nearly all azimuthal variation visible in the prior three instances shown.

The remainder of Figure 4.54 follows the evolution of the Reynolds normal ($\tilde{v}_r \tilde{v}_r$ and $\bar{v}_r \bar{v}_r$) and shear ($\tilde{v}_r \tilde{v}_z$ and $\bar{v}_r \bar{v}_z$) stress contributions. As to be expected in a highly organized coherent structure, the periodic fluctuation stresses dominate their stochastic

counterparts by a magnitude of 5 to 10 times in the early stages of development. Once the primary vortex begins to lose coherence ($t-t_0 = 9.8$ ms), however, the stresses become more comparable in magnitude, with the stochastic contributions becoming dominant by the time the remnants of the vortex pass $r/R > 3$. This is consistent with a rapid decrease in the observed strength of the primary and secondary vortex, which can be diminished by both random “jitter” in the vortex location as well as increased dissipation due to the violent breakdown that is initiated by the three-dimensionalization of the primary and secondary vortex. A full accounting of the turbulent kinetic energy budget is needed to ascertain the relative contributions to this trend, which is beyond the scope of the current limited data set. From Figure 4.54 it is also evident that the radial normal stresses are dominant over their shear stresses throughout the region by a factor of 2 to 3.

Finally, in regard to the stress magnitudes along the valley and streak regions (section AA and BB, respectively), Figure 4.55 indicates that the periodic component of both the normal and shear stresses should see higher magnitudes in the high-speed streak region (section BB) in comparison to the valley (section AA) because of the similarly

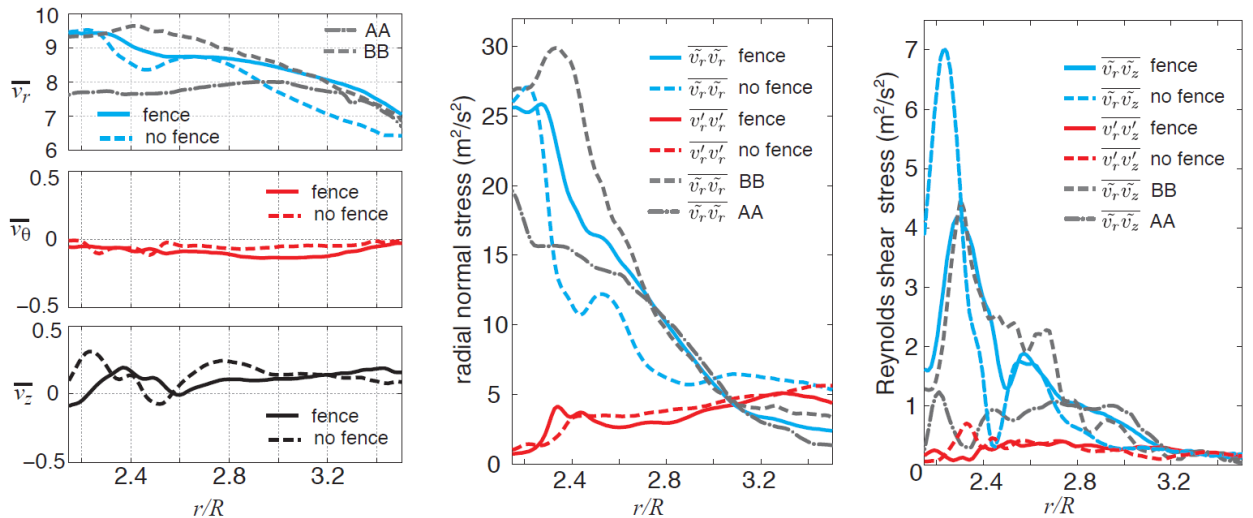


Figure 4.55: Azimuthal- and time-averaged radial profiles. Mean velocity profiles (left), radial normal stresses (center) and wall-normal Reynolds stresses (right). Grey lines indicate the sectional profiles in the low-speed (AA) wake, and the high-speed (BB) streak noted in the mean radial velocity shown in Figure 4.53

elongated streaks of elevated stress in this region. The stochastic stress, on the other hand, maintains a comparable radial width across all of the azimuthal locations, keeping comparable contributions to the net stress when comparing the valley and the high-speed streak regions.

The above measurements can then be further distilled to their contributions to the time-averaged equations (Figure 4.55) which present time-averaged sections of fence conditions, as well as time- and azimuthally-averaged data for both cases. The trends are muted relative to the ensemble-averaged results above, but maintain similar behavior. Specifically, the coherent stresses in the high-speed region (BB) are approximately 2 to 4 times what is observed in the valley (AA) over the range from $2.2 < r/R < 2.7$, after which they collapse to the azimuthal average values. For the normal stress, $\tilde{v}_r \tilde{v}_r$, the increase and decrease are roughly equal relative to the azimuthal average, while for the shear stress $\tilde{v}_r \tilde{v}_z$, the high-speed streak region remains similar to the azimuthal average, with the valley experiencing a significant decrease.

In comparing the fence, and no-fence conditions, the stochastic contributions to the stress are similar to each other, and the only significant differences result from variations in the periodic stresses (Figure 4.55). Examining the periodic stresses in more detail, the azimuthally-averaged periodic normal stress ($\tilde{v}_r \tilde{v}_r$) is elevated by roughly 50% within the region from $2.3 < r/R < 3.0$. This is a significant enough of an increase that even the reduced values in low-speed region (section AA) exceed the typical no-fence case magnitudes. In contrast to this, the peak of the wall-normal shear stress component, $\tilde{v}_r \tilde{v}_z$, is diminished in no-fence conditions, although a delay in the radial position of where the peak forms brings them to comparable values once $r/R > 2.3$.

For the mobilization and suspension of sediment into a turbulent boundary layer, the fluctuating stress components are typically the dominant contributors in comparison to pressure gradients and mean viscous shear stress. In the case of a coherent vortex within an impinging jet flow, it is perhaps of little surprise that the periodic stress components completely dominate over the stochastic components in the region of wall contact; the vortex is significantly larger and stronger than those that naturally formed in an unforced jet, and its coherence allow it to focus that energy in a highly localized and violent interaction at the walls surface. As seen in Figure 4.56, the average of these stresses at their peak can be 10 to 20 times greater than the stochastic component. The non-linear nature of this interaction rapidly destroys the coherence of the vortex and increases the stochastic fluctuations, all while the total stress is continually decreasing as the system relaxes towards the state of an axisymmetric turbulent wall jet. In this context, the greatest mobilization of sediment would be expected to occur within this narrow region ($2 < r/R < 2.5$), initiating saltation of larger sizes that will settle back further downstream when the fluctuation levels are no longer sufficient to keep the particles mobilized, while finer grains will be rapidly dispersed and carrier further out into the flow.

For the conditions where a small bump is present on the surface of a mobile bed, the measurements indicate that the erosion of the sediment would likely preferentially enhance the disturbance in the flow with base conditions small relative to the sediment uplift threshold values; the significantly higher stresses formed in the high-speed streak region would continue to erode the particles at a higher rate on either side of the disturbance, while the reduced stress level immediately downstream of the disturbance

would favor a reduced erosion rate, thus preserving a higher bed elevation. If one is well beyond the suspension threshold, then the erosion rate in both regions may be sufficiently rapid to preserve any significant azimuthal topography.

Chapter 5: Conclusion

The effect of a radial fence on a vortex-wall interaction was studied. The research was conducted to further the understanding of the driving fluid mechanics of rotorcraft brownout flow. A prototype for brownout flow was produced by employing an acoustically forced axial jet. Data was acquired using single-camera and stereo PIV to produce planar velocity data. The velocity data was assembled into volumetric data sets providing an ensemble averaged 3-dimensional view of the forced vortex ring. Data was acquired for high speed ($Re_I \approx 50,000$) and low speed ($Re_I \approx 10,000$) conditions with single event and continuous forcing. An axial fence similar to the striations commonly seen in sediment flow was introduced onto the ground plane of the experiment. Velocity, Reynolds stresses, vorticity, and enstrophy were calculated for each set to fully quantify the effect of the fence. Triple decompositions were employed to separate periodic contributions to the fluctuations from the stochastic variations in the flow. The experimental results were compared and validated against previous literature, mainly the work of Didden and Ho (1987) and Luton and Ragab (1997). The data was analyzed to produce several conclusions relating to the flow-field.

First, the effects of reducing the Reynolds number on the vortex-ground interaction were described. As previously seen in the literature, the vortex ring approached the ground plane hyperbolically before separating the wall boundary layer and forming a secondary vortex ring. The primary ring and the secondary ring act as a dipole and lift into the flow. As the Reynolds number increases, the effect of the secondary ring on the primary vortex trajectory is expected to increase. While the vortex location remains stable (before the onset of the rebound event), the two data sets produce

velocities and Reynolds stresses with similar magnitudes. Before the rebound event, the periodic Reynolds stresses dominate the flow; they are greater than the stochastic stresses by an order of magnitude. After the rebound event, the stochastic variation approaches and eventually surpasses the periodic fluctuations because of the increase in vortex jitter brought about by the non-linear interaction of the two vortices. Examining the profiles of the periodic stresses, it becomes apparent that coherent energy of the vortex is dissipated by the secondary vortex. The largest variations between the two presented data sets stems from the involvement of vortex jitter in the flow. It is noted that the jitter begins at different areas of the vortex-wall interaction due to the lack of damping of the instabilities in the high-speed data. Also, the jitter in the high Reynolds number data is coherently aligned with the streamlines of the mean flow, as opposed to a random scattering seen in the low speed data. This bias of the jitter organizes the stochastic fluctuations in the high speed data and manifests more recognizable structures of stochastic Reynolds stresses.

The wrapping mechanisms caused by the fence agree well with the simulations of Luton and Ragab (1997) with a few exceptions. While the previously conducted simulations initiated wrapping events with random perturbations on the ground plane, this experiment instead forced a single wrapping event with a single dominant disturbance on the wall surface. The secondary kinks in the boundary layer under the primary vortex are instead uplifted by the flow field generated by the primary wrapping event. This difference leads to the wrapping above the vortex ring to occur differently, as the secondary kinks exist under the primary kink when looped over the primary vortex ring. Three-component velocity measurements acquired from a horizontal plane very close to

the surface were analyzed using a triple-decomposition to examine the role of the coherent forced vortex in the presence of the radial fence. The results show a dramatic increase in the coherence of the three-dimensional looping exhibited by the secondary vortex, leading to a more organized and strongly perturbed mean flow. Specifically, a triple decomposition of the velocity fluctuations indicates a very intense periodic stress in the vicinity of the impingement site, followed by a significant decay. Conversely, the random component of the fluctuating stresses gradually increase to modest levels as the coherent contributions decrease, eventually becoming comparable to greater than the coherent stress. The fence produces a bifurcation in the flow through the perturbation of the secondary vortex, which in turn creates a high- and low-speed streak on either side of the fence.

The following implications for sediment uplift in rotorcraft brownout flow are illuminated by this study:

- The rotor-tip vortices are the dominant sediment uplift features of rotor downwash flow.
- The vortex-wall interaction produces the highest wall normal velocities in rotor downwash flow.
- The introduction of wall fence structures favors the preferential erosion on either side of the topographic disturbance.

The highest Reynolds stresses associated with rotor downwash flow occur during the interaction of the vortex ring with the ground plane. The acceleration of the vortex by the wall (as represented by an image vortex) as well as the jet formed between the primary-

secondary vortex dipole form large areas of stress near the ground plane. Without the rotor-tip vortices, or with vortices of significantly reduced circulation and coherence, the flow sediment beds would be subjected to more scour and saltation as opposed to the uplift and bombardment associated with brownout clouds. From the results of this study, it may be determined that reducing the strength and coherence of the tip vortices formed by rotorcrafts may serve as the best form of fundamental brownout mitigation.

The introduction of the axial fence also has implications for sediment uplift. The fences may serve to organize the uplift patterns of rotorcraft brownout, describing the origins and growth of the striations seen on the ground plane. It was shown that topographic disturbances on the wall plane would be preferentially eroded by the stresses induced by the vortex-wall interaction in near uplift threshold conditions. A parametric study on fence location, height, and frequency could illuminate the possibilities of utilizing fence arrays to organize sediment uplift away from problem areas of cloud formation (i.e., the areas in the pilot's field of view) as well as increasing primary vortex dissipation.

Appendix A: Pressure Calculations

Two kinds of pressure losses were observed in the jet. The major losses are caused by surface roughness from the PVC, honeycomb, and blower tubing. Minor losses are seen at the entrance and exit of the each section of the jet along with the turbulence reduction screens. The losses are calculated using the following equations:

Major losses:

$$\Delta p_{\text{major}} = (f \cdot L/d) \cdot (\rho \cdot V^2/2)$$

Minor losses:

$$\Delta p_{\text{minor}} = k \cdot (\rho \cdot V^2/2)$$

Pressure losses are calculated at the diffuser entrance and exit, tubing entrance and exit, plenum sections, honeycomb entrance and exit, coarse and fine screens, and the nozzle entrance and exit. The losses are calculated based off the maximum desired velocity at the nozzle outlet (18ms^{-1}). This velocity is translated through the jet using the constant flow rate relation $A_1 V_1 = A_2 V_2$. The following table (Table A.1) shows the areas and associated velocities of each section where loss is expected.

	Area (m ²)	Velocity (m/s)
diffuser entrance	0.016668	16.72814
diffuser exit	0.051613	5.402379
tubing entrance	0.009501	29.34836
tubing exit	0.009501	29.34836
plenum section 1	0.06196	4.500188
honeycomb entrance	0.04963	5.618212
honeycomb exit	0.04963	5.618212
plenum section 3	0.06196	4.500188
nozzle entrance	0.06196	4.500188
nozzle exit	0.015491	18

Table A.1: The area and associated velocities with each section of the jet given an exit velocity of 18ms^{-1} .

The other necessary parameters for pressure loss calculations (wetted perimeter, hydraulic diameter, Reynolds number, surface roughness, friction loss factor, length) are included in the following tables (Table A.2 and A.3):

	K	Section	Length (m)
Diffusor	.53604	Tubing	1
Diffusor-Tubing	.5	PVC	.5255
Tubing-Plenum	1	Honeycomb	.12
Fine Screen	2.5		
Fine Screen	2.5		

Table A.2: The loss characteristics of each section of the jet.

	Pw (m)	Dh (m)	Re
diffuser entrance	0.53604	0.124382	128534.2
diffuser exit	0.9144	0.225778	75349.37
tubing entrance	0.099746	0.03175	57562.68
tubing exit	0.099746	0.03175	57562.68
plenum section 1	2.363986	0.10484	29145.47
honeycomb entrance	0.015708	0.005	1735.328
honeycomb exit	0.015708	0.005	1735.328
plenum section 3	2.363986	0.10484	29145.47
nozzle entrance	2.363986	0.10484	29145.47
nozzle exit	0.880752	0.070352	78228.02

Table A.3: The physical characteristics of each section of the jet.

Using the aforementioned parameters, the pressure losses across each of the critical areas are calculated and displayed in the following table (Table A.4):

	Δp (pascals)
Diffusor	26.04953
Diffusor-Tubing	276.4868
Tubing	1219.154
Tubing-Plenum	552.9735
Plenum	0.290396
Honeycomb	7.595184
Screen 1	5.984185
Screen 2	5.984185
Nozzle	260
Total	2354.518

Table A.4: loss values of each section of the jet.

The pressure loss calculations were repeated for different flow velocities to create pressure curves. The curves were compared against the performance curves of several blower options in the following figure (Figure A.1):

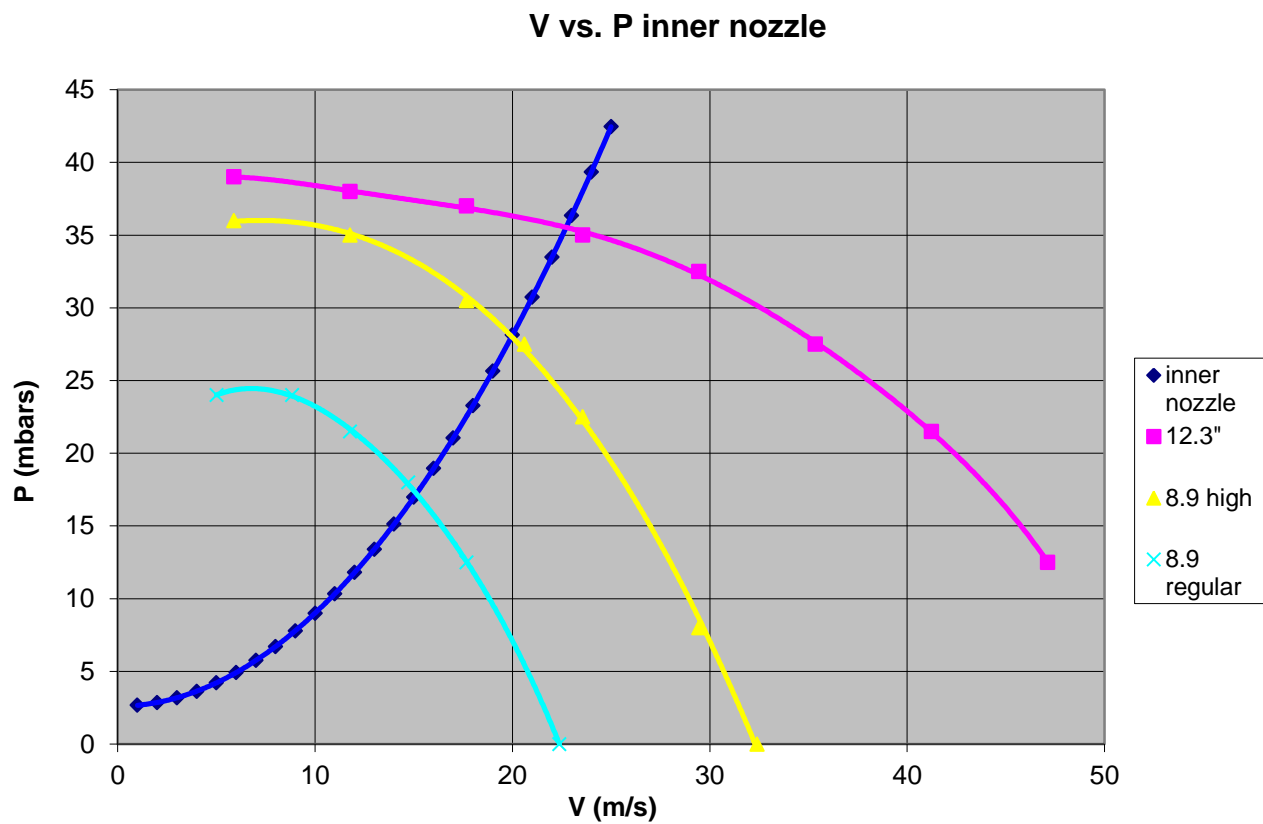


Figure A.1: Performance Characteristics for multiple fans.

Appendix B: Uncertainty Propagation

To calculate the values of the vorticity from the velocity fields obtained by PIV, derivatives of the velocity must be estimated. These derivatives are estimated with the following second order central finite-difference scheme:

$$\frac{\partial U_i}{\partial x_j} \cong \frac{\delta U_i}{\delta x_j} = \frac{U_i(x_j + \delta x_j) - U_i(x_j - \delta x_j)}{2\delta x_j}$$

where δx_j represents the grid spacing and U_i is the velocities obtained from PIV. The truncation of the central difference theme also adds to the uncertainty of the reported vorticity measurements. This translates into a total uncertainty value for the derivative of:

$$\left| \frac{\partial \tilde{U}_i}{\partial x_j} - \frac{\delta U_i}{\delta x_j} \right| = O(\delta x^2) + O\left(\frac{\Delta U_i}{\delta x_j}\right)$$

where \tilde{U}_i is the true velocity and ΔU_i is the uncertainty from the velocity measurement. The value of the truncation error is given by Foucaut and Stansislas (2002). After accounting for the truncation error, the true uncertainty in the derivatives can be expressed as:

$$\Delta \frac{\delta U_i}{\delta x_j} = \frac{\delta x_j^2}{3!} \frac{\partial^3 U_i}{\partial x_j^3} + 0.71 \frac{\Delta U_i}{\delta x_j}$$

where the third derivative is approximated as:

$$\frac{\partial^3 U_i}{\partial x_j^3} \cong \frac{\delta^3 U_i}{\delta x_j^3} = \frac{U_i(x_j + 2\delta x_j) - 3U_i(x_j + \delta x_j) + 3U_i x_j - U_i(x_j - \delta x_j)}{\delta x_j^3}$$

On average, the truncation error is about 15% of the magnitude of the SEM and, therefore, is deemed insignificant. Each component of the vorticity is calculated as follows:

$$\bar{\omega} = \frac{1}{2} \nabla \times \bar{U} = \frac{\delta U_j}{\delta x_i} - \frac{\delta U_i}{\delta x_j}$$

The propagation of the uncertainty leads to a final vorticity uncertainty of:

$$\Delta \vec{\omega} = \Delta \frac{\delta U_i}{\delta x_j} \sqrt{2}$$

The enstrophy is calculated as sum of the squares of all components of the vorticity, i.e.:

$$\varepsilon = \sqrt{\omega_x^2 + \omega_y^2 + \omega_z^2}$$

which translates to an error of:

$$\Delta \varepsilon = \Delta \omega \sqrt{3}$$

References:

- Aydemir, E., Worth, N. A., and Dawson, J. R. 2010, The formation of vortex rings in a strongly forced round jet, *Exp. Fluids* DOI 10.1007/s00348-011-1110-6.
- Brown, R.E., Houston, S.Crow, S.C. (1970) Stability theory for a pair of trailing vortex rings. *AIAA J.* **8**, pp 2172-2179
- Crow, S. C. & Champagne (1971) Orderly structure in jet turbulence. *J. Fluid Mec.*, **48**, pp 547-591
- Diddeen, N. & Ho, C.M. (1985) “Unsteady separation in a boundary layer produced by an impinging jet,” *J. Fluid Mech*, **160**, pp. 235-256
- Elliott, J. W., Cowley, S. J., and Smith, F. T. 1983, Breakdown of boundary layers: (i) on moving surfaces; (ii) in self-similar unsteady flows; (iii) in fully unsteady flow. *Geophys. Astrophys. Fluid Dyn.* **25**,77-138
- Gawthrop, Shepherd, and Perrott, J. (1931) *Franklin Inst.*, 211, pp 67-86
- Gharib, M., Rambod, E., Shariff, K. (1998) A universal time scale for vortex ring formation. *J Fluid Mech* 360, pp121-140
- Greeley, Ronald, and James D. Iversen. (1985)*Wind as a geological process: on Earth, Mars, Venus, and Titan.* Cambridge Cambridgeshire: Cambridge University Press, Print.
- Helmholtz, H. (1987) On integrals of the hydrodynamic equations which express vortex motion. *Phil. Mag.* **33**, 485-512
- Jimenez, J. & Moin, P. (1991) The minimal flow unit in near-wall turbulence *J. Fluid Mech.* **225**, pp 213-240
- Jimenez, J. (2004) Turbulent flows over rough walls. *Annu. Rev. Fluid Mech.* 36, pp 173–196
- Johnson, B. (2009) “Mechanisms of Sediment Entrainment and Transport in Rotorcraft Brownout,” Unpublished Master’s Thesis. University of Maryland.
- Lasheras, J.C. and Choi, H. (1988), Three-dimensional instability of a plane free shear layer: an experimental study of the formation and evolution of streamwise vortices,*J. Fluid Mech.* **189**, pp 53-86
- Lawson, N. J., & Wu, J. (1997). Three-dimensional particle image velocimetry: Error analysis of stereoscopic techniques. *Meas. Sci. Technol.* **8**, pp 894-900

- Leishman, J. G. (2008) Rotorcraft Brownout: Advanced Understanding, Control and Mitigation. DTIC Document
- Lim, T. T. & Nickels, T. B. (1995) Vortex Rings. S. I. Green (ed.) Fluid Vortices 95-153
- Luton J. & Ragab, S.A. (1997) “The Three-Dimensional Interaction of a Vortex Pair with a Wall,” *Phys. of Fluids*, **9**, pp 2967-2980
- Magarvey, R. H. & MacLachy, C. S. (1964) The formation and structure of vortex rings. *Can. J. Phys.* **42**, 678-689
- Milne-Thompson, L. M. 1963, *Theoretical Hydrodynamics* 4th Edition Macmillan
- Morel, T. (1975) Comprehensive design of axisymmetric wind tunnel contractions. *J. of Fluids Engng.* **97**, pp 225-233
- Perrin, R., Braza, M., Cid, E., Cazin, S., Barthet, A., Sevrain, A., Mockett, C., and Thiele, F. (2007), Obtaining phase averaged turbulence properties in the near wake of a circular cylinder at high Reynolds number using POD, *Exp. Fluids* **43**,341-355
- Reynolds, W. C., and Hussain, A. K. M. F. 1972, The mechanics of an organized wave in turbulent shear flow. Part 3. Theoretical models and comparisons with experiments, *J.Fluid Mech.* **54** ,pp 263-288
- Robinson, S.K. (1991) Coherent motions in the turbulent boundary layer. *Annu. Rev. Fluid Mech.* **23**, pp 601–39
- Vejrazka, J., Tihon, J., Marty, Ph. and Sobolik, V. (2005), Effect of an external excitation on a circular impinging jet, *Phys. Fluids* **17**,105012
- Walker, J.D.A., Smith, C.R., Cerra, and Doligalski, T.L. (1987) “The Impact of a Vortex Ring on a Wall,” *Journal of Fluid Mechanic*, **181**, pp. 99-140
- Walsh, M. J. (1990) Riblets. In *Viscous Drag Reduction in Boundary Layers*, ed. DM Bushnell, JN Hefner, pp 203–61. New York: AIAA
- Widnall, S. E. & Sullivan, J. P. (1973) On the stability of vortex rings. *Proc. Roy. Soc. A* **332**, 335-353
- Widnall, S. E., Bliss, D. B., Tsai, C. Y. (1974) The instability of short waves on a vortex ring. *J. Fluid Mech.* **66**, 35
- Yuan, J. & Piomelli, U. (2010) Large-eddy simulation of acceleration boundary layers over rough surfaces

Zaman, A. K. M. F. & Hussain, K. B. M. Q. (1980) The 'preferred mode' of the axisymmetric jet. *J. Fluid Mech.* **110**, 39-71